

**Development of deformational regimes and crystal orientation fabric, microstructures and deformational regimes in the deep sections and overall layered structures of the Dome Fuji ice core, Antarctica**

Tomotaka Saruya<sup>1</sup>, Atsushi Miyamoto<sup>2</sup>, Shuji Fujita<sup>1,3</sup>, Kumiko Goto-Azuma<sup>1,3</sup>, Motohiro Hirabayashi<sup>1</sup>, Akira Hori<sup>4</sup>, Makoto Igarashi<sup>1</sup>, Yoshinori Iizuka<sup>5</sup>, Takao Kameda<sup>4</sup>, Hiroshi Ohno<sup>4</sup>, Wataru Shigeyama<sup>3\*</sup>, Shun Tsutaki<sup>1,3</sup>

<sup>1</sup> National Institute of Polar Research, Tokyo 190-8518, Japan  
<sup>2</sup> Institute for the Advancement of Graduate Education, Hokkaido University, Sapporo 060-0817, Japan  
<sup>3</sup> Polar Science Program, Graduate Institute for Advanced Studies, SOKENDAI, Tokyo 190-8518, Japan  
<sup>4</sup> Kitami Institute of Technology, Kitami 090-8507, Japan  
<sup>5</sup> Institute of Low Temperature Science, Hokkaido University, Sapporo 060-0819, Japan

\*Currently at: JEOL Ltd., Tokyo, Japan

**Correspondence:** Tomotaka Saruya (saruya.tomotaka@nipr.ac.jp), Atsushi Miyamoto (miyamoto@high.hokudai.ac.jp), Shuji Fujita (sfujita@nipr.ac.jp)

Added (or partially modified)  
Moved  
Modified Figure  
Removed

An in-depth examination of the rheology in the deep sections of polar ice sheets is crucial for understanding glacial flow. This study investigates the crystalline textural properties of a 3035-meter-long Antarctic deep ice core, drilled at an inland plateau dome, with a focus on the lowermost ~20%. Inland plateau domes provide a unique opportunity to study ice deformation processes with minimal influence from simple shear. We analyze the crystal orientation fabric of both c- and a-axes, comparing them with various other properties measured from the ice core. To examine the distribution and texture of the c- and a-axes, we employed three methods: the dielectric tensor method (DTM) for bulk properties of thick sections, Laue X-ray diffraction for detailed crystal grain orientations, and an automatic ice fabric analyzer for grain-by-grain analysis using thin sections. Microstructural observations were made using optical microscopy. DTM provided preferred c-axis orientations as eigenvalues with high sampling frequency, spatial resolution, and continuity, offering statistical significance. Laue X-ray diffraction clarified detailed preferred orientations of both c- and a-axes, while the automatic fabric analyzer tracked c-axis orientation variations among individual grains. Microstructural images revealed dynamic recrystallization. In the uppermost ~80% thickness zone (UP80%), the clustering strength of single-pole c-axis fabric steadily increased, reaching a maximum at the bottom, driven primarily by vertical compression. Below 1800 m in the UP80%, layers with varying dusty impurities

showed different rates of cluster strength growth, a pattern that persisted until 2650 m. In the lowermost ~20% zone (LO20%), the c-axis clustering strength trend changed around 2650 m, with substantial fluctuations below this depth. Impurity-rich layers maintained stronger clustering, while impurity-poor layers showed relaxation, likely due to the emergence of new grains with c-axis orientations offset from the existing cluster and migration recrystallization. These impurity-poor layers exhibited features of bulging and migrating grain boundaries, with a decrease in grain aspect ratio. Additionally, in such ice, the a-axis organization progressed, displaying one or two sets of three preferred orientations within the a-axis girdle, orthogonal to the c-axis cluster, possibly due to crystal twinning. These findings confirm that dislocation creep is the primary deformation mechanism in polar ice sheets. In the LO20%, dynamic recrystallization plays a critical role, with more pronounced effects in impurity-poor layers than in impurity-rich layers, enabling the continuation of dislocation-creep-based deformation and forming a-axis organization within the a-axis girdle, particularly under higher temperatures closer to the bed. Additionally, c-axis layers and cluster axes rotate meridionally due to rigid-body rotation from simple shear strain above subglacial slopes. Insights into these nonlinear, irreversible processes offer vital clues for understanding the 3D structure of polar ice sheets, leading to inhomogeneous deformation, the formation of folds, faults, and mixing between layers at various thickness scales.

An in depth examination of rheology within the deep sections of polar ice sheets is essential for enhancing our understanding of glacial flow. In this study, we investigate the crystalline textural properties of the 3035 m long Antarctic deep ice core, with a particular emphasis on its lowermost 20%. We examine the crystal orientation fabric (COF) and compare it with various other properties from the ice core. In the uppermost approximately 80% thickness zone (UP80%), the clustering strength of single pole COF steadily increased, reaching its possible maximum at the bottom of the UP80%. Below 1800 m in the UP80%, layers with more or fewer dusty impurities exhibit slower or faster growth of cluster strength. This situation continued until 2650 m. In the remaining lowermost approximately 20% thickness zone (LO20%), the trend of the COF clustering strength changed around 2650 m and exhibited substantial fluctuations below this depth. In more impurity rich layers, stronger clustering is maintained. In impurity poor layers, relaxation of the COF clustering occurred due to the emergence of new crystal grains with c axis orientation distinctly offset from the existing cluster, and dynamic recrystallization related to this emergence. The less impure layers show apparent features of bulging and migrating grain boundaries. We argue that the substantial deformational regime of polar ice sheets involves dislocation creep in both UP80% and LO20%, with dynamic recrystallization playing a critical role in the LO20%, particularly in impurity poor layers, to recover a potential of COF available for the continuation of dislocation-creep based deformation. Furthermore, we observe that layers and cluster axes of COF rotate meridionally due to rigid-body rotation caused by simple shear strain above subglacial slopes. These features provide vital clues for the development of the 3D structure of polar ice sheets in the deeper part, leading to inhomogeneous deformation between layers in various thickness scales, and the formation of folds, faults and mixing depending on the layers.

## 65 1. Introduction

### 66 1.1 Modeling ice sheets: challenges and insights from crystals to continents

67 The polar ice sheets are massive bodies of ice on Earth. With ongoing global warming, there is a deep concern about the  
68 trend of these ice sheets contributing to sea level rise (e.g., Church et al., 2013). Continuous improvement of reliable predictive  
69 models for this phenomenon is crucial. However, there are many key processes that govern the flow of ice sheets, making the  
70 modelling of these sheets complex. Although many essential processes exist, many are not included in modelling efforts due  
71 to insufficient understanding (e.g., Pattyn et al., 2008). Deciphering the dynamic layer structure within the ice sheet is one of  
72 the most critical challenges (e.g., Young et al., 2017).

### 73 1.2 Crystal anisotropy and ice sheet dynamics

74 The response of individual ice crystals to stress exhibits a pronounced anisotropy in deformation. Crystals readily undergo  
75 shearing along the slip systems within their basal planes, whereas shearing on alternate slip systems is significantly more  
76 difficult, nearly a hundredfold (e.g., Duval et al., 1983). The overall rate of deformation in a polycrystalline aggregate under  
77 stress is influenced by the orientation of its constituent crystals. If the crystals within an aggregate are randomly oriented, the  
78 material will behave isotropically; however, if the orientations of the crystals are not random, the material will show anisotropic  
79 behavior. The study of anisotropic ice deformation has been conducted historically. They were done through theoretical  
80 research (e.g., Alley, 1992; Azuma, 1995; Azuma and Goto-Azuma, 1996; Castelnau et al., 1996; Gödert and Hutter, 1998;  
81 Johnson, 1977), and through laboratory experiments (e.g., Duval, 1981; Duval and Le Gac, 1982; Shoji and Langway Jr., 1985;  
82 Pimienta et al., 1988; Budd and Jacka, 1989; Castelnau et al., 1998; Goldsby and Kohlstedt, 2001; Qi et al., 2019; Fan et al.,  
83 2020). These laboratory-based studies are characterized by experimental setting of strain rate by more than several orders of  
84 magnitude, and under temperature close to melting point, typically between -20 and 0 °C. Therefore, these laboratory-based  
85 knowledge can be a valuable reference mainly for such conditions. To better understand rheology of polar ice sheets, analyses  
86 of ice texture sampled from polar ice sheets play another essential role. Examples of Antarctic deep ice core include, Dome  
87 Fuji (hereinafter, DF) ice core (e.g., Azuma et al., 2000 and Saruya et al., 2022b), EPICA Dome C (hereinafter, EDC) ice core  
88 (e.g., Wang et al., 2003, Durand et al., 2007, 2009) , Byrd ice core (Gow and Williamson, 1976) , EDML ice core (e.g.,  
89 Weikusat et al., 2017), Mizuho Station ice core (Fujita et al., 1987; Higashi et al., 1988), Talos Dome ice core (Montagnat et  
90 al., 2012), WAIS Divide ice core (Fitzpatrick et al., 2014) and South Pole (SPICE) ice core (Abbasi et al., 2024). Examples of  
91 Greenland ice sheet include GRIP ice core (Thorsteinsson et al., 1997), NEEM ice core (Montagnat et al., 2014), EGRIP ice  
92 core (Stoll et al., 2021a, 2022; Richards et al., 2023) and among others. In these studies, the influence of anisotropy on the  
93 movement of ice aggregates is so substantial that comprehending its impact on the expansive flow patterns of ice sheets is  
94 essential (e.g., Castelnau et al., 1998; Mangeney et al., 1997; Paterson, 1991; Russell-Head and Budd, 1979; Thorsteinsson et  
95 al., 1999). For instance, during the internal deformation of the ice sheet, the flow forms  $\epsilon$  preferred orientations of crystal

axes, at the same time, the ice flow is modulated based on COF them. The ice flow is also modulated by the concentration of ionic species and microparticles, as well as disturbances or folds in the layer structure (e.g., Cuffey and Paterson, 2010, Durand et al., 2007, Saruya et al., 2022b). These factors can introduce either positive or negative feedback, modulating the flow characteristics of the ice sheet. Considering this complex nature of ice, we need a systematic understanding of the layered internal structure of polar ice sheets over space and time. An important method for understanding these is to conduct analysis of ice cores in terms of ice dynamics, which provides a “ground truth” perspective of the ice.

### 1.3 Advantages of ice cores from dome regions in central plateau area of the ice sheets

The ice in the dome summit regions of central plateau areas on ice sheets offers an opportunity for studying ice deformation processes. In these regions, conditions are relatively simplified because it can be presumed that they are least affected by simple shear deformation. This deformation is typically caused by surface slope and gravity. Because of this simplicity, dome regions in central area of the ice sheets are often chosen as ice core drilling sites for the purpose of exploring the history of past climate changes. At the same time, these sites are ideal for investigating how processes related to deformational progress (such as dislocation creep and recrystallization) develop in a relatively simplified stress-strain environment and under moderate temperature gradients. Among the drilling sites in Antarctica shown in Figure 1, we can presume that so far only DF and EDC sites meet this condition. In fact, in the case of inland domes, ice deforms mainly by compression along the vertical. This is confirmed by the preferred orientation of *c*-axes measured along cores drilled at these sites (as in references listed above), which exhibit a single pole distribution of the *c*-axes. Similarly, this has been confirmed in the Greenland ice sheet with the GRIP core (Thorsteinsson et al., 1997). We note that there are also local domes at the edge of the ice sheet plateau, for example, Talos Dome (Urbini et al., 2008). Such a dome is characterized by lower elevation (of 2318 m), location facing to the coast, with annual accumulation rate much larger than those of central plateau (by 3~4 times), and migration at least in the last few centuries. Such a dome has higher instability, and it is suitable to investigate impact of more shear in contrast to the domes in the central plateau area. Evolution of preferred orientation of *c*-axes for the Talos Dome core was presented by Montagnat et al. (2012).

### 1.4 Exploring deep ice rheology and crystal properties

In ice sheets, the rheology in deep ice (deepest several hundred meters) is complicated by geothermal effects and increased stresses from bedrock topography. So far, there have been limited reports on the crystal properties of ice near the bed at dome summits of central plateau of the ice sheets (e.g., Thorsteinsson et al., 1997; Durand et al., 2009, Faria et al., 2014a, Ohno et al., 2016). The DF ice core was drilled on the Antarctic plateau (Figure 1). This location is at 77°19' S latitude and 39°42' E longitude, and 3,810 m above sea level. Annual surface mass balance (SMB) has ranged from approximately 24 to 28 kg m<sup>-2</sup> y<sup>-1</sup> over the last 5000 years (Oyabu et al., 2023), and the annual mean surface air temperature is -54.4°C (Yamanouchi et al., 2003). For the DF ice core, Ohno et al. (2016) revealed the air hydrates and water isotope composition of

the deepest 1% thickness (3000–3035 m). These properties were found to retain the basic layered structure of ice core signals except in the deepest few meters. However, the investigation did not include the COF crystalline textural properties. For the EDC core (Figure 1), Durand et al. (2009) investigated the COF *c*-axis orientations of ice down to the very deep parts, using thin sections of ice (40 × 110 mm in width and 0.4 mm in thickness) sampled at every 11 m depth.

Deep ice is characterized by higher temperature, under which enhancement of molecular transport phenomena is an issue (e.g., Petrenko and Whitworth, 1999). The molecular transport phenomena include plastic deformation, the molecular diffusion process and recrystallization. Dynamic recrystallization within ice sheet has been widely investigated historically, as reviewed in papers or textbooks (e.g., Poirier 1985; Humphreys and Haterly 2004; Faria et al., 2014a, b) or individual papers (e.g., De La Chapelle et al. 1998; Weikusat et al. 2009, Kipfstuhl et al. 2009, Montagnat et al. 2012, 2014; Stoll et al., 2021a). Exploring deep ice rheology and crystal properties, dynamic recrystallization is one of main focuses in this paper.

### 1.5 Advancing ice sheet dynamics: The development and role of crystal orientation fabric

The COF crystal orientation fabric contains information of deformational history, grain growth and recrystallization (e.g., Cuffey and Paterson, 2010; Faria et al., 2014a, b). Saruya et al. (2022b) investigated the layer structures of COF the *c*-axis fabric in the uppermost (shallower) ~~ea-~~80% thickness zone (hereinafter, UP80%) of the DF ice core. They used thick sections of ice (ranging in thickness from 33 to 79 mm) employing the principle of the radio-wave birefringence to obtain information from a volume much larger than that of thin sections of ice in typical thickness of about 0.3–0.5 mm. The sampling volumes between the two methods (thick-section method and thin-section method) differ by a factor of 85–190 around two order of magnitude. Using the dielectric tensor method (hereinafter, DTM), they continuously measured “dielectric anisotropy” (denoted as  $\Delta\epsilon$ ) along the ice cores with high resolution, involving ice volumes of cylinders measuring 16–38 mm in effective radio beam diameter and 33–79 mm in radio propagation thickness. This  $\Delta\epsilon$  is defined as the difference in relative permittivity along the vertical (denoted as  $\epsilon_v$ ) and in the horizontal plane (denoted as  $\epsilon_h$ ). Thus,  $\Delta\epsilon = \epsilon_v - \epsilon_h$ .  $\Delta\epsilon$  is an indicator of the clustering strength of COF *c*-axes.  $\Delta\epsilon$  is linearly compatible with the normalized eigenvalues of the second order tensor (Saruya et al., 2022a, b). The normalized eigenvalues are often used to express the degree of the COF *c*-axes clustering. Thus, continuous profiling with DTM is an innovative and powerful tool to directly measure the normalized eigenvalues for COF preferred orientation of *c*-axes with symmetry (such as single pole, girdle type or superposition of them). These authors found that  $\Delta\epsilon$  steadily increases with depth, showing fluctuations in the UP80%. In addition, significant decreases in  $\Delta\epsilon$  were found at depths of major glacial to interglacial transitions. These changes in  $\Delta\epsilon$  are explained as variations in the deformational history of the vertical compression. Moreover, fluctuations in  $\Delta\epsilon$  along neighboring depths were enhanced during the glacial/interglacial transitions. Furthermore, the  $\Delta\epsilon$  data exhibited a positive correlation with the concentration of Cl<sup>-</sup> ions and an inverse correlation with the amount of dust particles. Since these factors originate from atmospheric deposition, Saruya et al. (2022b) proposed that the fluctuations in COF the clustering strength might be common across wide area of ice sheets. This hypothesis for the Dome Fuji core, in part, differs from an existing hypothesis for the EDC ice core given by Durand et al. (2007). That

is, the changes in the clustering strength (which increase sharply with depth) were associated with positive feedback between variations in ice viscosity and the impact of a shear stress component, also increasing with depth (Durand et al., 2007). A basic difference is that Saruya's hypothesis did not need to assume the presence of shear deformation as a prerequisite to explain the observed fluctuations of the clustering strength whereas Durand et al. (2007) suggested the impact of shear and the positive feedback was important.

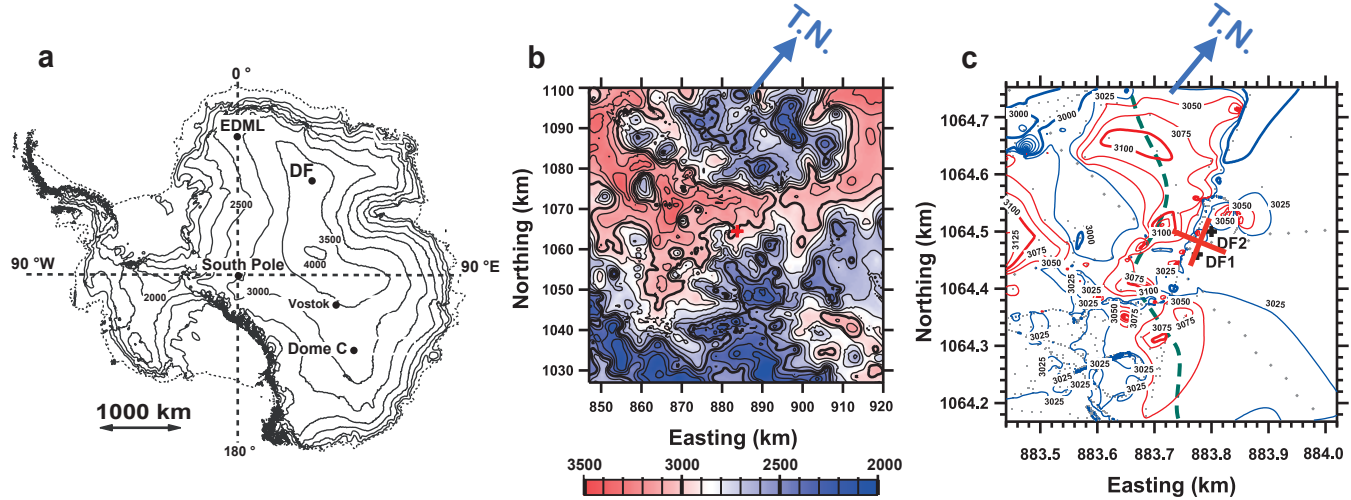
Following this previous study, research focusing on the lowermost (deepest) approximately 20% thickness zone (ranging from about 2400 m to the deepest ice at 3035 m) remains to be done, to examine textural data for the entire thickness of the ice sheet. Hereinafter, we refer to this zone as LO20%. A major difficulty was the inclination of the ice sheet layers, which became steeper at deeper depths (Dome Fuji Ice Core Project Members hereinafter referred to as DFICPM, 2017). In the present study, we extend the investigation to the LO20%. To investigate this, we utilized the thick-section-based method of (i) DTM, and thin-section-based methods such as (ii) the Laue X-ray diffraction method and (iii) the microstructural observations. We compare textural data by these methods with various data from ice core analyses analyzed from the ice core. This paper provides a comprehensive an advanced and most updated dataset of COF crystal orientation fabric for both *c*-axis and *a*-axis, and other textural data for the entire thickness of the ice sheet at DF. We then discuss COF development of crystal orientation fabric, variations in the microstructure, layered structures, and rheology of polar ice sheets, addressing differences in the existing hypotheses. Our new data will provide important clues for understanding the development of the layer structure of ice sheets, which leads to inhomogeneous deformation of layers across various layer thickness scales.

Furthermore, retrieving continuous ice core records that correspond to ages of more than 1 million years presents a significant challenge in palaeoclimatology (e.g., Wolff et al., 2022). International Partnerships in Ice Core Sciences (IPICS) identified the retrieval of multiple ice cores that extends to 1.5 million years (symbolically named as the “oldest-ice cores”) as one of the most important challenges for ice core studies. Identifying suitable sites for drilling of such ice will require improved knowledge of glacial layers under various ice conditions. Note that a list of abbreviations is provided in Appendix A for clarity of terms used in this paper.

## 2. DF ice cores

At DF, deep ice cores have been drilled twice (e.g., Motoyama et al., 2020). The first core, “DF1” measuring 2503 m in length, was drilled in the 1990s. The second, “DF2,” a 3035-m-long core, was drilled between 2004 and 2007 in a borehole 44 m away from the previous borehole (Figure 1c). We used the DF2 core in this study. The drilling sites are situated above a subglacial slope, positioned between bedrock high in the east and a subglacial trough with an ice thickness of about 3100 m in the west (Figures 1b and 1c). An ice thickness of about 2850 m marks the boundary between thawed bed (in thicker ice) and a frozen bed (in thinner ice) (Fujita et al., 2012). It is speculated that spatially inhomogeneous basal melting has caused the layer inclination in localized areas within the ice sheet (DFICPM, 2017). The layered structures incline by less than about 5° in the UP80% while in the lower 20% (LO20%), the inclination reaches values up to 45° at a depth of 3000 m.

191 In terms of the *c*-axis fabric, Azuma et al. (1999; 2000) reported that at DF1 the *c*-axis fabric exhibited the elongated single  
 192 pole fabric as the dome undergoes deviatoric strain depending on orientations. This elongated single pole fabric is already  
 193 observable at shallow depths. In addition, Fujita et al. (2006) discussed, based on polarimetric radar sounding at Dome Fuji,  
 194 the amount of radio wave birefringence caused by this elongated single pole, up to depths of about 2200 m. They demonstrated  
 195 that the orientations of the elongated single pole are consistent at least to this depth. Figure 1c shows inferred two principal  
 196 axes of the elongated *c*-axis fabric, aligning with the orientation of the subglacial slope (WNW) and its orthogonal direction.



197  
 198  
 199 **Figure 1.** Maps of the Coring Site. (a) Surface elevation (DEM by Bamber et al., 2009). (b) and (c) show the thickness of the ice in areas of  
 200 72 km square, and 580 m square, respectively. Marker symbols near the center indicate the coring site. T.N. stands for true north. In (c), data  
 201 points for ice thickness are represented by dots for the data from Tsutaki et al. (2022) and by markers for the data from Eisen et al. (2020).  
 202 A green bold dashed line indicates the presence of the local trough. The DF coring sites are located at the bank of this local trough, aligning  
 203 with the estimated drainage routes of subglacial water (as shown in Figure 8d in Tsutaki et al., 2022). On the Figure 1c, two principal axes  
 204 of elongated single pole fabric inferred from the polarimetric radar sounding (Fujita et al., 2006) is indicated.

### 205 3. Methods and samples

206 We utilized the thick-section-based method of DTM, as well as the thin-section-based methods of the Laue X-ray  
 207 diffraction method and the microstructural observation. On one hand, using DTM, *c*-axis fabric data are provided as  
 208 eigenvalues with high sampling frequency, high spatial resolution, and continuity, thereby offering statistical significance.  
 209 However, this method does not produce data for the crystal axes of individual grains. Additionally, if a cluster of *c*-axes is  
 210 significantly inclined from the vertical, it is impossible to derive correct eigenvalues without knowing both the inclination  
 211 angle of the *c*-axis cluster and the horizontal orientation of the *c*-axis cluster. On the other hand, the Laue X-ray diffraction  
 212 method allows us to clarify detailed information about both the *c*-axis and *a*-axes of each crystal grain. Additionally, the

automatic fabric analyzer, model G50, originally manufactured by Russel-Head Instruments, is a very useful method for demonstrating how crystal orientation differs from one grain to another. Using both the G50 and microscopy, we conducted microstructural observations to investigate the signals of dynamic recrystallization and grain morphology. The judicious use of these methods provides unprecedentedly rich information on crystalline texture along ice cores.

### 3.1 Dielectric Tensor Method

#### 3.1.1 Method

The principle of the open resonator method for determining the relative permittivity ( $\epsilon$ ) of thin samples have been described in the literature (Jones, 1976a, b; Cullen, 1983; Komiyama et al., 1991). We have developed this into a method for measuring the tensorial permittivity of thick samples by using radio birefringence continuously scanning along ice cores (Matsuoka et al., 1998; Fujita et al., 2009, 2014, 2016; Saruya et al., 2022a, b; Inoue et al., 2024). We apply a microwave beam to thick samples. The  $\epsilon$  values are volume-weighted averages within the volume encompassed by the Gaussian distribution of the beam. By setting the angle between the axis of the  $c$ -axes cluster and the electric field to approximately  $45^\circ$ , radio birefringence occurs due to macroscopic permittivity of the crystals (e.g., Hargreaves 1978). When we sweep radio frequencies to detect resonances satisfying TEM<sub>0,0,q</sub> modes (where TEM stands for transverse electromagnetic and  $q$  is an integer), we detect twin resonant peaks caused by the two permittivity components. These two components correspond to  $\epsilon$  along the axis of the  $c$ -axes cluster and its orthogonal axis, representing components on the plane of the electric field vector (orthogonal to the axis of beam incidence).

#### 3.1.2 The open resonators and samples

We utilized an open resonator, employing frequencies between 26.5 and 40 GHz (No.1 in Table A1) for the ice in the LO20%. This resonator is different from the resonator used for the ice in the UP80%, employing frequencies between 15 and 20 GHz (No.2 in Table A1). Specifications of the two resonators are summarized in Table A1 in Appendix A1. The two resonators, each having a semi-confocal shape with a flat mirror and a concave mirror, are designed to produce beam diameter of 16 mm and 38 mm, respectively. The consistency of the data obtained with the two resonators was confirmed by comparing the  $\Delta\epsilon$  values at depths between 2400 and 2500 m (Figure A1 in Appendix A1). The smaller beam size means that the No.1 resonator is available for smaller sized samples (for example, narrow quadrangular prism samples) and for higher spatial resolution measurements. The No.1 and the No.2 resonators can measure ice thickness at least 40 mm and 90 mm, respectively. Sizes of the samples are given in Figure 2 and Table A2. Both upper and lower surfaces were microtomed to make very smooth and precisely parallel surfaces. The sampling rate for the DTM involves continuous 20 mm step measurements along a 0.5-m-long core segment from every 2.5-m depth interval. For samples deeper than 2736 m, we rotated the core axis horizontally in the open resonator setup to achieve detectable twin resonances. The experimental temperatures were in a range of  $-30 \pm 1.5^\circ\text{C}$ .

Along with the increased layer inclination, the axis of the  $c$ -axes cluster also exhibited an increased inclination, deviating from the vertical (hereinafter, inclination angle) in the same direction of the maximum layer slope. We confirmed that these two are in the same vertical plane throughout the LO20%. Additionally, the horizontal orientation of the  $c$ -axes cluster varied with depths due to the rotation of the ice cores. Under conditions where both inclination angle and horizontal orientation of the  $c$ -axes cluster change with depths, we measure only the non-principal components of the permittivity tensor within the ice using DTM. To apply geometrical corrections from the measured non-principal components to the principal components, we utilized information of both inclination angle and horizontal orientation of the  $c$ -axes cluster, derived from COF  $c$ -axis fabric data measured using thin-section method. The procedures for these corrections are detailed in Appendix B. The non-principal components of the dielectric anisotropy ( $\Delta\epsilon'$ ) were adjusted to align with the principal components ( $\Delta\epsilon$ ). We also note that the DTM is also useful to detect  $\Delta\epsilon$  values in the girdle type ice fabrics. We can refer to basic principle in Appendix A2, as girdle distribution of  $a$ -axes in the figure.

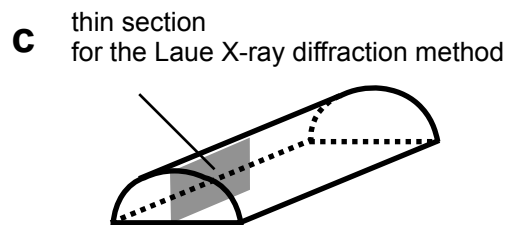
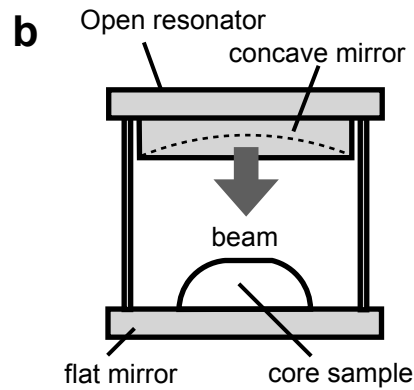
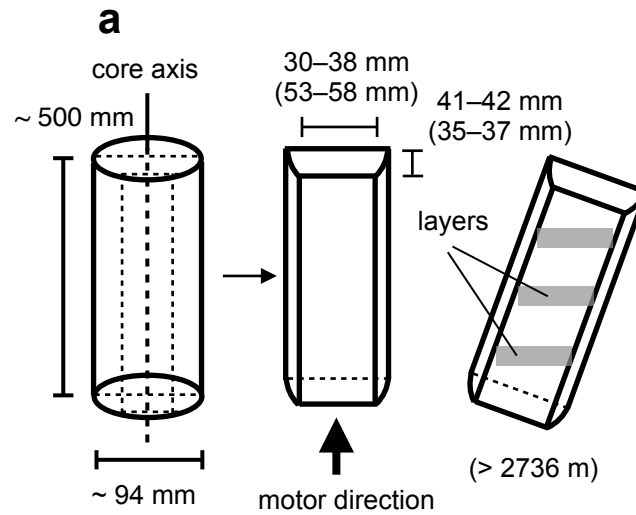


**Figure 2.** Diagrams of the (a) core cutting geometry, (b) setup viewed from the front, and (c) location of a thin section for the Laue X-ray diffraction method.

### 3.2 Laue X-ray diffraction method, microstructure observations and automatic fabric analyzer method

The Laue X-ray diffraction method was applied to thin sections measuring  $100 \text{ mm} \times 45 \text{ mm}$  (in the vertical and horizontal direction, respectively, with a thickness of less than  $0.5 \text{ mm}$ ). This method can determine the orientations of all axes of each

crystal grain with accuracy of  $\sim 0.5$  degree (Miyamoto et al., 2011). 43 42 depths within the thickness of the LO20% were selected. After obtaining all the Laue figures, the Laue patterns were analyzed. In each thin section, we express the data as the distribution of  $c$ -axes and  $a$ -axes on the Schmidt net diagram. In addition, we calculated the median inclination of  $c$ -axes with reference to the axis of the  $c$ -axes cluster. The median inclination is defined as a half apex angle of the cone in which a half of the measured  $c$ -axes are included from the center axis of the  $c$ -axes cluster.

Additionally, we conducted microstructure observations both G50 and using optical microscopy to investigate how microstructural evolutions affect the  $c$ -axis development and fluctuation on the same thin section. These measurements were performed at several selected depths. We prepared thin sections from the vertical plane of the ice cores, measuring 90 mm in the depth direction, 50 mm in the horizontal direction, and 0.5 mm in thickness. In addition, COF images of  $c$ -axis fabric were obtained using G50 automatic fabric analyzer, originally manufactured by Russell Head Instruments, to investigate the relationship between grain morphology and  $c$ -axis orientation of each grain.

Grain numbers included in a Gaussian beam or in a thin section are listed in Table A3. Depending on number of crystal grains in a beam or thin section, statistical significance is different. In some cases, moving averaging along the core is useful to gain more significance.

### 3.3 Grain size and layer inclination measurements

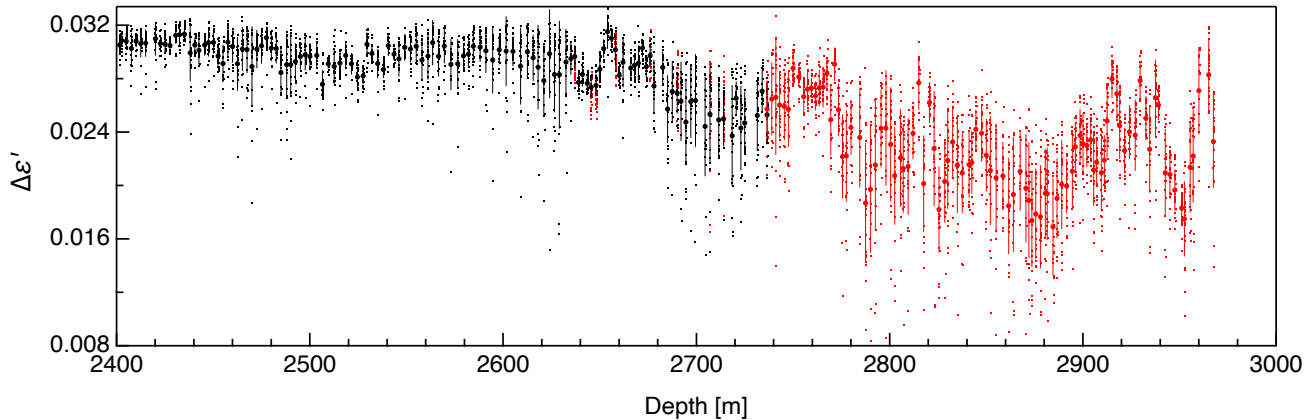
Grain sizes were measured at the DF site. Operators from the ice processing team observed the crystal grains by noting a faint difference in light reflectivity between grains and visible grain boundaries (hereinafter GB). While freshly cut surfaces did not exhibit such features, the ice cores in storage developed them over time due to the progress of sublimation. To measure the average surface area of each grain, we used three circular gauges with diameters of 10, 20, and 40 mm. The number of grains on the core surface within the circle of the gauge was counted. The number of crystal grains within each circle typically ranged from several to 20. The estimated error was up to 20%. This measurement was performed every 1.5 m to a depth of 2967.5 m. Below this depth, because of very large crystals, it was difficult to define grain size. Additionally, we visually investigated the growth of the inclination angle of the visible layers, such as cloudy bands or tephra layers, from the horizon using a protractor. A detail of the method is given in Appendix A3. In this process, core rotation resulting from core breaks was not considered. In addition to our preliminary report on this point (DFICPM, 2017), this study provides detailed data.

## 4. Results

### 4.1 Depth-dependent variation in measured $\Delta\epsilon'$ , corrected $\Delta\epsilon$ and SD values

Results on  $\Delta\epsilon'$  are presented in Figure 3. Examples of the continuous variation of  $\Delta\epsilon'$  along 0.5-m core segment are provided in Appendix C. Markers and bars indicate the average values and the standard deviations (SD) determined at 0.5-m intervals along the core sample. Dots represent raw data. Black and red symbols represent data obtained without and with inclined

290 measurement, respectively. Data from both cases (without and with horizontal sample inclinations within the resonator) in  
 291 agreement at overlapping depths (2630–2730 m), confirming the experimental principle that the horizontal rotation of the  
 292 samples in the open resonator give no influence on the measurement of the relative permittivity. We note that in the LO20%  
 293  $\Delta\epsilon'$  values have a large-scale tendency to decrease with increasing depth. The scatter of the raw data tends to be larger at greater  
 294 depths. We will discuss the detailed features after applying necessary corrections, using results from the Laue X-ray diffraction  
 295 measurements.



296  
 297 **Figure 3.** Results on  $\Delta\epsilon'$  in the LO20%. Dots represent raw data, recorded at every 0.02-m step. Markers and bars indicate the average values  
 298 and SDs for each 0.5-m step. Black and red markers/dots indicate data obtained without and with rotation of the samples in the open resonator,  
 299 respectively (see Figure 2).

#### 300 4.2 COF from The $c$ - and $a$ -axis orientation measured by the Laue X-ray diffraction method

301 Figure 4 presents examples of the COF  $c$ - and  $a$ -axis orientations obtained through thin-section the Laue X-ray diffraction  
 302 methods. Examples from 15 17 of the 43 42 measured depths are shown. In the diagrams, red dots and dark blue dots represent  
 303 the orientations of  $c$ -axis and  $a$ -axis within the space, respectively. The three panels, from left to right (views from 1 to 3),  
 304 represent  $c$ - and  $a$ -axis projected on the Schmidt equal net diagram are as follows. View 1: Horizontal view from the axis of  
 305 the microwave beam incidence (the center of the diagram), which is the same view as in Figure A2b in Appendix A2, without  
 306 information of the inclination angle or the horizontal orientation of the  $c$ -axes cluster. View 2: Horizontal view from the  
 307 orthogonal direction (axis) of the inclination angle. This view is attained by horizontal rotation of the system using the vertical  
 308 axis, by moving the center of the  $c$ -axes cluster to the periphery of the diagram. This operation relates to the horizontal  
 309 orientation. The center of the diagram is parallel to the girdle of the  $a$ -axes. This view corresponds to that in Figure A2b'.  
 310 View 3: View seen from the center axis of the  $c$ -axes cluster. In all diagrams, In the diagrams, red dots and dark blue dots  
 311 represent the orientations of  $c$ -axis and  $a$ -axis within the space, respectively. Additionally, green triangle markers indicate the  
 312 orientation of the vertical in the ice sheet. The fourth column (View 4) indicates normalized density  $\rho$  of the  $a$ -axis along the  
 313 girdle plane of the  $a$ -axis.  $\theta$  (degrees) is angle from the figure top of the View 3.

COFs The *c*-axis fabric generally exhibits a strong single-pole cluster. The strength of this cluster fluctuates with increasing depth. In contrast to observations in the UP80% (in Saruya et al., 2022b), the cluster strength becomes weaker at greater depths. Since each crystal grain of the hexagonal crystal lattice has three equivalent *a*-axes orthogonal to the *c*-axis, the distribution of the *a*-axes forms a girdle plane orthogonal to the *c*-axes cluster at each depth. As for the inclination angle, it is monotonically larger at greater depths down to 2967 m. Figures 4(k–o m–q) display data from the deepest five depths, which lie within the bottom 2% of the ice sheet. At each depth, red and blue number markers indicate the distributions of the *c*-axis and *a*-axis, respectively. Because of grain growth near the bed of the ice sheet, the largest number of crystal grains in a thin section was six. Therefore, the center of the clusters could not be determined with this very limited number of grains. In these five diagrams, we did not find any angular relations between neighboring grains. Both Except these five depths, both the inclination angle and the horizontal orientation of the *c*-axes cluster were extracted through the observation of COF *c*-axis fabric, considering views from 1 to 3. Both were used for the corrections from  $\Delta\epsilon'$  to  $\Delta\epsilon$ . We present correction procedures in Appendix B. In addition, the median inclination of the *c*-axes cluster values was calculated using the thin-section-based *c*-axis fabric data. Both the inclination angle and median inclination values of the *c*-axes cluster are presented in Figure 5f.

The *a*-axis fabric generally exhibits a strong girdle-type cluster on a plane. As with the fluctuations of the *c*-axis cluster, the strength of this girdle cluster fluctuates with increasing depth as well. Because of the three-equivalent *a*-axes orthogonal to *c*-axis for each crystal grain, the distribution of the *a*-axes in a girdle plane generally have periodicity of 60 degrees. We find in depth dependent profiles in View 4 that normalized density  $\rho$  of the *a*-axis along the girdle plane of the *a*-axis, exhibit strong inhomogeneity being dependent on  $\theta$ . In some cases, it indicates strong 60 degrees periodicity, which is evident in (b), (e) and (g) in Figure 4 and several more examples in the Supplementary information A. In other cases, it indicates superposition of variations with 60 degrees periodicity: examples are (a), (c), (h), and (k) in Figure 4. We discuss these clusters of the *a*-axes in this paper.

Distribution of *c*-axes of each thin section and *a*-axes anisotropy are further shown in Figures 5c and 5d. In terms of the distribution of *c*-axes, we can find crystal grains with *c*-axis oriented around 30–60 degrees at depths below 2600 m, in particular, except for the impurity-rich layer shown by brown shading. The *a*-axes anisotropy is defined as standard deviation of the *a*-axes density  $\rho$  (hereinafter,  $SD_\rho$ ) in panels 4 in Figure 4. Here larger value corresponds to the more anisotropic distribution of *a*-axes. We find that there are relatively small and large anisotropy in the impurity-rich layers and impurity-poor layers, respectively, and that the  $SD_\rho$  of the *a*-axis anisotropy exhibit large scale fluctuations with changes in glacial and interglacial periods. It is also very important to note that the  $SD_\rho$  is well synchronized with the grain size (Figure 5e), which implies underlining Physics.

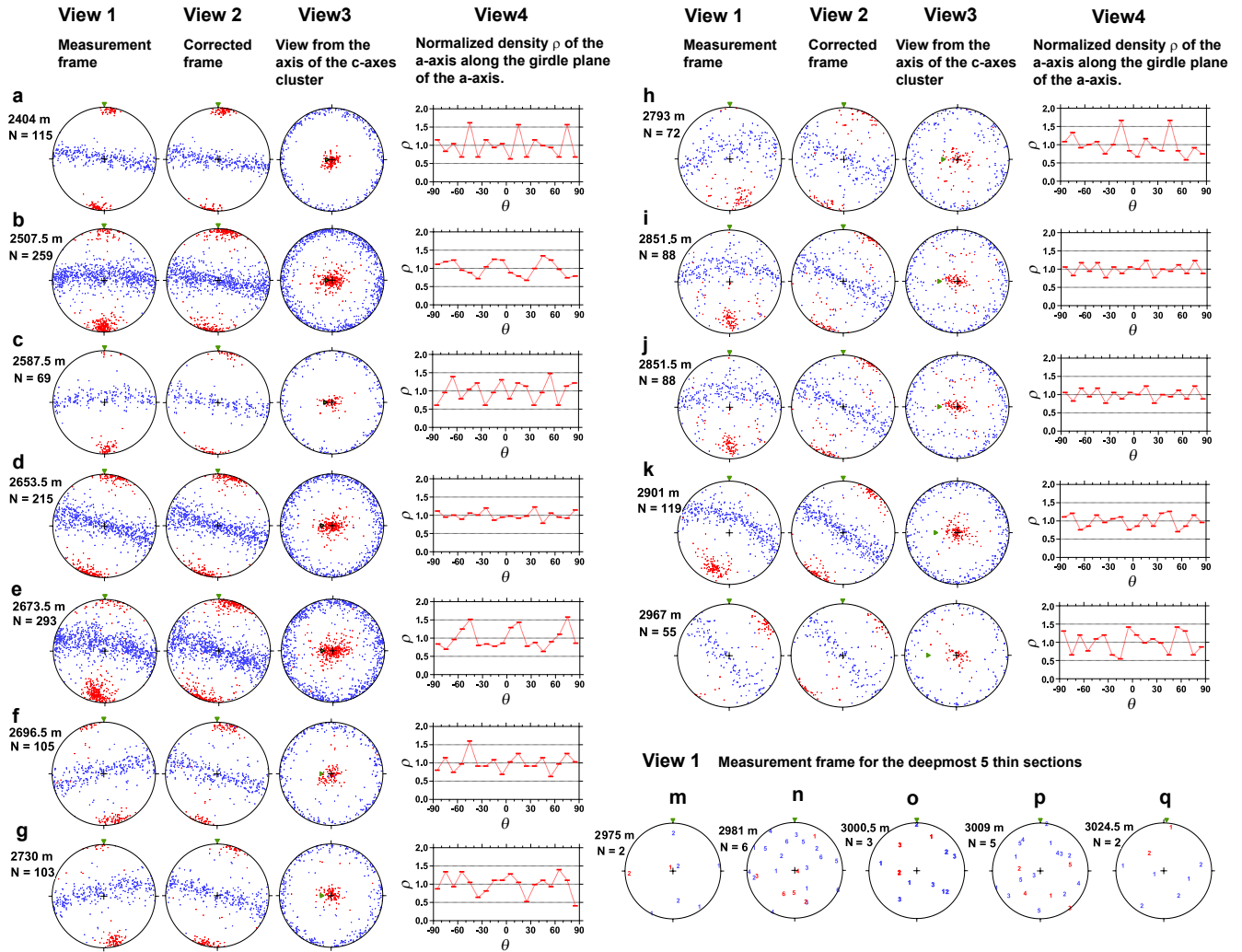


**Figure 4.** Examples of COF. The  $c$ -axis distribution data and  $a$ -axis distribution data obtained by the Laue X-ray diffraction measurements. 17 depths were selected from a total of 43 42. At each depth of the shallower 12 depths from (a) to (l) in depth range of 2400 and 2967 m, we show three Schmidt equal area net diagrams to express the distributions of  $c$ -axis and  $a$ -axis projected on it with red and blue colors for dots/markers, respectively. At each depth, red and blue colors for dots/markers represent the distributions of  $c$ -axis and  $a$ -axis, respectively, projected on a Schmidt equal area net diagram (e.g., Langway, 1958). Diagrams from (a) to (j) represent ten examples in depth range of 2400 and 2967 m. For these ten 12 depths, the left diagram (view 1) is the projection from the measurement frame (refer to Figure A2b). Center The second left diagram (view 2) is the projection from the corrected frame (see Figure A2b'). Right The third left diagram (view 3) is the projection from the center of the  $c$ -axes cluster. Green triangles in each diagram indicate the vertical orientation in the ice sheet. The vertical orientation aligns with the core axis. The fourth column indicates normalized density  $\rho$  of the  $a$ -axis along the girdle plane of the  $a$ -axis.  $\theta$  (degrees) is angle from the figure top of the View 3. Diagrams from (km) to (eq) represent the deepest five depths, ranging from 2975 to 3024.5 m. Because of grain growth near the bed of the ice sheet, number of crystal grains in each thin section was less than 6. Instead of dots, number markers were used to indicate the orientation of each grain.

### 4.3 Depth-dependent variations of corrected $\Delta\epsilon$ and SD values, and eigenvalues

We corrected from  $\Delta\epsilon'$  to  $\Delta\epsilon$  using both the inclination angle and the horizontal orientation of the  $c$ -axes cluster estimated from the Laue X-ray diffraction method. Correction procedures are presented in Appendix B. Figure 5a indicates corrected  $\Delta\epsilon$  values and eigenvalues obtained from Laue X-ray diffraction method. As with the Figure 3, markers and bars indicate the average values and the SD determined at 0.5-m intervals along the core sample. The relationship between  $\Delta\epsilon$  and eigenvalue is expressed as  $a_3^{(2)} = (2\Delta\epsilon / \Delta\epsilon_s + 1) / 3$ , assuming a single-pole fabric without horizontal anisotropy. Here,  $\Delta\epsilon_s$  represents the dielectric anisotropy of a single crystal. The  $\Delta\epsilon$  value (see Figures 5a) reaches approximately 0.031 at depth of 2430 and 2654 m. After reaching this maximum level, the  $\Delta\epsilon$  values decrease, accompanied by larger SD at greater depths (see Figures 5b). The  $\Delta\epsilon$  values fluctuate largely. The decrease in  $\Delta\epsilon$  values and larger SD are directly linked to the scatter in each individual  $\Delta\epsilon$  measurements (represented by dots in Figure 5a). When scatter is pronounced,  $\Delta\epsilon$  value averaged over each 0.5-m segment becomes smaller and the SD larger. At depths greater than about 2900 m, the  $\Delta\epsilon$  values exhibit greater fluctuations over distances on the order of 10 m. It is noted that when the SD values are large, each ice core displays numerous sharp negative spikes in  $\Delta\epsilon$ , as shown by the dots in the panel and an example profile in Figure C2.

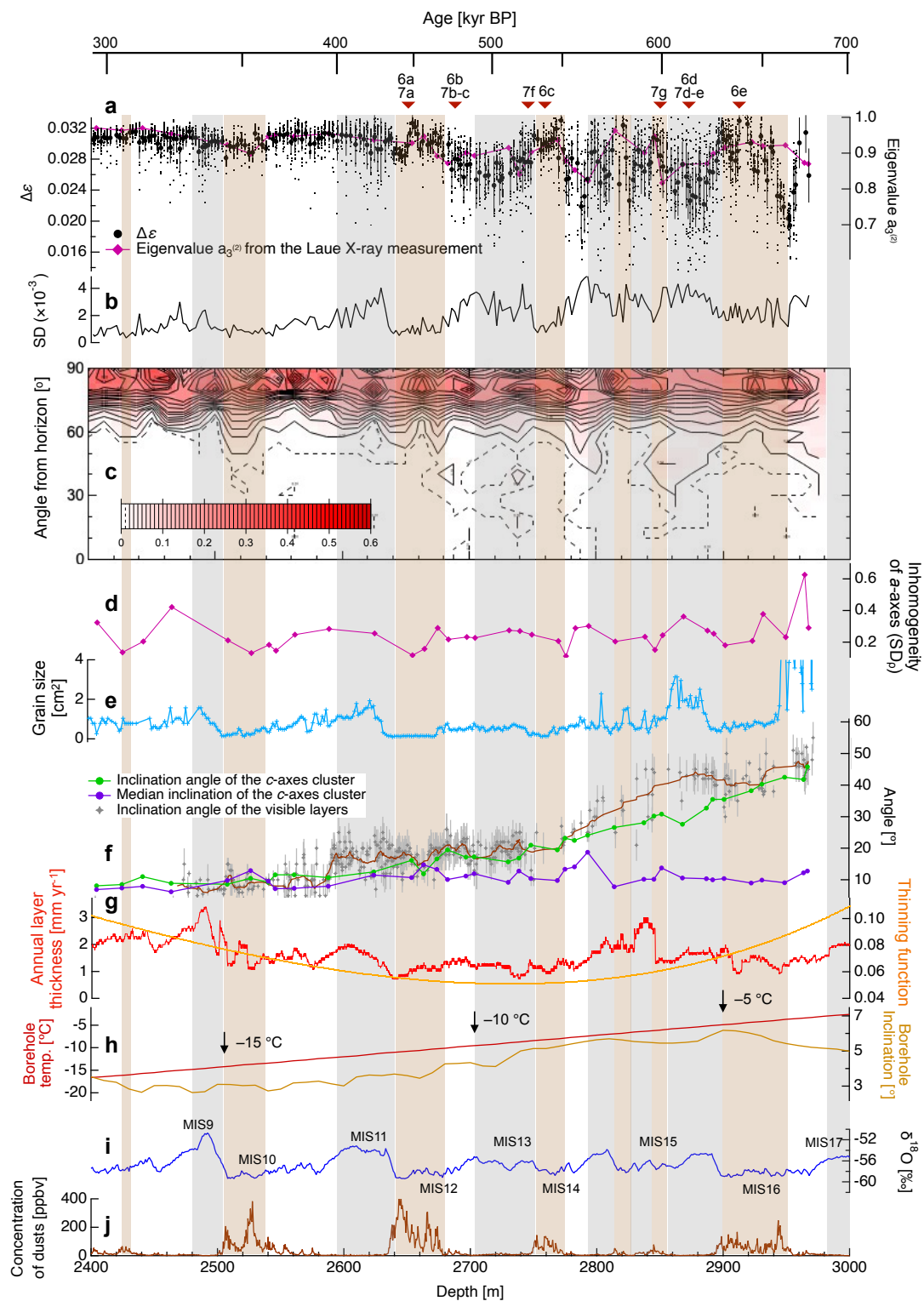


**Figure 5.** Detailed view of the comparison of  $\Delta\epsilon$  with various ice core data in the LO20%. (a)  $\Delta\epsilon$  (mean and raw data from DTM) and eigenvalues (from the Laue X-ray diffraction method). Possible uncertainty of the eigenvalues in terms of the total number of sampled grains are given in Appendix A4. (b) SD. (c) Distribution of  $c$ -axes as angles from a plane orthogonal to the cluster of  $c$ -axes. This was analysed using the data from the Laue X-ray diffraction method. The probability of the presence of  $c$ -axes is expressed with contour lines. (d) Inhomogeneity of  $a$ -axes shown as standard deviation of  $a$ -axes density  $\rho$  ( $SD_\rho$ ). (e) Grain size. (f) Inclination angles of the  $c$ -axes cluster and the visual layers (smoothing) and median inclination. (g) Annual layer thickness and thinning function (DFICPM, 2017). (h) Borehole temperature and inclination (Motoyama et al., 2020). (i)  $\delta^{18}\text{O}$  (DFICPM, 2017). (j) Concentration of dust particles (DFICPM, 2017). Gray and brown shading indicate interglacial periods and depths with a higher concentration of impurities (representing impure impurity-rich layers), respectively. The depths at which we observed the microstructure are indicated in the upper part.

#### 4.4 Grain size and layer inclination

The results for the grain sizes and inclination angle of the visible layers are presented in Figures 5e and 5f, respectively. The grain size tends to be larger during interglacial periods and smaller during glacial periods. The results for the grain sizes and inclination angle of the visible layers are presented in Figures 5e and 5f, respectively. Grain size tends to be larger during interglacial periods and significantly smaller during glacial periods, with this difference becoming more pronounced at greater depths. We observed that  $\Delta\epsilon$ , SD of  $\Delta\epsilon$ , and grain sizes are approximately synchronized, implying the presence of common underlying mechanisms. In grain sizes we could observe only weak increasing trend versus depth. The grain sizes at depths between 2900 and 2950 m remain small despite temperatures higher than  $-5^\circ\text{C}$ . At depths greater than 2950 m (in the deepest approximately 2%), the grain sizes become extremely large. Grain size profile within the entire thickness is displayed in Figure 10e along with the grain size reported from the UP80% of the DF1 ice core (Azuma et al. 1999, 2000). We observe that in the UP80%, the grain size increased steadily, while in the LO20%, the grain size tends to fluctuate, showing a clear distinction between very small grains of impurity-rich layers and larger grains of impurity-poor layers. There is a transition of the data aspect at depth of about 2500 m.

The inclination angle of the visual layers will not be exactly consistent with the inclination angle of the  $c$ -axes cluster if simple shear strain occurs in the ice sheet. The simple shear in principle contains components of compression, extension, and rigid-body rotation of the system. In this case, an axis orthogonal to the shear plane and the inclination angle of the  $c$ -axes cluster will deviate. Indeed, we observed that the inclination angles of the  $c$ -axes cluster and visual layers deviate over a wide range of depths, deeper than about 2580 m (Figure. 5f). The deviation is pronounced at depths between 2800 and 2900 m. We also note that the inclination angle of the visual layers changes in stepwise manner at 2580 and 2770 m.

#### 4.5 Microstructure in the deep sections of DF ice core

##### 4.5.1 Microstructural features in glacial and interglacial periods

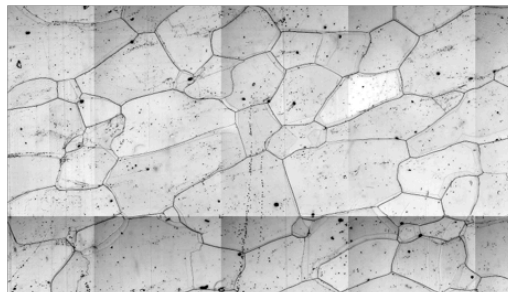
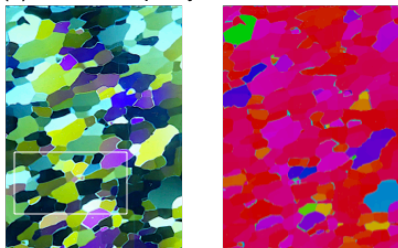
In the present study, we provide limited but significant examples of noteworthy microstructures in Figures 6 and 7. In Figure 6, five examples include impure impurity-rich ice (panel a: 2648 m,  $\sim 270$  ppbv dust concentration; panel c: 2759 m,

403 ~137 ppbv), less impure **impurity-poor** ice (panel b: 2685 m, ~10 ppbv; panel d: 2872 m, ~3 ppbv), and ~~impure~~ **impurity-rich**  
 404 deep ice (panel e: 2909 m, ~80 ppbv). Here, we use the term ~~impure~~ **impurity-rich** to mean that ice contains either insoluble  
 405 particles (like dust) ~~and~~ or soluble impurities such as dissolved ionic species. ~~It is noteworthy that the concentration of the less~~  
 406 ~~impure ice is markedly smaller than in impure ice. We provide polarized images, COF data of each grain obtained by G50,~~  
 407 ~~and microscopy images. The concentration of impurity-poor ice is distinctly lower than that of impurity-rich ice; the difference~~  
 408 ~~is significant. We provide images of ice thin sections viewed through crossed polaroids, *c*-axis fabric data for each grain~~  
 409 ~~obtained using G50, and microscopy images. Black solid thin lines in the microscopy image indicate GBs grain boundaries.~~  
 410 ~~GBs Grain boundaries~~ on the reverse side of a thin section are visible as thin lines. ~~Illustration of grain boundaries, grain~~  
 411 ~~boundaries on the reverse side, and subgrain boundaries are shown in Figure A3 in Appendix A5. The legend for COF *c*-axis~~  
 412 ~~fabric data is given as a by lower circle at the bottom of Figure 6. The color of each grain indicates the direction of *c*-axis~~  
 413 ~~orientation; the red color corresponds to the vertical direction means that the *c*-axis has an orientation in the vertical. Therefore,~~  
 414 ~~*c*-axis of red color grain is orientated toward the vertical direction. As for the *c*-axis orientation, at panels (a) and (c), we~~  
 415 ~~observe many small grains with *c*-axis orientation distinctly offset from the vertical direction (see *c*-axis fabric image). These~~  
 416 ~~are sparsely distributed. The size of such small grains range in the order of a millimeter or much less. Additionally, we observe~~  
 417 ~~that flattened (or, elongated in 2D) shape of grains that is slanting. These features were unique in the impurity-rich depths, and~~  
 418 ~~absent in impurity-poor depths. At panels (b) and (d), we observe much coarser grains with *c*-axis orientation distinctly offset~~  
 419 ~~from the vertical direction. Compared to the cases of the impurity-rich layers, these coarser grains occupy much larger areas~~  
 420 ~~in the image, with diameters of a few millimeters. In the two deepest samples (panels (d) and (e)), it is evident that the crystal~~  
 421 ~~grain boundaries tend to be distributed as more straight lines, and there are few subgrain boundaries. Panel (e) is a sample of~~  
 422 ~~impurity-rich layers; crystal grain is coarser compared to (a) and (c). However, some features of impurity-rich layers observed~~  
 423 ~~in panels (a) and (c) are persistently present in (e). That is, flattened grains have slanting features. Additionally, grains with *c*-~~  
 424 ~~axis orientation distinctly offset from the vertical direction occupy only minor area within the image.~~  
 425 As for the link between ice fabric eigenvalues and the microstructure,  $\Delta\epsilon$  values are significantly affected by volume  
 426 fraction of grains with *c*-axis orientation distinctly offset from surrounding grains. Coarser grain is more influential compared  
 427 to sparsely distributed smaller grains. An example ~~comparing  $\Delta\epsilon$  values with microstructure derived from thin section~~  
 428 ~~measurement of comparison them~~ is provided in Appendix C. ~~Since~~ ~~Because~~ the  $\Delta\epsilon$  values are volume-weighted averages  
 429 within the microwave beam, mean  $\Delta\epsilon$  values within a 0.5 m core sample decreases ~~more when there are more grains (in size~~  
 430 ~~and number)~~ with *c*-axis orientation distinctly offset from surrounding grains.

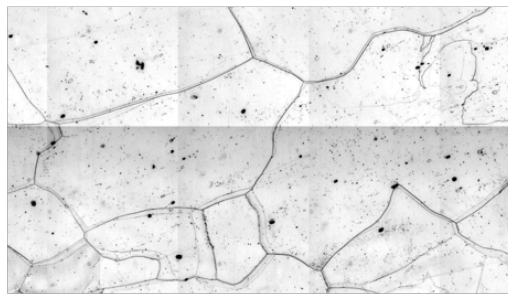
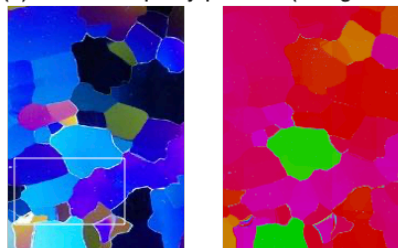
1. Polarized images 2. c-axis fabric images

3. Optical microscopy images

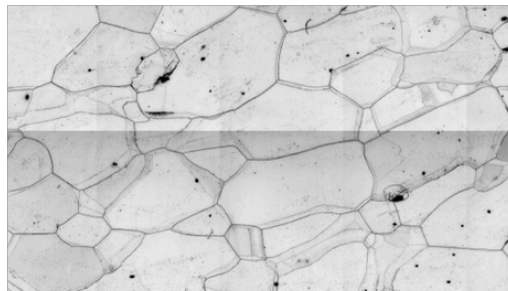
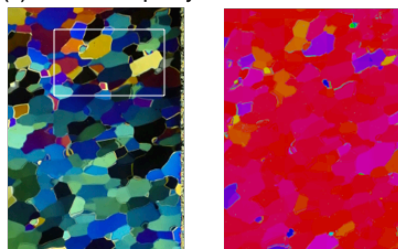
(a) 2648 m: impurity-rich ice



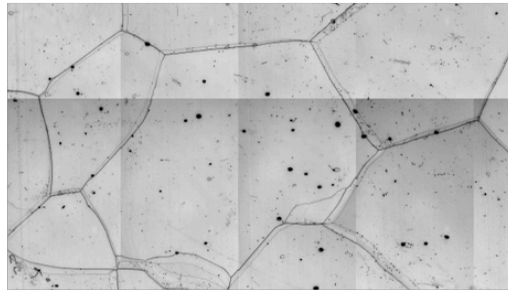
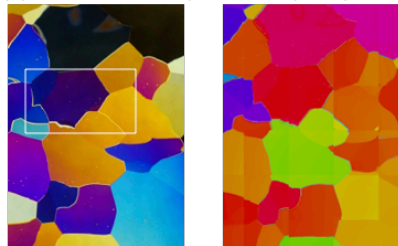
(b) 2685 m: impurity-poor ice (interglacial)



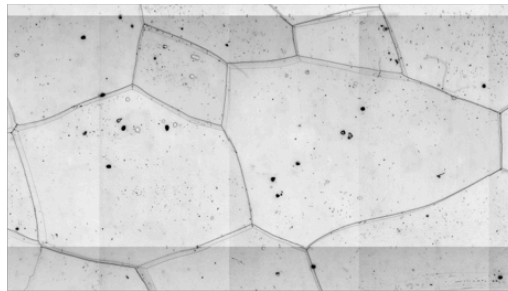
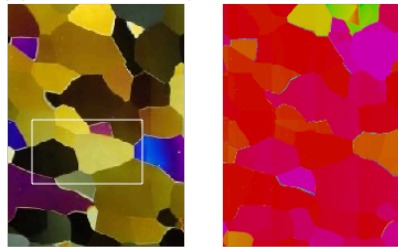
(c) 2759 m: impurity-rich ice



(d) 2872 m: impurity-poor ice (interglacial)



(e) 2909 m: impurity-rich ice



10 mm

c-axis orientation

2 mm

**Figure 6.** Microstructure images representing examples from five depths. Depths and types of ice are specified in the figure. For each depth, an images of ice thin section viewed through cross polaroids polarized image (left), a COF *c*-axis fabric image (center) and optical microscopy images (right) are presented. In the optical microscopy images, black solid thin lines indicate GBs grain boundaries. GBs Grain boundaries on the reverse side of a thin section are visible as thinner lines. White frames in the left column indicate the location of microscopy images shown in the right column, respectively. The For the *c*-axis fabric images in the mid column, the legend for COF *c*-axis orientation is given images is shown at the bottom. The color of each grain indicates the orientation of *c*-axis. Red color corresponds to the means that *c*-axis has the vertical orientation direction.

#### 4.5.2 Microstructures in the impurity-rich layer: grain elongation and smaller grain size Microscopic grain boundary sliding via microshear

Based on discussions above, in this section, we discuss the  $\Delta\epsilon$  value variations, focusing on microshear and dynamic recrystallization process. From microstructural observations, we identified interesting features in the impure layers (Figure 6): the crystal grains elongate, and their major axes incline away from horizontal directions. We introduce the term “microshear” to describe the localized stress/strain (Drury and Humphreys, 1988; Bons and Jessell, 1999; Faria et al., 2009). It is remarkable that the crystal grains in impurity-rich layers tend to be flattened, and their major axes incline away from horizontal directions. These features seem absent in surrounding impurity-poor (interglacial) layers. An example of the slanting and flattened grains is shown in Figure 7a. As for the grain flattening, we analyzed the aspect ratio of the short and long axis of a fitted ellipse in 2D, using ImageJ software. The aspect ratios were distinctly different between in the impurity-rich layer and in the impurity-poor layers. In the impurity-rich layers it ranged 1.9–2.0, while in impurity-poor layers it was smaller, 1.5–1.7. Detailed data in the LO20% are given in Table A4 in Appendix A5. They are displayed in Figure 9 along with the aspect ratio reported from the UP80% of the DF1 ice core (Azuma et al. 1999, 2000). We observe that in the UP80%, the aspect ratio increased steadily, while in the LO20%, the aspect ratio tended to decrease, showing a clear distinction between higher values of impurity-rich layers and lower values of impurity-poor layers. Transition from the increasing trend to the decreasing trend is at depths approximately 2500 m (Figure 9). These features of the transition are very similar to the case of the grain size, noted in section 4.4. Azuma et al. (1999) suggested that nucleation-recrystallization is not active above 2500 m depth and that deformation and rotation recrystallization affect the increasing trend of grain size and thus aspect ratio. However, below the transition at ~2500 m, situations are different in terms of nucleation-recrystallization, which we will discuss later in this paper.

Regarding the flattened features within the impurity-rich layers, Azuma et al. (1999, 2000) demonstrated growth of flattening of the grains in the UP80%, which is the basis of the aspect ratio shown in Figure 9. A similar 2D feature, known as the “brick-wall pattern” has been reported at the high-impurity ice layers of the Antarctic EDML ice core (Faria, 2009) but it has not been reported in the Antarctic EDC ice core. For the Greenland NEEM ice core, Kuiper et al. (2020) reported that fine-grained bands with flattened (or elongated in 2D) grains with aspect ratio of 2, which is as large as the maximum level in the DF core. For the EDML core, Weikusat et al. (2017) suggested that shear deformation is responsible for the flattened (or, elongated) grains. Faria et al. (2009) proposed that microscopic grain boundary sliding via microshear was a deformation

mechanism for making the brick-wall pattern. According to these authors, a condition favorable for the occurrence of grain boundary sliding is likely a combination of smaller grain size, the presence of significant stress, and higher temperature. Smaller grain size is often achieved by the presence of high impurity content. These conditions are typical in the impurity-rich layer of the deeper sections in ice sheets (Faria et al. 2009). On the one hand, in the LO20%, grain elongation becomes less pronounced in deeper sections as shown in Figure 6e (sample from a depth 2909 m) and Figure 9. We suggest that the flattened features remain, but they are weakened by recovery and recrystallization due to exposure of ice to high temperature close to melting point for time periods in the order of 105 years. Strength of the flattened feature is dependent on temperature (thus, depth) and impurity concentration.

Another feature in the ~~impure~~ impurity-rich layer is approximately constant grain size (Figure 5e). Constant grain size is observed in MIS10, 12, 14 and 16, where the concentration of dust particles is extremely high. The small size is clearly deviated from the growth trend in the UP80% (Figure 10e). This ~~constant~~ persistently small grain size in ice core is known as “steady state grain size” (e.g., Steinbach et al., 2017). It is believed that steady state grain size is achieved when normal grain growth counteracts rotation recrystallization regardless of the initial grain size (Jacka and Li, 1994). We ~~believe~~ suggest that the steady grain sizes in the ~~impure~~ impurity-rich layers established themselves after these layers had reached deeper depths. When the ~~impure~~ impurity-rich layers were at shallower depths in the past, grain size would have been inversely correlated with dust concentration. ~~Besides rotational recrystallization, GBS also contributes to grain size reduction by dividing large grains into smaller ones through the formation of new grain boundaries.~~

#### **4.5.3 Migration recrystallization and grain nucleation ~~Influence of nucleation and migration recrystallization on COF development~~**

In dynamic recrystallization processes, rotation recrystallization has minimal effect on COF ~~c-axis fabric~~ changes but reduces grain size ~~and the aspect ratio~~. In contrast, migration recrystallization can significantly modify COF ~~c-axis fabric~~ (e.g., De La Chapelle et al., 1998; Cuffey and Paterson, 2010). ~~In GN, new grains tend to form with a preferential orientation towards basal glide. As a result, new grains lead to a weakened concentration of the c-axis. When a difference in stored strain energy exists between a few neighboring grains, the GB grain boundary migrates towards the higher-energy grain (e.g. Faria et al., 2014b). During strain induced migration recrystallization, GBs grain boundaries sometimes become irregular, forming interlocking patterns (Duval and Castelnau, 1995; Faria et al., 2014b). GN decreases the mean grain size; in contrast, migration recrystallization increases the mean grain size by consuming a neighbor grain. Even when grain nucleation (GN) occurs in ice, its contribution to COF changes may not be immediately apparent in the volume-weighted average  $\Delta c$  values in the DTM. However, if such nucleated grains grow by incorporating water molecules from surrounding grains, the situation changes. Migration recrystallization significantly affects the  $\Delta c$  values if the grains having different c-axis orientations grow. Rotation recrystallization was observed at upper part of the DF and throughout of the EDC ice cores, but clear evidence of GN and migration recrystallization have not been reported in both ice cores (Azuma et al., 1999; 2000; Durand et al., 2009). In contrast, at the DF core, we found substantial instances of direct and circumstantial evidence.~~

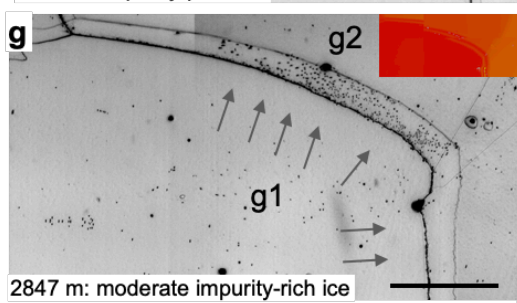
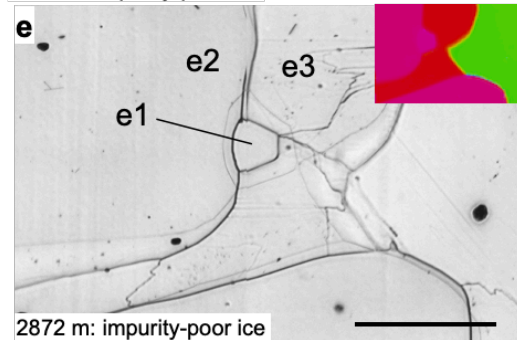
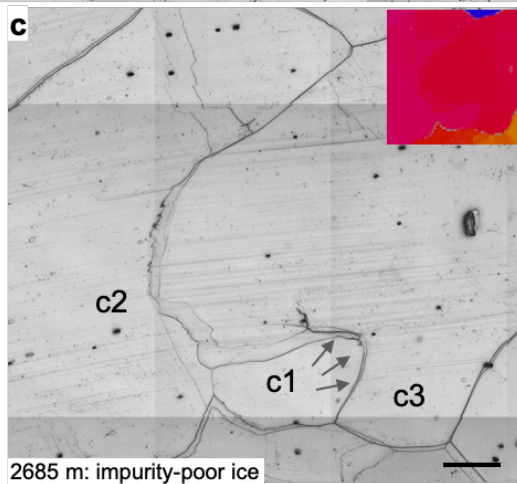
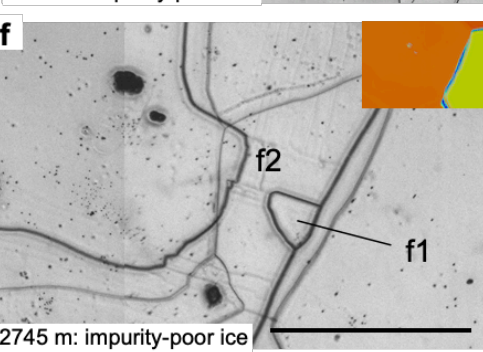
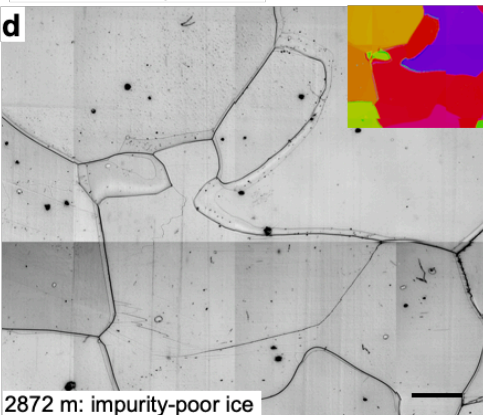
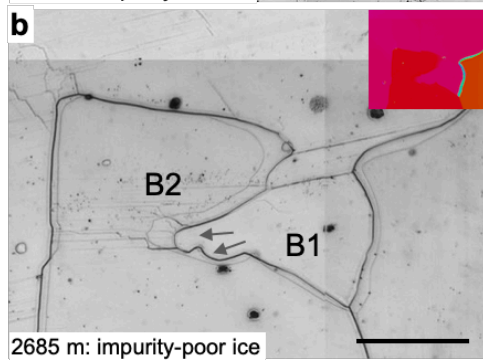
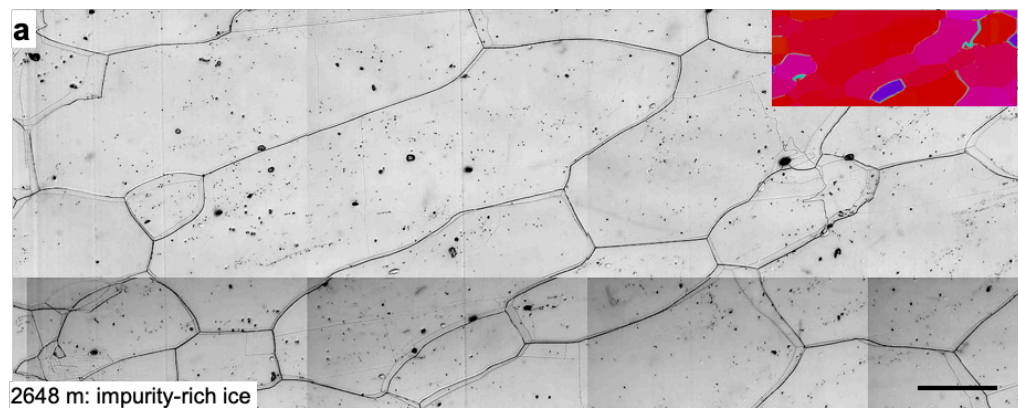
Microstructures indicative of dynamic recrystallization are depicted in Figures 12(c-i). We found migration recrystallization; migrating GBs are indicated with arrows. In panels e and d, small and squared grains (e1 and d1) with no internal structures can be nucleated grains. The orientations of the *c* axis in nucleated grains differ significantly from those in surrounding grains. Faria et al. (2009) mentioned that GN occurs at triple junctions or at GBs as two-sided grains. We observe grains satisfying these conditions at greater depths. In panel e, e1 grain migrates toward e2 grain. Migrating grain e1 lacks internal structures, while e2 grain has many sGBs. The presence of numerous sGBs implies high stored strain energy (Faria et al., 2014b). The lack of internal structures in grain e1 suggests a rearrangement of water molecules within its crystal lattice. Similarly, in panels f and g, we can observe migrating boundaries. In each panel, the migrating boundaries have irregular shapes, exhibiting interlocking features. The *c* axes of migrating grains (e1 and g1) deviate from the *c* axis clustering axis (i.e., vertical direction indicated in red). We propose that GN and migration recrystallization lead to significant changes in COF; a decreasing in  $\Delta c$  values and less clustered COF can be explained only by growth of grains with different *c* axis orientations. Such a situation would be impossible if migration recrystallization occurs without accompanying GN.

Figures 7b and 7c show examples from a depth of 2685 m presumably formed by strain induced migration recrystallization. In panel (b), top-left large grain (b1) has convex grain boundary toward adjacent grain (b2). In panel (c), bottom grain (c1) has convex grain boundary toward adjacent grain (c3). The presence of numerous subgrain boundaries implies highly and heterogeneously strained region (Faria et al., 2014b; Stoll et al., 2021a). Interlocking grains are shown in Figure 7d (sample from a depth of 2872 m). Grains with various *c*-axis orientation are intricately interwoven (see a *c*-axis fabric image). These features were well evident in impurity-poor layers. Contrastingly, in impurity-rich ice, grains with *c*-axis orientations distinctly offset from the vertical are present as smaller grains surrounded by larger grains (Figures 6a, 6c and 7a).

It is believed that grain nucleation occurs at triple junctions, at grain boundaries as two-sided grains, or similar regions characterized by high concentration of dislocation walls and subgrain boundaries (Faria et al. 2014b). We note that identification for a “just nucleated grain” is very difficult, as it requires time-series observations. Rather, when nucleation occurs, it may grow immediately after nucleation in natural ice samples; observation may be difficult. However, considering morphological features of the small grains with *c*-axis distinctly offset from surrounded by larger grains (Figures 6a, 6c and 7a), we suggest that these may be grains that nucleated at some timing of the deformational history of ice within the ice sheet.

Although there have been several studies investigating grain nucleation with artificially deformed ice (e.g., Montagnat et al., 2015; Chauve et al., 2017), there are not enough examples with natural ice samples. Faria et al. (2014b) suggested that a nucleated grain does not exhibit internal structures and bulges toward a region rich in dislocation walls and subgrain boundaries. Examples of grains with such features are shown in Figures 7e and 7f. Small grains with no internal structures (e1 and f1) are located at grain boundaries. In case of these grains (e1 and f1), they have *c*-axis orientations close to those of the adjacent grains (e2 and f2) (see *c*-axis fabric images in panels e and f). Nucleation of grains are further discussed in section 5 in this paper.

531 As a phenomenon associated with ~~GB~~ grain boundary migration, we ~~found~~ observed dust particles segregation (Figure 7g).  
532 Thin lines adjacent to ~~GB~~ grain boundary ~~are represent~~ the reverse side of the ~~GBs~~ grain boundary. ~~So~~ Therefore, microparticles  
533 are segregated on the ~~migration~~ planes of the crystal grains. ~~GB~~ Grain boundary migration in the deeper parts ~~would~~ likely  
534 leads to the redistribution of soluble impurities and dust particles.



c-axis orientation



**Figure 7.** Microstructure images for showing illustrating features of microshear and dynamic recrystallization-grain elongation and migration recrystallization. Images from seven five selected depths are presented. Depths are indicated in each panel and summarized at the top of Figure 5. All images were observed using vertical thin sections. Black solid lines indicate GBs grain boundaries. GBs Grain boundaries on the reverse side of a thin section are visible as thin lines. Black arrows in panels (a) and (b) indicate sGBs transitioning into GBs and quadruple junctions. Arrows indicate convex GBs grain boundaries. Color coding (COF c-axis fabric image) in each panel indicates the c-axis orientation of each grain. The legend for c-axis fabric images is displayed at the bottom right. Red-colored grains have a c-axis oriented vertically, while green or blue-colored grain are inclined horizontally. (a) and (b) indicate sGBs transitioning into GBs and quadruple junctions. (c) and (d): Examples of grains thought to have nucleated (2490 and 2872 m). Small and squat grains (e1 and d1) exhibit c axis orientations different from surrounding grains and lack internal structures such as slip bands and sGBs. Panels (e) to (g) show examples from a depth of 2685 m. Gray arrows from (e) to (h) indicate migrating GBs. (e): Top-left large grain (e1) grows toward adjacent grain (e2). Migration direction can be read by observing absence and presence of the sGBs or slip bands; migrations erase such features. (f): Central grain (f1) grows toward grains f2 and f3. At the boundaries between grains e1-e2 and f1-f2, we observe pinning by impurities. Boundary migration is restricted by impurities. (g): Top large grain (g1) grows toward bottom grain (g2) having much and complicated sGBs. Color coding in panels (e) to (g) indicates the c axis orientation of each grain. (a): Flattened (or elongated in 2D) and slanting grains observed in the impure impurity-rich layer. Panels (b) and (c): show Examples from a depth of 2685 m. (b): Small b1 grain has bulged (cuspidate) GBs grain boundaries. (c): Bottom c1 grain has bulged (cuspidate) GBs grain boundaries. (d): An example of interlocking grains (sample from a depth of 2872 m). Grains with various c-axis orientation are intricately interwoven each other. (e) and (f): Possible examples of grain nucleation (samples from depths of 2872 and 2745 m). Small grains (e1 and f1) exhibit lack of internal structures such as slip bands and sGBs subgrain boundaries, while adjacent grains have display many slip bands and sGBs subgrain boundaries. The small grains are located at GBs grain boundaries as two-sided grains. (g): Segregation of dust particles on along the front of a GB grain boundary at 2847 m depth. (i): Microstructure at 2907 depth. Quadruple junctions are indicated by black arrows. Although the concentration of dust particles is high, there are no evident brick wall patterns. Scale bars: 2mm.

## 5. Discussions

### 5.1 Variations in the layer structures in the deeper sections

#### 5.1.1 Temperature and stress conditions

In ice physics, it is well accepted that both plastic deformation and the molecular diffusion process in ice are highly temperature dependent (e.g., Petrenko and Whitworth, 1999). The conditions of ice sheets in Antarctica, in terms of temperature and stress, are located on a boundary zone between dislocation and diffusional creep on the deformation mechanism map (e.g., Shoji and Higashi, 1978; Goodman et al., 1981; Duval et al., 1983). When ice is under temperatures close to the melting point in the LO20%, its viscosity is lower, and diffusion coefficients are higher compared to the colder ice, the rate at which recrystallization occurs also increases with temperature in the upper layers (from 20 to 55 °C in the UP80%) by a factor of 10 to 10<sup>2</sup> (e.g., Petrenko and Whitworth, 1999). The recrystallization processes require thermally activated molecular diffusion; this condition exists in very deep ice. Regarding the stress field, the coring site is situated on a bank very close to a subglacial trench (Figure 1c). Between the subglacial trench and the coring site, the depth difference and

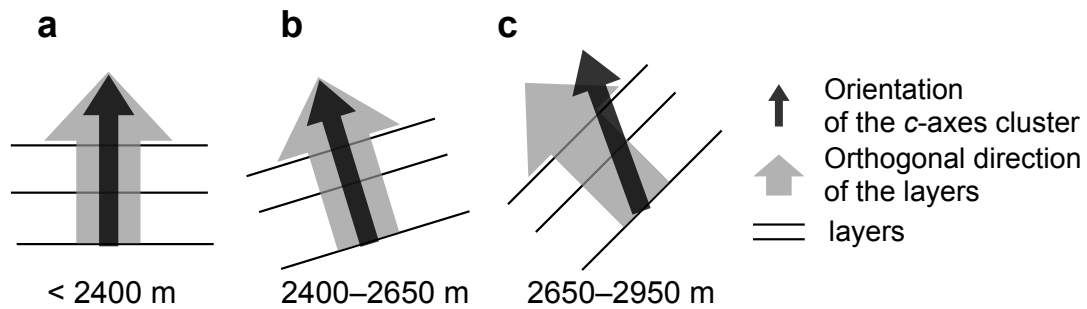
distance are each approximately 100 m each. This geometry corresponds with the maximum inclination angle of the *c*-axes cluster (approximately 45 degrees) and the inclination angle of the visual layers (approximately 45 degrees) near the base of the ice sheet (Figure 5f). In addition, the deeper trench may act as pathway for flow of subglacial water and the deeper bed is a location for more melt (e.g., Pattyn, 2010, Fujita et al., 2012). Thus, we hypothesize that there is a simple shear strain component directed towards the subglacial trench. The rheology of polycrystalline ice with a single-pole fabric is like that of the single crystal. It easily deforms under simple shear stress. We suggest that the simple shear stress dominates the deformation of ice at the bottom part of DF.

### 5.1.2 Relationships between the *c*-axis fabric and layer structure parameters

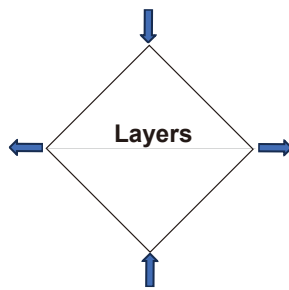
Figure 5 illustrates the relationships between *c*-axis fabric, layered structures, and physicochemical properties. The figure plots (a)  $\Delta\epsilon$  (mean and raw data from DTM) and eigenvalues (from the Laue X-ray diffraction method), (b) SD values, (c) the distribution of *c*-axes relative to a plane orthogonal to the *c*-axes cluster, (d) *a*-axes anisotropy within the girdle, (e) grain sizes, (f) inclination angle of the *c*-axes cluster and the visual layers, and median inclination, (g) the annual layer thickness and thinning function, (h) borehole temperature and inclination, (i)  $\delta^{18}\text{O}$ , concentrations of  $\text{Cl}^-$ ,  $\text{SO}_4^{2-}$  and  $\text{Ca}^{2+}$  ions, and (j) concentration of dust particles. The relationship between *c*-axis fabric, and layered structures evolves with increasing depth (Figures 5a–5f). Schematic diagrams of the relationships between layered structures and orientation of *c*-axes cluster are shown in Figures 8(a–c). The inclination angles of the visual layers and the *c*-axes cluster are approximately consistent at depths shallower than about 2600 m (Figure 5f). This indicates that the system, composed of visible layers and the *c*-axes cluster, rotated together as a rigid body. At depths deeper than about 2600 m, the consistency of the inclination angles in the visual layers and the *c*-axes cluster depends on glacial/interglacial periods. In glacial periods (MIS12, 14, and 16), both angles are approximately consistent, whereas in interglacial periods (MIS11, 13 and 15), they are not; the inclination angle of the *c*-axes cluster is smaller than those of the visual layers. This implies that the crystal grains undergo a simple shear mechanism, rotating less than layer structure rotation in these depth ranges, particularly during interglacial periods. In principle, simple shear is a superposition of pure shear and the rigid-body rotation of the system. The layer inclination is simply caused by the system's rigid-body rotation. Figures 8d and 8e illustrate 2D schematic explanation for configuration of strains and rotations in the ice body above the steep bedrock slope and near the bedrock. The *c*-axes also fall within the system's rigid-body rotation. However, the cluster of the *c*-axes alone will rotate backward due to the compression components within the pure shear by dislocation creep. Thus, the inconsistency of the angles is the evidence for dominance of the simple shear at this depth range. Such features were not observed reported in the EDC ice core. This suggests implies that these features are due to an environment specific to DF. In terms of the distribution of *c* axes (Figure 9c), we can find crystal grains with *c* axis oriented around 30–60 degrees at depths below 2600 m. It is believed that new grains tend to form with an orientation favorable for basal glide (Cuffey and Paterson, 2010), that is, approximately 45 degrees from compressional axis. We suggest that grains with a *c* axis orientation of around 30–60 degrees represent nucleated grains in the deeper part, and that these grains might

603 ~~grow and eliminate old grains by migration recrystallization. Such a process results in significant COF changes and more~~  
604 ~~occurrence of shear by dislocation creep. We discuss the details of recrystallization process in Section 5.3 in terms of~~  
605 ~~microstructure.~~

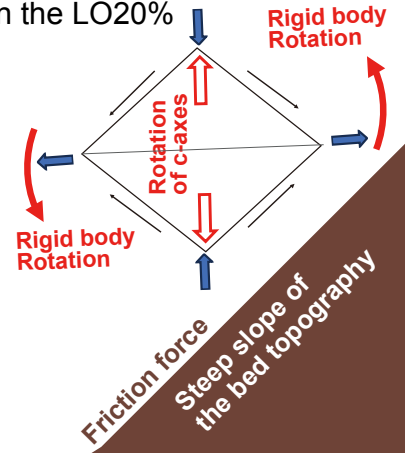
606 Next, we discuss layer thinning. DFICPM (2017) analyzed thinning function (the ratio of an ice layer thickness to its initial  
607 thickness at the surface) of the DF2 core from depth sequence of the climate signals and annual layer thickness (see Figure  
608 5g). The thinning function decreased to a local minimum at about 2750 m and then increased again towards greater depths.  
609 The authors hypothesized that spatially inhomogeneous basal melting might be linked to this anomalous thinning. In Figure  
610 5g, the broad local minimum of the thinning function is located at 2700–2800 m. This depth range agrees well with starting  
611 depths for large inconsistency between the inclination angles of the *c*-axes cluster **and the inclination angles of the layers**. ~~in~~  
612 ~~MIS16~~. Importantly, this depth is an approximate boundary where larger fluctuation of the  $\Delta\epsilon$  started. ~~In addition, both the~~  
613 ~~IACC and the IAVL have features of upward inflection at this depth range of glacial period of MIS 15.~~ We speculate that the  
614 observed phenomena were ~~caused by~~ **linked to** higher temperatures, thus the activated occurrence of recrystallization, and  
615 increased strain of simple shear from the bed. Then, we propose a scenario for development of the layer structure at the deeper  
616 part in DF based on the observed data using Figure 8f. An important point is that the DF drilling site is located just above a  
617 subglacial slope at the bank of the drainage pathway of the meltwater (Tsutaki et al., 2022). Under the dominance of the vertical  
618 normal stress near the dome, horizontal shear appears mainly on subglacial slopes rather than ridges or troughs (Tsutaki et al.,  
619 2022). Basal troughs are often influenced by basal melt or connected to deeper troughs of more basal melt. Consequently,  
620 troughs tend to serve as rapid pathways for ice flow. Thus, we suggest that the subglacial slope near the trough causes ice to  
621 flow towards the center of the trough, ~~disturbing~~ **shearing** the layered conditions. Furthermore, spatially inhomogeneous basal  
622 mass loss due to melting lead to an imbalance of force equilibrium in the vertical direction. Below the hardest ice, ice mass is  
623 lost locally at the base. As a result, layers can be stretched downwards, creating a convex shape centered around the location  
624 of the trough.



**d** Vertical compression  
In the UP80%



**e** Vertical compression  
Combined with simple shear  
In the LO20%



**f** Ice sheet surface

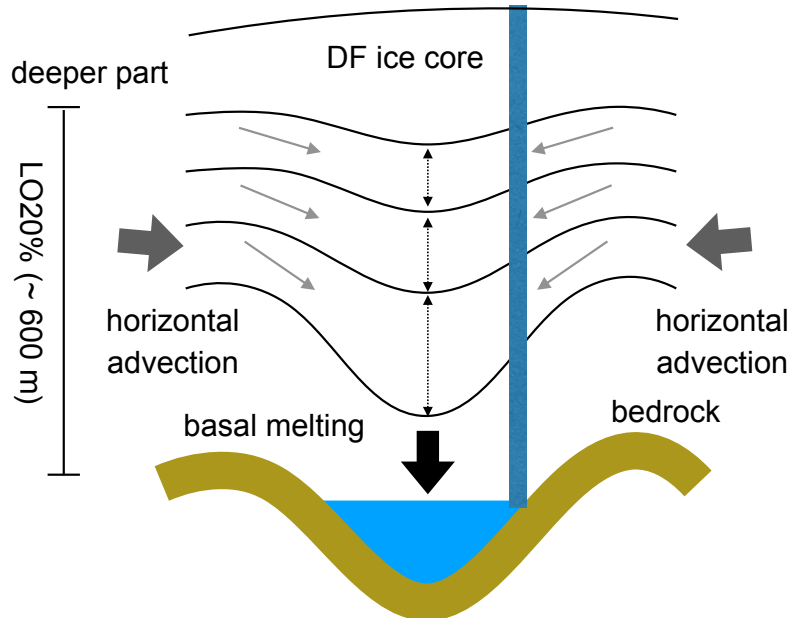


**Figure 8.** Schematic diagram of layered structures and 2D schematic explanation for configuration of strains and rotations in the ice body at Dome Fuji. (a–c) Diagram illustrating the relationship between layers and the orientation of the *c*-axes cluster. (a) Far above the bedrock, layers and the orientation of the *c*-axes are consistent, both oriented vertically. (b) Up to a depth of 2650 m, layers and the *c*-axes cluster rotate together as a rigid body. The directions of *c*-axis clustering and layers are consistent, yet they deviate from the vertical. (c) In addition to the rigid body rotation of the system, the cluster of *c*-axes rotates backward due to the compression component of pure shear. The orientations of the *c*-axes clustering and layers diverge. (d) and (e) Rectangular shape means a body of ice considered for deformation. Black thin arrows and blue bold arrows mean components of shear strains and normal strains. Bold red arrows indicate rigid body rotation of the system. Open red arrows indicate the axis toward which the cluster of the *c*-axes rotate. (d) A condition well above the bed, or in the UP80% in this paper. Uniaxial compression in the vertical dominates. (e) A condition under more influence from the bed topography, or in the LO20% in this paper. Because of the friction force between ice and bed, simple shear system rotates the entire system including the internal layers and the *c*-axes cluster together. However, because of the normal components of the strains (both compression in the near-vertical and extension near the horizontal plane), the all the *c*-axes thus the *c*-axes cluster rotates toward the vertical at the same time. This mechanism of the rotation in counter-direction works only for the *c*-axes and not to the layers. In this way, total amount of inclinations becomes larger for the internal layers than the cluster of the *c*-axes. (f) Schematic diagram of deep layered structure. The DF drilling site is located just above the subglacial slope at the bank (see Figure 1c), and horizontal shear along subglacial slopes appears in areas including the borehole near the trough. We suggest that the subglacial slope induces ice flow towards the center of the trough. Spatially inhomogeneous mass loss due to basal melting can lead to an imbalance in force equilibrium in the vertical direction. Layers can stretch downward, forming convex shape centered around the trough.

### 5.1.3 Variations in *c*-axis fabric and texture by the presence of insoluble impurities Relationships between COF with ionic impurities and dust concentrations

Within the UP80%, Saruya et al. (2022b) investigated the controlling factors of COF *c*-axis fabric by comparing  $\Delta\epsilon$  with various ionic impurities and dust concentrations. They found that  $\Delta\epsilon$  is correlated positively with the concentration of  $\text{Cl}^-$  ions and inversely with the amount of dust particles; the correlation grows markedly in a range from MIS5 to MIS8. In contrast to UP80%, the relationship between  $\Delta\epsilon$  and  $\text{Cl}^-$  ions within the LO20% was unclear. For the depths of the LO20%, we compared  $\Delta\epsilon$  with  $\delta^{18}\text{O}$ , grain size, and dust particles (Figure 5). Profiles of concentration of ionic impurities ( $\text{Cl}^-$ ,  $\text{SO}_4^{2-}$  and  $\text{Ca}^{2+}$ ) are plotted in entire depths figure (Figure 10). Referring to the  $\delta^{18}\text{O}$  profile, we observe that depressions in the mean  $\Delta\epsilon$  (caused by a large scatter of data points) occur during interglacial periods at depths below 2650 m; the depressions deepen with larger scatter of the raw data at greater depths. The relative sizes of SDs are smaller in glacial periods and larger in interglacial periods, respectively (Figures 5b). As for the ionic impurities we investigated, only  $\text{Cl}^-$  ions have a property to be easily substituted for the location of  $\text{H}_2\text{O}$  molecules in the ice crystal lattice (Jones, 1967; Jones and Glen, 1969; Nakamura and Jones, 1970). Dissolved and substituted  $\text{Cl}^-$  ions can increase density of the point defects in ice and promote dislocation movement, which will result in enhanced plastic deformation. Another characteristic of the  $\text{Cl}^-$  ions is their ability to be easily homogenized by diffusion through the ice lattice (e.g., Thibert and Domine 1997, Barnes et al., 2003, Fujita et al., 2016). Therefore, the influence of  $\text{Cl}^-$  ions on the deformation will be smoothed out and occurs in wider depths with time. In contrast to the softening effects

of dissolved  $\text{Cl}^-$  ions, dust particles are suggested to impede COF changes and thus deformation (Saruya et al., 2022b). The influence of dust particles on impeding deformation will remain since the dust particles do not diffuse easily. In our data from the LO20%, the relationship between  $\Delta\epsilon$  and  $\text{Cl}^-$  ions is unclear. That is, even at depths where the concentration of  $\text{Cl}^-$  ions is high, we did not find stronger  $c$ -axis cluster. The highly concentrated impurities had an apparent influence on the  $\Delta\epsilon$  values, maintaining a persistently high level of  $\Delta\epsilon$  below 2600 m (Figure 5a). Additionally, grain sizes tend to be small (Figure 5c), and the aspect ratio of the crystal grains remains consistently high in these layers, with values reaching up to 2 (Figure 9). Overall, these textural features—grain sizes, shapes, and  $c$ -axis fabric—are interdependent and strongly correlated with the presence of impurities.

According to the review by Stoll et al. (2021b) and a case study for NEEM ice core by Eichler et al. (2017), dust particles located not only at grain boundaries but also at grain interiors and triple junctions. To the best of our knowledge, the role of microparticles in ice deformation (dislocation creep) is not well understood. Production of dislocation is one of the possibilities. In contrast, microparticles may act as sink of dislocation like grain boundaries. In the former case, the smaller  $\Delta\epsilon$  values can be explained as a result of weaker clustering of  $c$ -axes due to restricted deformation. In the latter case, the smaller  $\Delta\epsilon$  values are also explainable as a result of the contribution of diffusion creep instead of dislocation creep. Even if ice is deformed significantly, diffusion creep does not leave any traces in the  $c$ -axis clustering. Saruya et al. (2022b) suggested two possibilities: (i) restricted deformation due to the inhibition of dislocation by dust particles and/or (ii) the contribution of diffusion creep that does not cause  $c$ -axis rotation because, with this mechanism, only molecules diffuse due to the condition of smaller grains. In the former case, the smaller  $\Delta\epsilon$  values can be explained as a result of weaker clustering of  $c$ -axes due to restricted deformation. In the latter case, the smaller  $\Delta\epsilon$  values are also explainable as a result of the contribution of diffusion creep instead of dislocation creep. Even if ice is deformed significantly, diffusion creep does not leave any traces in the  $c$ -axis clustering. Which effect ((i) or (ii)) is more dominant remains unresolved. However, in either case, they can restrict changes in  $c$ -axis clustering. What we observed in ice below about 2600 m is that the degree of  $c$ -axis clustering in the dusty (i.e., impure impurity-rich) layers is stronger than in the surrounding layers. Additionally, the consistently smaller grain sizes and higher aspect ratio of the crystal grains in the impurity-rich layers indicate that grain boundary migration is also restricted in such ice. This confirms that the movement of dislocations (as line defects) and grain boundaries (as planar defects) within the crystal lattice is significantly influenced by the presence of insoluble impurities. We suggest that these two unresolved mechanisms, related to restricted changes in the  $c$ -axis cluster, persist at depths below 2600 m, and that, in addition, dust particles have a strong influence on the occurrence frequency of dynamic recrystallization under higher temperature conditions in the LO20%.

To further explore the relationship of COF with ionic impurities, dust concentrations, and grain size, correlation coefficients ( $r$ ) and  $p$  values between them are given in Table 4. We analyzed each coefficient from data at 2.5 m intervals between 2400 and 2957 m ( $n = 216$ ) with data smoothing at 2.5 m intervals for the concentration of  $\text{Cl}^-$  ions, dust particles, and grain size. We found that SD is negatively correlated with  $\text{Cl}^-$  ion and dust particle concentrations and positively with grain sizes. This implies that fluctuations of COF depend on these parameters. Details about this dependence are discussed in the next subsection

(5.2.4). We also find, in contrast, that  $\Delta\epsilon$  is only weakly correlated with  $\text{Cl}^-$  and dust particle concentrations. Observing the brown shades in Figure 9, the variations of  $\Delta\epsilon$  values are apparently related to variations in dust particle concentrations in the impure layer below 2600 m. However, these variations are apparently unrelated in less impure layers. We suggest that this situation caused only weak correlations of  $\Delta\epsilon$  with  $\text{Cl}^-$  and dust particles. Interestingly, we find that grain size is clearly correlated with  $\Delta\epsilon$  and its SD. The development of COF is associated with recrystallization and grain growth, processes that are discussed in Section 5.3.

In addition to the  $\text{Cl}^-$  ions dissolved in ice and dust particles, as discussed above, we suggest that salt particles potentially influence COF development. Salt particles are known to exist solidly in ice cores at a volume fraction much larger than dust particles (Ohno et al., 2005). Depending on the type of salt particles, they have various eutectic points in the ice sheet. If the temperature condition is above each eutectic point, ions including  $\text{Cl}^-$  ions can be dissolved in the polycrystalline ice. However, we could not find any anomalous features in the data indicating the presence of additional COF changes. The phenomena seem complicated; little is known about the influence of salt particles or dissolved ions above eutectic points on deformation and microstructures.

Comparing the relationship of COF  $c$ -axis fabric with impurities in the UP80% with the LO20%, in the UP80%, more/less impure impurity-rich/poor layers have smaller/larger  $\Delta\epsilon$  values. In the LO20%, some thickness between 2400 m and 2650 m is a kind of transition zone; in it we find no clear correlation between  $\Delta\epsilon$  values and impurity. Below depths of about 2650 m, the trend is seemingly reversed. The COF  $c$ -axis fabric clustering strength exhibited substantial fluctuations. There, more impure impurity-rich layers maintain clustering persistently. In less impure impurity-poor layers, relaxation of the COF  $c$ -axis fabric clustering occurred, as represented by numerous negative spikes of  $\Delta\epsilon$ . A similar relationship exists between the aspect ratio and impurities in the UP80% and LO20% sections. In Figure 9, we observe an increasing trend in aspect ratio with depth in the UP80%. In contrast, the LO20% shows a distinct split in the data: an aspect ratio close to 2 in impurity-rich layers and much smaller values in impurity-poor layers.

In summary, the presence of insoluble impurities in the ice sheet has a significant impact on the  $c$ -axis fabric, grain size, and aspect ratio of crystal grains. In impurity-rich layers, particularly below 2600 m, grain boundary migration is restricted, leading to consistently smaller grain sizes and higher aspect ratios. The relationship between these textural features and impurities varies between the UP80% and LO20% sections, with a stronger correlation observed in the latter. These findings highlight the complex interplay between impurities and the deformation mechanisms within the ice, suggesting that the presence of insoluble particles plays a crucial role in controlling the microstructural evolution of deep ice.

Here, crystal grain size provides additional information regarding impurity. Grain sizes in ice sheets generally increase over time by thermodynamic process (e.g., Cuffey and Patterson, 2010). This implies that the grain sizes increase towards greater depths until nucleation mechanisms commence. However, grain sizes in DF (and EDC) ice have fluctuations along depths. Azuma et al. (1999, 2000) reported that the grain sizes in the DF1 ice core in the UP80% is correlated with  $\delta^{18}\text{O}$  variation and concentration of impurities, which was confirmed in this study (Figures 5 and 9). The same trend is common in the GRIP and Vostok ice cores (Lipenkov et al., 1989; Thorsteinsson et al., 1997). Thus, we can hypothesize that the physical

phenomena (grain growth, nucleation, and recrystallization) determined by deposition of impurities are common across a wide area of the ice sheet. This situation closely aligns with our suggestion that the COF profile is basically similar across a wide area of the ice sheet, primarily due to the deposition of impurities. The COF contains information on several factors: (i) deformational history, (ii) grain growth, and (iii) recrystallization (e.g., Cuffey and Paterson, 2010; Faria et al., 2014a, b). Ultimately, all these factors are sensitive to the deposition of impurities. Impurities restrict grain boundary migration through drag and Zener pinning mechanisms and also impede dislocation movement (Alley and Woods, 1996; Durand et al., 2006). These characteristics result in slow growth of COF clustering in impure layers within the UP80% and slow relaxation of COF clustering in the LO20%. This leads to an apparent reversed correlation between  $\Delta c$  values and impurity levels in both the UP80% and the LO20%.

#### 5.2.4 Small fluctuations in COF and related conditions

One clear advantage of DTM is its ability to estimate fluctuations over a unit length of an ice core, represented as SD. The correlation between the SD and detrended  $\Delta c$  data indicates that more/less deformed ice exhibits smaller/larger fluctuations within the ice core sample, respectively. We compared the SD values and detrended  $\Delta c$ , as well as concentrations of dust particles and  $\text{Cl}^-$  ions and grain sizes in Figure 11. We divided the time series graph into two segments, before and after 350 kyr BP, each with differently scaled inverted SD values on the left axis. Here, 350 kyr BP corresponds to a depth of about 2520 m. In each panel, black, red, brown, purple, and light blue lines indicate SD (with left axis), detrended  $\Delta c$ , concentration of dust particles, and  $\text{Cl}^-$  ions and grain sizes (with right axis), respectively. Note that the concentrations of dust particles and  $\text{Cl}^-$  ions, are and grain sizes represented on a logarithmic scale. We find that logarithmic concentration of dust and  $\text{Cl}^-$  ions and changes of grain sizes have variations very similar to inverted SD values. This similarity suggests that even a small amount of either dust particles or  $\text{Cl}^-$  ions (less than 30 ppbv for dust particles and 100  $\mu\text{g L}^{-1}$  for  $\text{Cl}^-$  ions), or both, significantly influence ice deformation during interglacial periods.

We propose that these correlations are explained as follows. Dust concentration is essentially a control factor for grain boundary migration and thus for grain growth. The SD can be large when restriction for grain boundary migration is weak. In deep zones such as the LO20%, nucleated grains have a significant impact on the large SD. Grain size can be explained with the same context; grains can grow more when restriction for grain boundary migration is weak. The correlation between the SD and  $\text{Cl}^-$  ions remains unclear. On one hand,  $\text{Cl}^-$  ions dissolved in the ice crystal lattice appear to have no direct physical link with grain size, as determinant factor is likely dust. On the other hand, concentration of  $\text{Cl}^-$  ions is probably related to concentration of salt particles that can affect grain boundary migration. In any case, we do not find possible physical bases as to why the SD is correlated to logarithm of dust, grain size or concentration of ions. Additionally, it should be noted that the densification of firn is also correlated with logarithmic concentrations of impurities (e.g., Freitag et al., 2013; Fujita et al., 2016). Jones (1967) suggested that the deformation of ice is most likely related to the logarithm of the ionic concentrations. There may be a common underlying mechanism.

#### 5.1.4 Cause of $\Delta\epsilon$ $c$ -axis fabric fluctuations inferred from microstructures

The  $c$ -axis fabric contains information on several factors: (i) deformational history, (ii) grain growth, and (iii) recrystallization (e.g., Cuffey and Paterson, 2010; Faria et al., 2014a, b). Ultimately, all these factors are sensitive to the deposition of insoluble impurities. Insoluble impurities restrict grain boundary migration through and Zener pinning mechanisms and also impede dislocation movement (Alley and Woods, 1996; Durand et al., 2006). These characteristics result in slow growth of  $c$ -axis clustering in impurity-rich layers within the UP80% and slow relaxation of  $c$ -axis clustering in the LO20%. This leads to an apparent reversed correlation between  $\Delta\epsilon$  values and impurity levels in both the UP80% and the LO20%. In terms of the distribution of  $c$ -axes (Figure 5c), we can find crystal grains with  $c$ -axis oriented around 30–60 degrees at depths below 2600 m. It is believed that new grains tend to form with an orientation favorable for basal glide (e.g., Alley, 1992; Humphreys and Hatherly, 2004; Cuffey and Paterson, 2010), that is, approximately 45 degrees from compressional axis. However, it is also noteworthy that, in Figure 5c, distribution of  $c$ -axis density approximately from 30 degrees from compressional axis (60 degrees from horizon) is always denser than 45 degrees or 60 degrees. It is possible that it has some underlying mechanisms in terms of nucleation recrystallization relative to the existing  $c$ -axis cluster. Additionally, crystal grains with  $c$ -axis oriented around 30–60 degrees tend to appear more in the impurity-poor zones where grain size is larger with low level of  $\Delta\epsilon$ . We suggest that these grains with a  $c$ -axis orientation of around 30–60 degrees represent nucleated grains in the deeper part, and that these grains might grow and eliminate old grains by migration recrystallization. At the same time, ice crystals will recover the  $c$ -axis orientations available for the continuation of dislocation-creep-based deformation.

We propose that grain nucleation and migration recrystallization lead to significant changes in crystal orientation fabric; a decreasing in  $\Delta\epsilon$  values and less clustered  $c$ -axis fabric in impurity-poor layers can be explained only by growth of grains with different  $c$ -axis orientations. Conversely, such grains are much smaller and limited in volume in the impurity-rich layer. Grain coarsening by migration recrystallization does not appear to occur since insoluble impurities restrict the grain boundary migration (e.g., Durand et al., 2006; Stoll et al., 2021b) thus growth of the nucleated grains as well. Therefore, the  $c$ -axis fabric change (decreasing of  $\Delta\epsilon$  values) caused by nucleation and migration recrystallization would appear strongly only in the impurity-poor layers. Thus, the dynamic recrystallization process would have greatly contributed to the characteristic behavior of  $c$ -axis fabric development. Even when grain nucleation occurs in ice both in impurity-rich ice and in impurity-poor ice, its contribution to  $c$ -axis fabric changes depend on the surrounding conditions: it may not be immediately apparent in the volume-weighted average  $\Delta\epsilon$  values in the DTM. However, when such nucleated grains grow, which is the case mostly in impurity-poor ice, subsequent strain induced migration recrystallization significantly affects the  $\Delta\epsilon$  values because of the growth of grains having different  $c$ -axis orientations.

#### 5.1.5 Variations in $a$ -axis fabric

Grain nucleation will also lead to significant changes in  $a$ -axis fabric. However, due to the lack of data on  $a$ -axes distribution in the UP80% section, we cannot determine the presence or absence of anisotropic  $a$ -axes organizations in this

792 upper section. Our observations are as follows: (i) In many depths within the LO20%, the girdle plane of the  $a$ -axis exhibits  
793 strong inhomogeneity depending on  $\theta$  (refer to the panels in View 4 of Figure 4 and Supplementary Information A). (ii) When  
794 the inhomogeneity of the  $a$ -axis within the girdle is expressed as  $SD_p$ , the  $SD_p$  tends to be larger in impurity-poor layers and  
795 smaller in impurity-rich layers (Figure 5). (iii) The  $SD_p$  is well correlated with grain size, aspect ratio, and  $\Delta\epsilon$  values (Figures  
796 5 and 9).

797 These observations raise several questions: (i) At what depths and how did this  $a$ -axis organization begin to form and  
798 develop? (ii) What is the physical mechanism behind this phenomenon—is it deformation, recrystallization, or a combination  
799 of both? (iii) What is the spatial scale of the  $a$ -axis organization? Is it limited to the scale of thin sections, or does it extend  
800 further?

801 Many of these questions cannot be conclusively answered with the current data alone. However, we can speculate based  
802 on our significant findings. In dislocation creep, if the slip plane is primarily the  $c$ -plane (the easy-glide plane of hexagonal  
803 ice), it is unlikely that  $a$ -axis organization occurs geometrically through  $c$ -plane slip. Since these processes do not seem  
804 interdependent, we exclude this possibility. The organization of the  $a$ -axis structure among these crystal grains can only occur  
805 due to interactions at the grain boundaries between adjacent crystal grains. Therefore, we speculate that dynamic  
806 recrystallization processes, particularly migration recrystallization associated with nucleation, play a critical role. The  
807 observations listed as (i) to (iii) at the beginning of this section support this speculation.

808 Unlike migration recrystallization, which can significantly modify  $c$ -axis fabric (e.g., De La Chapelle et al., 1998; Cuffey  
809 and Paterson, 2010), rotation recrystallization has a minimal effect on  $c$ -axis fabric changes but does reduce grain size and the  
810 aspect ratio. Similarly, it seems reasonable to think that rotation recrystallization has a minimal effect on  $a$ -axis fabric changes  
811 as well. Thus, we exclude this as a possible cause of the  $a$ -axis organization. We speculate that the new grains, with  $c$ -axis  
812 orientations distinctly offset from the single pole cluster, also have new  $a$ -axis orientations. When new crystal grains form  
813 through recrystallization, they arrange water molecules to form the most energetically favorable orientation, minimizing energy  
814 between the surfaces of the grains and forming  $a$ -axis alignment between adjacent grains. Here, we cite two papers by Matsuda  
815 et al. (1976) and Matsuda and Wakahama (1978) on the possibility of crystal twinning in ice sheets. Crystal twinning occurs  
816 when two or more adjacent crystals of the same mineral share some crystal lattice points symmetrically, forming an intergrowth  
817 of tightly bonded crystals. The shared surface is known as the twin plane or composition surface. Matsuda et al. (1976)  
818 investigated ice core samples from the Antarctic ice sheet near Cape Folger, revealing distinct crystallographic changes at  
819 specific depths. The ice layers exhibit a "diamond" pattern in  $c$ -axis orientations, indicating twinning relationships between  
820 crystal groups. The crystal structure of hexagonal ice has seven directions of oxygen-oxygen bonds, which are connected by  
821 hydrogen bonds, including along the  $c$ -axis. The angles between these bonds are equal to the tetrahedral angle of  $109.5^\circ$ . These  
822 authors determined the orientations of all seven oxygen-oxygen bond directions from the orientations of the  $c$ -axis and  $a$ -axis  
823 measured in polycrystals with a four-maxima "diamond" pattern  $c$ -axis fabric. As a result, it was found that 2 to 3 of the seven  
824 bonds in each crystal group were aligned with the bond directions of neighboring crystal groups. The alignment of oxygen-  
825 oxygen bond directions between neighboring crystal groups strongly suggests that the neighboring crystals might be in a

826 twinning relationship. Variations in grain size, texture, and crystallographic orientation are linked to deformation under high  
827 shear stress, with less deformation and twinning observed in certain layers, leading to characteristic *c*-axis patterns. Matsuda  
828 and Wakahama (1978) further investigated several types of polycrystalline ice of different origins. They suggested that a great  
829 majority of the adjoining crystals might be in a twinning relation. They suggested a strong possibility that the structural relation  
830 between crystals plays a major role in the appearance and growth of nuclei which have specific orientations during  
831 recrystallization.

832 These findings offer insights into the structural evolution of deep ice in response to stress and impurities; this crystal  
833 twinning hypothesis by these authors may apply to the current case of DF. Although we did not observe a four-maxima *c*-axis  
834 pattern at DF, crystal twinning likely occurs during nucleation and subsequent crystal growth, leading to share *a*-axis  
835 orientations between adjacent grains, even before the four-maxima pattern is concretely shaped.

836 Based on these speculations, we propose some answers to the questions posed earlier: (i) This *a*-axis organization likely  
837 began to appear and grow during periods of enhanced nucleation and migration recrystallization, particularly under higher  
838 temperatures in the LO20%. In the UP80%, this phenomenon is likely very weak. (ii) The most fundamental cause of *a*-axis  
839 rearrangement is nucleation and migration recrystallization, which relieves localized stresses. It is possible that crystal  
840 twinning, where some crystal lattice points are shared symmetrically, forms the *a*-axis organization to create the most stable  
841 thermodynamic conditions. (iii) The spatial extent of *a*-axis rearrangement is thought to be relatively limited, likely confined  
842 to a small region, such as the size of a single thin section or even smaller. This is because it is difficult to consider a far-  
843 reaching effect where distant crystal grains align with each other in terms of the *a*-axis. While the *a*-axes tend to align among  
844 adjacent and nearby crystal grains, it is natural to consider that the orientations formed in coordination become entirely different  
845 as the distance increases.

846 It is also noteworthy that a few deformation experiments on polycrystalline ice conducted in the laboratory have reported  
847 *a*-axis organization (Journaux et al., 2019; Qi et al., 2019; Wang et al., 2024). These experiments were conducted at  
848 temperatures near the melting point, with strain rates much higher (by about  $10^5$  to  $10^7$  times) than those in plateau region of  
849 the Antarctic ice sheet. A preferred *a*-axis maximum was detected in all these shear experiments. Additionally, natural  
850 examples from sheared ice under temperatures close to the melting point (Monz et al., 2021; Thomas et al., 2021) also exhibit  
851 a preferred *a*-axis maximum. These observations can be explained by the same speculation that the *a*-axis organizations were  
852 formed due to grain nucleation and migration recrystallization induced by shear strain under temperatures close to the melting  
853 point.

## 854 5.2 Development of the overall layered structures

### 855 5.2.1 Depth-dependent variations of $\Delta\epsilon$ in the entire core

856 Figure 9 shows  $\Delta\epsilon$ , its SD, and the aspect ratio across the entire core thickness. In the UP80%, both  $\Delta\epsilon$  and the aspect ratio  
857 increase with depth, reaching their maximum levels at the bottom. Below this, between approximately 2400 and 2650 m, the

858 trend changes, with both  $\Delta\epsilon$  and the aspect ratio showing larger fluctuations and sharp drops. The decrease in  $\Delta\epsilon$  values and  
859 the increase in SD are directly linked to the scatter in individual  $\Delta\epsilon$  measurements (represented by dots). Pronounced scatter  
860 results in smaller averaged  $\Delta\epsilon$  values over each 0.5-m segment and larger SD, with a corresponding decrease in the aspect  
861 ratio. At depths greater than about 2800 m,  $\Delta\epsilon$  values exhibit significant fluctuations over distances of about 10 m, and the  
862 aspect ratio remains at its smallest level.. Saruya et al. (2022b) argued that the linear trend of  $\Delta\epsilon$  in the UP80% was dominated  
863 by dislocation creep. A  $\Delta\epsilon$  value of about 0.031 implies that it is close to the  $\Delta\epsilon$  of a single crystal ( $0.0334 \pm 0.0007$  at  $-30^\circ\text{C}$ ;  
864 Saruya et al., 2022b). The state of the COF cluster with this  $\Delta\epsilon$  of about 0.031 is equivalent to the normalized eigenvalue  $a_3^{(2)}$   
865 of about 0.93 for a single pole COF. On one hand, it is well known that ice with a single pole fabric is resistant to strain in  
866 uniaxial compression axis configurations, as the basal planes of hexagonal ice have no room to slip for further strain. On the  
867 other hand, it is also evident that ice, even in the LO20%, continues to deform, as shown by analyses of thinning functions  
868 (e.g., DFICPM, 2017). The question then arises: What mechanisms dominate further deformation? We suggest three  
869 possibilities for mechanisms: (i) dominance of dislocation creep using slip systems other than basal plane slip within the  
870 hexagonal ice, (ii) dominance of diffusional creep, and/or (iii) dynamic recrystallization. These mechanisms can cause further  
871 deformation in ice with highly clustered COF. The first possibility is unlikely because it assumes extremely hard ice within  
872 the ice sheet, which does not align with the data. The second is also unlikely under a condition where we observe drastic  
873 changes of COF. In contrast, what we observe in the data is evident occurrence of dynamic recrystallization, typical for warmer  
874 ice, and continuation of dislocation creep using the slip system of the basal planes of hexagonal ice for grains that arise through  
875 recrystallization. We suggest that evidence includes a wide scatter of dots with low values of  $\Delta\epsilon$  in figures, leading to smaller  
876 average  $\Delta\epsilon$  values in interglacial periods, accompanied by large SD values. We interpret the wide scatter as indicative of grain  
877 nucleation and subsequent growth.

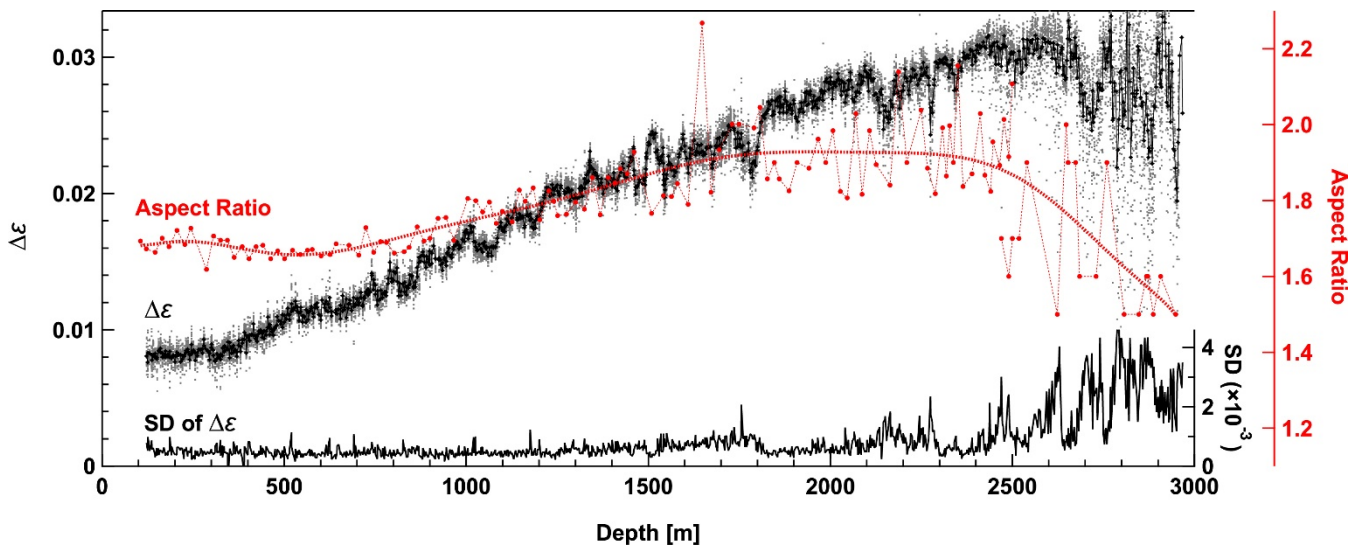


**Figure 9.** Variation of  $\Delta\epsilon$ , its SD, and the aspect ratio across the entire depth of the core is presented.  $\Delta\epsilon$  is shown as raw data (dots) and as mean values for each 0.5 m interval (markers). The dots represent  $\Delta\epsilon$  values at each 0.02 m step, and the SD corresponds to  $\Delta\epsilon$  values over each 0.5 m segment. Data from the UP80% are sourced from Saruya et al. (2022b), while aspect ratio data is indicated by red markers and lines. Data for the LO20% are from the current study of the DF2 core, and data for the UP80% are from the DF1 core (Azuma et al., 1999; 2000).

### 5.2.2 Comparison of COF *c*-axis fabric at deeper part of three summit ice cores

We extend our comparison of *c*-axis fabric data from DF with that of EDC. We first compare COF data from DF with that of EDC, representing two dome summits in Antarctica, separated by approximately 2000 km. It is notable that these two sites are similar in terms of glaciological conditions, including surface temperature, annual mean surface mass balance and ice thickness (see Table 2). Figure 10a indicates the relationship between  $\Delta\epsilon$  (averages and raw data as with Figures 5a) value and normalized eigenvalue  $a_3^{(2)}$  which can be expressed as  $a_3^{(2)} = (2\Delta\epsilon/\Delta\epsilon_s + 1)/3$ , assuming a single pole COF without horizontal anisotropy. Here,  $\Delta\epsilon_s$  represents the dielectric anisotropy of a single crystal. In the figure, we can observe the scatter of dots for the DF ice core. General trends in cluster strength and grain size are very similar in both ice cores across all age scales. Note that the sampling volume differs by a factor of  $10^2$  for each single data point between the thick section based DF data and the thin section based EDC data (Saruya et al., 2022b). In the bottom part of the EDC core, there is a correlation between the grain size and impurity concentration (Durand et al., 2009). However, no clear correlation between the COF and climate or chemical properties was reported. Furthermore, Durand et al. (2009) pointed out depth-dependent developments in COF *c*-axis clustering in deep sections are similar in the GRIP ice core (Thorsteinsson et al., 1997) and EDC core in Antarctica. Indeed, at the three summit sites, the depth zones where the maximum clustering appears are similar (see Table 2). The similarity among these three sites across both hemispheres implies that certain physical mechanisms are driving this similar development of COF *c*-axis clustering. We speculate that temperature profiles are primarily related to control enhancement of molecular diffusions and dislocation creep. We hypothesize that the temperature environment within the ice sheet, through mechanisms such as dislocation creep and recrystallization, might have resulted in the commonality of *c*-axis fabric at three points in the ice sheets. In this hypothesis, at the bottom of the UP80%, the thickness of ice is approximately 10% of the original ice equivalent thickness at the time of deposition (see Figure 5g). At this depth, the eigenvalue  $a_3^{(2)}$  reaches about 0.93. In the absence (or faint presence) of shear stress, a strongly clustered texture will be difficult, either to compress or shear, thereby necessitating dynamic recrystallization as an accommodation process. This state of saturation of the *c*-axis cluster, along with the common temperature range may be more effective as a condition to trigger nucleation and recrystallization. The deepest 10–20% of the polar ice sheets are typically characterized by their ability to easily deform under horizontal shear, due to high temperatures and well-clustered *c*-axis fabric. In these depths, dynamic recrystallization plays a critical role, particularly in impurity-poor layers, to recover the potential of *c*-axis orientations available for the continuation of dislocation-creep-based deformation.

911 An implication for this similar COF development is rheology of the ice sheet. The deepest 10–20% of the polar ice sheets  
 912 are typically characterized by their ability to easily deform under horizontal shear, due to high temperatures and well-clustered  
 913 COF. Within this thickness, the clustering strength of the *c* axes along vertical fluctuated in these ice cores. Thorsteinsson et  
 914 al. (1997) suggested that migration recrystallization might be the cause of COF fluctuations in the deepest part of the GRIP  
 915 core, although direct evidence was not observed. Migration recrystallization occurs when the temperature is close to melting  
 916 point (e.g., De La Chapelle et al., 1998; Humphreys and Hatherly, 2004) and the driving force for GB migration is stored,  
 917 which is achieved in the very deep parts of ice sheets. We observed evident features indicating the occurrence of migration  
 918 recrystallization (see Section 4.5 and Figure 6). These features imply presence of stored strain energy which induces the  
 919 migration recrystallization (Faria et al., 2014b). We therefore suggest that migration recrystallization predominantly occurs at  
 920 the dome summits of both ice sheets.

921 In the present study including Saruya et al. (2022b), we did not identify large anomalous step of *c*-axes clustering with  
 922 increasing depth (Figures 9, 10 and Appendix D). Rather, *c*-axis fabric exhibits fluctuations that appear already at a few  
 923 hundred-meter depth at Termination I. Thus, there is no indication attributable to presence of simple shear. This argument  
 924 differs with the existing scientific claim given by Durand et al. (2007). They suggested the impact of shear was important to  
 925 explain anomalous strengthening the *c*-axes cluster especially at the Termination II. In contrast to this earlier attribution to  
 926 shear, Saruya et al. (2022b) attribute small depressions of  $\Delta\epsilon$  values at MIS5e to the very low concentration of resolved Cl<sup>-</sup>  
 927 ion, which can substitute for the location of H<sub>2</sub>O in the crystal lattice, indicating that ice is harder because of it. This explanation  
 928 applies to the EDC case because, at EDC, most Cl<sup>-</sup> ions are lost to the atmosphere from snow compared to DF at least during  
 929 the Holocene (i.e., the interglacial period), while at Dome Fuji, they are preserved as NaCl and in solid solution (Oyabu et al.,  
 930 2020). These conditions suggest that ice becomes harder, preventing the *c*-axis cluster from strengthening at MIS5e as well.  
 931 In other words, this given an alternative explanation for the significant depression of the *c*-axis cluster at MIS5e and a notable  
 932 jump in the *c*-axis cluster at EDC. Additionally, further complexity arises because, at EDC, the surface mass balance (SMB)  
 933 contrast between glacial and interglacial periods is approximately 20% larger than that of DF (Fujita et al., 2015; Parrenin et  
 934 al., 2016), which will dilute Cl<sup>-</sup> ions more at EDC and also complicate ice flow models.

937 Table 2: Environment of the DF, EDC, and GRIP sites from dome regions in central plateau area of the ice sheets

Site	Elevati on (m)	Ice thickness (m)	Annual mean SMB (kg m <sup>-2</sup> y <sup>-1</sup> )	Annual mean surface air temperature (°C)	Depth of temperatur e at -10 °C (m)	Depth of maximum COF- <i>c</i> - axis cluster and corresponding temperature range (°C)	References
DF	3810	3028 (±15)	24–28	-54.4	ca. 2700	2400–2650 -18 to -12	This study, DFICPM, 2017, Oyabu et al., 2023,

							Yamanouchi et al., 2003
EDC	3233	3273 (±5)	25	−54.5	ca. 2800	2400–2650 −20 to −13	EPICA Community Members, 2004, Durand et al., 2009, Buizert et al., 2021 Dahl-Jensen, et al., 1993, 1998, Thorsteinsson et al., 1997
GRIP	3216	3085	230	−30.0	ca. 2960	2600 −28–20	

---

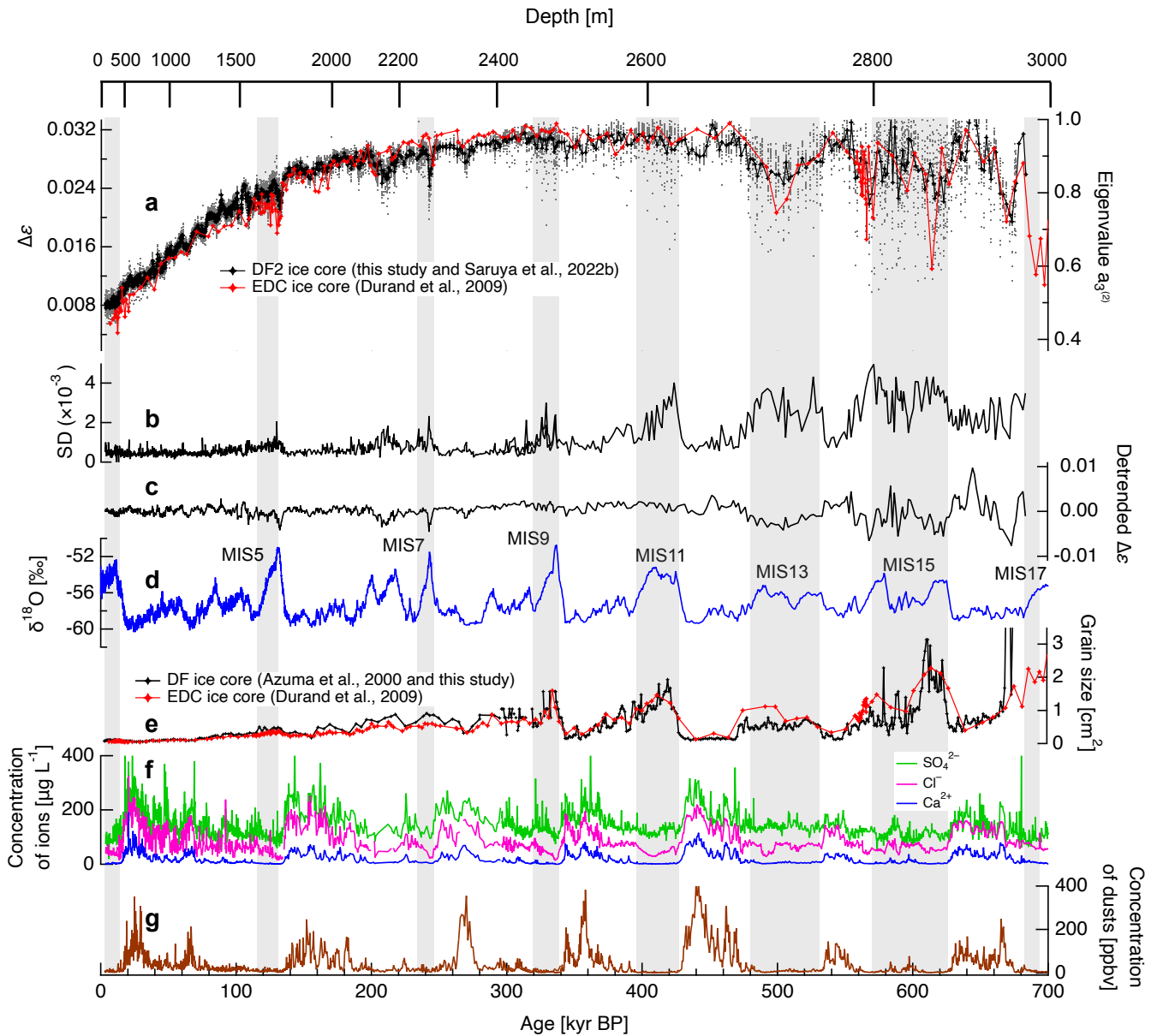


**Figure 10.** The COF **c-axis fabric** data and grain size data from the DF core and the EDC core are compared. Here, we applied the DF2021 age scale (Oyabu et al., 2022) for ages younger than 216 thousand years BP and the AICC2012 age scale (Bazin et al., 2013) for older ages. Light-gray shading indicates the interglacial periods. (a)  $\Delta\epsilon$  presented as raw data (dots) and as mean values for each 0.5-m segment (black markers for DF) or for each thin section (red marker for EDC). The right axis provides a scale for normalized eigenvalues. (b) SD for  $\Delta\epsilon$  in the DF core. (c) Detrended  $\Delta\epsilon$  values in the DF core. (d)  $\delta^{18}\text{O}$  in the DF ice core. (e) Grain size in DF cores (Azuma et al., 2000 and this

944 study) and EDC core (Durand et al., 2009). (f) Concentrations of  $\text{Cl}^-$ ,  $\text{SO}_4^{2-}$  and  $\text{Ca}^{2+}$  ions (Goto-Azuma et al., 2019). (g) Concentration of  
945 dust particles (DFICPM, 2017).

#### 946 **5.4 Zoning of COF development in the DF ice core**

947 Based on the profiles of physical properties (Figures 8 and 9), we propose characterizing the COF development of the DF  
948 ice core into five distinct zones. This zoning proposal aims to facilitate discussions about physical processes. (i) Ice sheet  
949 surface to bubble close off depth at approximately 100 m, categorized as the *firn zone*. (ii) Bubble close off to 2400 m,  
950 categorized as the *dislocation creep zone*. (iii) 2400–2650 m, categorized as the *transition zone*. (iv) 2600–2950 m, categorized  
951 as the *dislocation creep/recrystallization zone*. (v) 2950 m–bedrock, categorized as the *ice bed interface zone*. In the following,  
952 we summarize physical processes within these zones.

##### 954 i. ~~Ice sheet surface–bubble close off depth: *firn zone*~~

955 COF in firn is dominated by complex processes of metamorphism and initial deformation up to the bubble close off point.  
956 Initial conditions of snow deposition, such as accumulation rate, wind forcing, temperature and temperature gradient,  
957 have a large influence on the initial properties of snow (e.g., Colbeek, 1989; Inoue et al., 2023). The initial conditions in  
958 microstructures regarding COF were described in our previous paper (see Section 4.3 in Saruya et al., 2022b). In the firn  
959 stage, limited studies suggest that COF sometimes clusters around the vertical or is horizontally inclined at inland plateau  
960 sites in East Antarctica (e.g., Fujita et al., 2009, Calonne et al., 2017).  $\Delta c$  values of the DF cores at ~100 m depths are  
961 about 0.008–0.009 (Fujita et al., 2009, 2016). These values represent about 30% of the perfectly clustered COF. This  $\Delta c$   
962 value is the initial value for the subsequent zones.

##### 964 ii. ~~Bubble close off depth–2400 m: *dislocation creep zone*~~

965 The  $\Delta c$  values increase with increasing depth from approximately 0.008 to 0.031 in this zone. The large scale  
966 increasing trend is attributed to the rotation of the  $c$  axes towards compressional axis due to dislocation creep.

##### 968 iii. ~~2400–2650 m: *transitions zone*~~

969 This zone is characterized by a transition from the dominant deformation mechanism of dislocation creep to the onset  
970 of accompanying recrystallization processes. The  $\Delta c$  values reach maximum (approximately 0.031) and keep this high  
971 level in this zone. Additionally, fluctuations in  $\Delta c$  values are prevalent within this zone. Unlike the upper zones, the  
972 influence of bedrock topography starts to be apparent.

##### 974 iv. ~~2650–2950 m: *dislocation creep/recrystallization zone*~~

975 This zone is characterized by the predominance of recrystallization processes, which occur alongside the continued  
976 dislocation creep. As ice is deeper, the fluctuations of  $\Delta c$  values have a larger amplitude. In the impure layer, the  $\Delta c$

values remain at their highest levels; however, in surrounding less impure layers, the values are lower with numerous spikes of lower  $\Delta\epsilon$ .

v. 2950 m bedrock: *ice bed interface zone*:

The deepest 3% zone of the ice sheet very close to the bedrock. The bottom ice is meteoric (Ohno et al., 2016). Crystal grains are often larger than diameter of the ice core (94mm). Thus, it is difficult to make statistically meaningful COF measurements. The temperature approaches the pressure melting point, at around  $-2^{\circ}\text{C}$  (Motoyama et al., 2020). We infer that prolonged exposure (in the range of  $10^4$ – $10^5$  years) to this temperature has enhanced grain growth.

### 5.3 Implications for Ice Core Sciences and Radioglaciology **An overview of the layered structure of the ice sheet**

Based on the above discussions, we propose that polar ice sheets are massive bodies of ice, comprising alternating softer and harder layers, with layer thicknesses ranging from millimeters to those spanning glacial/interglacial periods. This situation has significant implications for ice core sciences and radioglaciology. The layered structures correlate directly with the vertical thinning of each layer, making them extremely useful for improving ice core dating models by providing constraints on strain values. Additionally, moving away from the dome, gravity driven shear movement of the ice sheet leads to inhomogeneous deformation between layers or layer zones, resulting in the formation of folds, faults, and mixing of ice across various layer thickness scales. For ice core sciences aiming to investigate continuous records of very ancient ice (on the million-year scale), choosing a drilling site at the dome is crucial. Drilling away from the dome area may lead to serious problems due to layer disturbances. Another implication of this discussion concerns the state of radio echoes from the very deep parts, specifically, the LO20% of the ice sheet. In glaciology, the presence or absence of echo-free zones is a topic of discussions (e.g., Fujita et al., 1999; Drews et al., 2009). In this study, we observed large fluctuations of  $\Delta\epsilon$  in a layered manner in the LO20% depth;  $\Delta\epsilon$  exhibited significant scatter in the less impure ice while the scatter was weak in the more impure ice. On one hand, the large scatter of  $\Delta\epsilon$  will lead to rather incoherent scattering of radio waves in radar sounding. On the other hand, there are distinct large-scale layers of  $\Delta\epsilon$  on glacial/interglacial age scales. The amplitude of changes in permittivity between such large-scale layers is sufficiently large to cause reflection coefficients leading to detectable radio echoes. From this perspective, we can expect coherent permittivity-based radio echoes from deep within the ice sheets. However, at DF, the layer was inclined by up to 45 degrees, a situation that prevents coherent scattering of radio waves. Moreover, moving away from the dome, continuous shear will disturb the preservation of layering, eventually forming radio-echo-free zones. From the perspective of this ice core study, we suggest that the presence of echo-free zones in wide areas away from the dome can be reasonably explained.

Based on the above discussions, we propose an overview of the layered structure of ice sheets. Polar ice sheets are massive bodies of ice, comprising layers with a wide variety of rheological characteristics, which are dependent on depositional features, that is, historical depositions of aerosols from the atmosphere. The thickness of layers ranges widely, from annual layers (millimeters) to those spanning glacial and interglacial periods. The initial ice fabric forms during firn processes (e.g., Calonne

et al., 2017; Fujita et al., 2009, 2016; Montagnat et al., 2020). Another fundamental factor, not covered in the current paper, is the content of ions that either enhance (Cl<sup>-</sup> and F<sup>-</sup>) or impede (NH<sub>4</sub><sup>+</sup>) deformation (Nakamura and Jones, 1970; Jones and Glen, 1969; Jones, 1967), as well as the presence of insoluble particles like salt inclusions, in addition to the dust particles discussed in this study. In ice physics, F<sup>-</sup> and NH<sub>4</sub><sup>+</sup> are well-known as major factors that modify the viscosity of ice crystals (as reviewed in textbooks by Petrenko and Whitworth (1999) and Fletcher (1970)). It must be emphasized that these ions can substitute for the location of H<sub>2</sub>O in the crystal lattice, thereby modulating the density and behavior of dislocations. These effects from ions are present in the ice crystal lattice from the firn process all the way to the bottom of the ice sheet. For example, Fujita et al. (2014) and Fujita et al. (2016) suggested that the rheology of polar firn is dependent on these ions. Additionally, it must be emphasized that salt inclusions have larger volume fractions than dust particles (Ohno et al., 2005).

Ice with these diverse initial properties, which will persist in the ice, experiences two distinct conditions in the upper 80% and the lower 20% of the ice sheet, as listed in Table 3. Four types of conditions affect the development of crystal orientation fabric, microstructures, and deformational regimes. These are: (i) temperature conditions, (ii) primary strain configurations, (iii) effects of insoluble particles (such as dust, metals, and salts) on texture, and (iv) processes of dynamic recrystallization, including the formation of new grains and migration recrystallization. Consequently, each individual layer has its own trajectory of deformational history over time periods spanning up to 106 years.

This overview has significant implications for practical applications, such as ice sheet modelling, ice core sciences and radioglaciology. Practical application for the ice sheet modelling is beyond the scope of this paper. However, these layered structures correlate directly with the vertical thinning of each layer, making them useful for improving ice core dating models by providing constraints on strain values. Additionally, at locations moving away from the dome, the increase in gravity-driven shear movement of the ice sheet causes inhomogeneous deformation between layers or layer zones, eventually resulting in the formation of folds, faults, and mixing of ice across various layer thickness scales. For ice core sciences, which aim to investigate continuous records of very ancient ice on the million-year scale, choosing a drilling site at the dome is crucial. Drilling at locations away from the dome area carries serious risks of layer disturbances near the bottom. Another implication of this discussion concerns the state of radio echoes from the very deep parts, specifically in the lower 20% of the ice sheet. In glaciology, the presence or absence of echo-free zones is a topic of debate (e.g., Fujita et al., 1999; Drews et al., 2009). On one hand, layers of *c*-axis ice fabric can cause the reflection of detectable radio echoes (e.g., Fujita et al., 2000). On the other hand, phenomena in the lower 20% will change the nature of ice for radio wave scattering. Concretely, reflections are more likely from large-scale layers corresponding to glacial/interglacial changes rather than shorter time-scale events. Additionally, layer disturbances accompanied with dynamic recrystallization may be observed as echo-free zones.

**Table 3.** Sequence of physical conditions of ice related to formation of crystal orientation fabric, texture and rheology within the ice sheet near dome summit in East Antarctica.

Depth range <sup>a)</sup>	Temperature condition (°C) <sup>a)</sup>	The primary strain configurations	Insoluble particles (such as dust and salt) slow down...	Influence of dynamic recrystallization on variation of crystal orientation fabric and texture
Depths of firm processes (0 – 100 m)	–55 <sup>a)</sup>	vertical compression	(unknown)	small
UP80% <sup>b)</sup> (100 – 2400m)	–55 ~ –16 <sup>a)</sup>	vertical compression <sup>c)</sup>	the formation of the <i>c</i> -axis clustering	small
LO20% <sup>b)</sup> (2400 – 3035 m)	–16 ~ melting point <sup>a)</sup>	vertical compression combined with simple shear	the relaxation of the <i>c</i> -axis clustering, and the decrease of the aspect ratio of crystal grains	formation of <i>c</i> -axis with orientations distinctly offset from the original <i>c</i> -axis cluster formation of preferred <i>a</i> -axis fabric, possibly due to crystal twinning the decreasing trend of the aspect ratio of crystal grains

- a) Numbers are all approximate ones.
- b) There is no sharp boundary between the UP80% and the LO20%. Rather, the transition occurs gradually and progressively.
- c) Vertical compression will be combined with simple shear progressively from deeper side if we move away from dome.

## 6. Conclusions

### *Use of the innovative methods for analysis of crystalline textures, and their outcome*

For enhanced understanding of layer structures and deformation regimes in polar ice sheets, we investigated the DF ice core using innovative analytical methods. Using the Laue X-ray diffraction method, we clarified detailed information about both *c*- and *a*-axes for each crystal grain. Microstructural observations provided signals of migration recrystallization and potentially nucleated grains. With the DTM, we provided COF *c*-axis fabric data with unprecedented sampling frequency, spatial resolution, continuity, and statistical significance. Furthermore, by combining data from these two methods, we clarified the COF layering of crystal orientation fabric in the LO20%. Coupled with previously reported COF *c*-axis fabric data in the UP80%, we obtained comprehensive and high-resolution COF *c*-axis fabric profiles for the core. Our major conclusions are summarized as follows: The complex sequence includes changes in depth range from the UP80% to the LO20%, and temperature variations from about –55°C to the pressure melting point. The primary strain configurations evolve from vertical compression to a combination of vertical compression and simple shear. Insoluble particles like dust influence the process by shifting from promoting the slower formation of *c*-axis clustering to inhibiting its relaxation. Moreover, the activity of dynamic recrystallization increases from less active to more active states. Including these, our major conclusions for each specific point are further listed as follows:

*Development of COF crystal orientation fabric, microstructure, and layering*

- (i) **Presence of transitions:** The Both the clustering strength of *c*-axes reached a maximum level at the bottom of the UP80% and in the transition zone (about 2400–2650 m depth), with large fluctuations below this zone, and fluctuated below 2650 m depth.
- (ii) ~~COF fluctuates over distance scales ranging from  $10^{-1}$  to  $10^2$  m, depending on the concentration of ionic impurities, particularly  $\text{Cl}^-$  ions, and dust. Across the entire concentration range in logarithmic scale, these impurities significantly influence COF and deformation.~~
- (iii) **The *c*-axis clustering fluctuation over short distances:** In the LO20%, the SD of the clustering strength within many 0.5-m ice segments is much larger than in the UP80%, indicating that COF the *c*-axis clustering fluctuation over short distances is enhanced in deeper sections.
- (iv) **Growth of the *c*-axis clustering, aspect ratio, and grain size:** In the LO20%, the SD of the clustering strength within many 0.5 m ice segments is much larger than in the UP80%, indicating that COF fluctuation in short distances is enhanced in deeper parts. In the LO20%, more impure impurity-rich layers maintain stronger *c*-axis clustering. In less impure layers, relaxation of the COF clustering occurs due to the emergence of new crystal grains with *c*-axis orientations distinct from the existing cluster, and dynamic recrystallization related to this emergence. Thus, dynamic recrystallization alters the COF of less impure layers. In impurity-poor layers, relaxation of the *c*-axis clustering occurs due to the emergence of migration recrystallization, altering both the *c*-axis and *a*-axis fabric of impurity-poor layers. In the LO20%, more impurity-rich layers maintain stronger *c*-axis clustering, larger aspect ratio, and smaller grain size. In impurity-poor layers, relaxation of the *c*-axis clustering, decreases in the aspect ratio, and growth of crystal size occur due to nucleation and migration recrystallization, altering both the *c*-axis and *a*-axis fabric of impurity-poor layers.
- (v) **The preferred *a*-axis fabric:** In the LO20%, *a*-axis fabric exhibited preferred orientation within the plane of the *a*-axis girdle, in a spatial scale of the thin sections used for the Laue measurements. Organization of the preferred *a*-axis fabric is enhanced in impurity-poor ice. Additionally, the enhancement of the preferred *a*-axis fabric is well correlated with grain growth.
- (vi) **Roles of the nucleation, the migration recrystallization, and the crystal twinning:** Signals of migration recrystallization, such as bulged and migrating GBs grain boundaries and interlocking grains, and probably nucleated grains were found in less impure impurity-poor layers. The appearance of new crystal grains with *c*-axis orientation divergent from the cluster decreases the degree of *c*-axis clustering. Crystal grains in impure impurity-rich layers showed an flattened (elongated in 2D) shape, with their major axes inclined from horizontal. These microstructures are unique to deeper sections and result from GBS via microshear. We argue that the migration recrystallization is the exact physical mechanism that caused the *c*-axis relaxation and the *a*-axis organization.
- (vii) **Presence of nucleation in the impurity-rich layers:** In impure impurity-rich layers, features indicating nucleation were observed. However, only weak signals of migration recrystallization were observed. The contrasting

microstructures between ~~impure~~ **impurity-rich** and ~~less-impure~~ **impurity-poor** layers are closely linked to the differing variations in cluster strength in each layer.

(vii) **Growth of the rigid body rotation:** The layer inclination angle shows stepwise changes at 2580 and 2770 m, being 10° at depths less than 2580 m, 20° at 2770 m, and reaching 45° at 3000 m. Similarly, the orientation of the *c*-axes cluster deviates from the vertical in deeper parts. Until a depth of 2700 m, the inclination angles of the *c*-axes cluster and layers are approximately consistent but deviate from the vertical. The system rotates due to simple shear strain as a rigid body, while the *c*-axes cluster alone rotates backward, resulting from the compression components of the simple shear.

#### *Common and unique features of sites: implications for wider areas in polar ice sheets*

(i) **Atmospheric aerosols primarily determine ice fabric fluctuations:** The fluctuations of the cluster strength versus ice age are common at DF and EDC, suggesting that depositional features ~~such as chemistry and dust from~~ **atmospheric aerosols** primarily determine these fluctuations. This suggests that ~~COF~~ ***c*-axis fabric** layering is essentially common across a wide area of polar ice sheets, if the deposition of chemical ions and dust is similar among sites.

(ii) **The similarity among three dome summit sites:** At the three summit sites in Antarctica (DF and EDC) and Greenland (GRIP), the depth zones where the maximum clustering appears are similar. The similarity among these three sites across both hemispheres may be related to ~~regardless of the~~ **commonality of** temperature condition along with the total amount of strain in the LO20%.

(iii) ~~In contrast to (i) above, features of layer inclinations in the DF ice core at greater depths were not observed in the EDC ice core, likely due to the DF drilling site's location above the subglacial slope at the bank of a drainage pathway for subglacial meltwater.~~

(iv) **Unusual thickening of annual layers near the base of the DF ice explained:** Unusual thickening of annual layers near the base of the DF ice core can be explained by the rigid body rotation of the system in the meridional direction near the bed of the ice sheet.

~~(v) COF development within the ice sheet was categorized into five zones.~~

(vi) **An alternative explanation for the depression of the *c*-axis cluster at MIS5e in EDC ice:** The significant reduction of the *c*-axis cluster at MIS5 in EDC is explained by the very low concentration of Cl<sup>-</sup> ions in the ice during this period and at this location.

(vii) **Implications for the nature of the very deep ice:** We argue that the bottom 45% **thickness** of the ice sheet **deeper than approximately 2600 m** plays a special role in shear deformation when the ice sheet moves away from the dome. Uneven strains between the layers will eventually compromise the integrity of the ice body in each part of the ice sheets. Consequently, folding, mixing, and faulting lead to the destruction of resolvable continuity in ice core signals, ~~resulting in radio echo-free zones at this thickness.~~ **Ice core drilling, aiming the ancient climatic records, at locations**

away from the dome area carries serious risks of layer disturbances near the bottom. Echo-free zones for radar sounding can be explainable as zones with layer disturbances accompanied with enhanced dynamic recrystallization.

These numerous findings warrant further examination for a better understanding. The new data and insights should link directly to key processes governing the flow of polar ice sheets. Expanding the knowledge from the dome summit to a three-dimensional dynamic layer structure within the ice sheet is a critical challenge. Deciphering radar sounding data in depth is key to this endeavor. The internal deformation of the ice sheet modulates flow based on COF crystal orientation fabric, ion concentration, and microparticle presence, leading to differential ice movement or disturbances like folds and mixing at various layer thickness scales. These factors can introduce positive or negative feedback, modulating the flow characteristics of the ice sheet.

#### *Data availability*

The data used in this paper will be published in the National Institute of Polar Research ADS data repository in conjunction with the publication of the present manuscript in The Cryosphere.

#### *Author contributions*

We list author contributions using a standard called CrediT (Ghan et al., 2016) to achieve greater clarity in contributions of all authors. TS: Conceptualization, Methodology, Validation, Formal analysis, Investigation, Data curation, Writing - Original draft, Visualization. AM: Conceptualization, Methodology, Validation, Formal analysis, Investigation, Data curation, Writing - Review & editing, Visualization. SF: Conceptualization, Methodology, Validation, Formal analysis, Investigation, Writing - Original draft, Supervision, Project administration, Funding acquisition. TK: Investigation, Writing - Review & editing. MI: Investigation. KG-A, MH, AH, YI, HO, WS, and ST: Writing - Review & editing.

#### *Competing interests*

The authors declare that they have no conflict of interests.

#### *Acknowledgements*

The authors are grateful to all the Dome Fuji Deep Ice Core Project Members who contributed to obtaining the ice core samples, either through logistics, drilling, or core processing. The main logistics support was provided by the Japanese Antarctic Research Expedition (JARE), managed by the Ministry of Education, Culture, Sports, Science and Technology (MEXT). This work was supported by JSPS KAKENHI Grant Number 18H05294.

1157 **Appendix A: Abbreviations**

1158 COF: crystal orientation fabric

1159 DF: Dome Fuji

1160 DFICPM: Dome Fuji Ice Core Project Members

1161 DTM: dielectric tensor method

1162 EFZ: radio echo free zone within polar ice sheets

1163 GB: grain boundary

1164 GN: grain nucleation

1165 sGB: subgrain boundary

1166 GBS: grain boundary sliding

1167 HOCC: horizontal orientation of the *c* axes cluster

1168 IACC: inclination angle of the *c* axes cluster from the vertical

1169 IAVL: inclination angle of the visible layers

1170 IPICS: International Partnerships in Ice Core Sciences

1171 LO20%: the lowermost (deepest) ca. 20% thickness zone within Dome Fuji or more generally in polar ice sheets

1172 MICC: median inclination of *c* axes with reference to the axis of the *c* axes cluster

1173 UP80%: the uppermost (shallower) ca. 80% thickness zone within Dome Fuji or more generally in polar ice sheets

## 1174 **Appendix A: Supplemental information for Method**

### 1175 **A1 Specifications the Two Resonators and Consistency of the $\Delta\epsilon'$ Values.**

1176 In this study, we utilized an open resonator for microwaves operating at frequencies between 26.5 and 40 GHz (Resonator  
 1177 No.1), differing from our previous study that used frequencies of 15 and 20 GHz (Resonator No.2) (Saruya et al., 2022a, b),  
 1178 especially in terms of ice core sample size limitations. Specifications of the two resonators, thickness and width of the samples  
 1179 are summarized in Tables A1 and A2, respectively. Using a high-frequency band allows for reduced sample dimensions due  
 1180 to the smaller beam diameter at higher frequencies. To verify the consistency between the current study (Resonator No.1) and  
 1181 the previous one (Resonator No.2), we conducted measurements of the  $\Delta\epsilon'$  across both frequency bands at depths of 2400 to  
 1182 2500 m. Figure A1 presents a comparison of the dielectric anisotropy profiles and the standard deviation for each 0.5-m  
 1183 segment, using approximately 23 data points (0.02-m intervals) measured by both Resonator No.1 and Resonator No.2. No  
 1184 systematic differences were observed between the two resonators, though the standard deviation was slightly higher in  
 1185 Resonator No.1, due to its smaller beam diameter. Grain numbers included in a Gaussian beam or in a thin section are listed  
 1186 in Table A3. Depending on number of crystal grains in a beam or thin section, statistical significance is different. In some  
 1187 cases, moving averaging along the core is useful to gain more significance.

1188

1189 Table A1: Specifications of the two resonators

Item	Curvature radius of the concave mirror (mm)	Distance between two mirrors (mm)	Scale diameter of the beam on the flat mirror (mm)	Frequencies (GHz)	Depths range (m)
Symbol	$R$	$D$	$\omega$	$f$	$z$
Resonator No.1	120	110	16	26.5– 40	2400–2970
Resonator No.2	250	225	38	14–20	100–2500

1190 Table A2: Thickness and width of the samples

Depths range (m)	Thickness (mm)	Width (mm)	Resonators used
2400–2500	35–37	53–58	No.1 and No.2
2500–2970	41–42	30–38	No.1

1191 Table A3: Grain numbers included in a Gaussian beam or in a thin section.

Measuring size and grain area	Dimension (mm)	0.1 cm <sup>2</sup>	0.3 cm <sup>2</sup>	0.5 cm <sup>2</sup>	1 cm <sup>2</sup>	2 mm <sup>2</sup>	4cm <sup>2</sup>
Thick-section-based method							
DTM No.1	~16φ × ~40	353	68	32	11	4	1
DTM No.2	~38φ × ~70	3490	672	312	110	39	14
Thin-section-based methods							
Laue X-ray diffraction method	100 × 45	450	150	90	45	23	12
microscopy and G50	90 × 50						

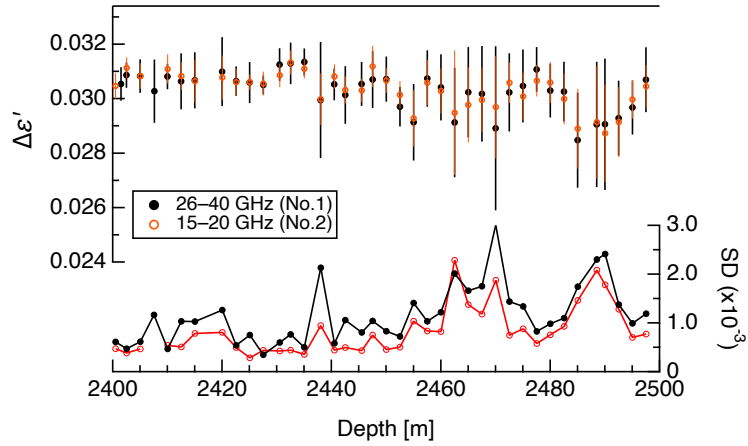


**Figure A1.** Comparison of the  $\Delta\epsilon'$  and standard deviation measured by Resonator No.1 (black) and No.2 (red).

## A2 Inclination of the $c$ -axes Cluster and the DTM

In the main text, Figure 2 was provided to explain the geometry of the sample and the open resonator. If the  $c$ -axes cluster aligns with the vertical (i.e., the ice core axis), it is relatively straightforward to set the angle between the  $c$ -axes cluster and the electric field close to about  $45^\circ$ . This was the case for ice shallower than approximately 2400 m (Saruya et al., 2022b). Figure A2 presents an example of this frame projected onto a Schmidt net. In this frame, the axis of the  $c$ -axes cluster is always orthogonal to the beam's incidence, thereby lying on the plane of the electric field vector. However, issues arise when the  $c$ -axes cluster deviates from the vertical. Depending on the inclination angle of the  $c$ -axes cluster from the zenith and the rotation of the cylindrical ice core in horizontal directions, the axis of the  $c$ -axes cluster may not align with the plane of the electric field vector (refer to Figure A2b). In such cases, the DTM detects permittivity components projected onto the plane of the electric field vector. These are non-principal components of the tensorial permittivity. Consequently, the raw data of non-principal components of dielectric anisotropy,  $\Delta\epsilon'$  (as shown in Figure A2b), is smaller than the principal components of  $\Delta\epsilon$  when the axis of the  $c$ -axes cluster aligns with the plane of the electric field vector. Correction of data from  $\Delta\epsilon'$  to  $\Delta\epsilon$  is possible only if both the inclination angle and the horizontal orientation of the  $c$ -axes cluster are known (see Figure A2b').

To enhance understanding of the measurement principles, Figure A2 is explained in greater detail here. Figure A2a depicts the case where the  $c$ -axes cluster of single pole fabric aligns with the vertical. The diagram's center represents the incident axis of the microwave beam in the resonator. Thus, the electric field vector is always orthogonal to the beam, spreading along the diagram's periphery. The dark blue plane contains the girdle of the  $a$ -axes. The red line represents a plane that includes both the beam axis and the  $c$ -axes cluster. In this setup, setting the electric field vector approximately within directions of  $\mathbf{E}_1$  or  $\mathbf{E}_2$  splits the vector components into two directions. This allows derivation of two permittivity components,  $\epsilon_v$  and  $\epsilon_h$ , as permittivities in the two principal axes along the diagram's periphery. Figure A2b illustrates a scenario where the  $c$ -axes cluster of single maximum fabric is inclined at an arbitrary horizontal orientation. The diagram's center is again the incident axis of

the microwave beam. The dark blue plane contains the girdle of the  $a$ -axes, while the red line is a plane containing both the beam axis and the  $c$ -axes cluster. The dashed line represents a plane perpendicular to the red plane and containing the beam axis. In this arrangement, setting the electric field vector approximately within rotated directions of  $E_1$  or  $E_2$  still splits the vector components into two directions. However, it results in two non-principal components,  $\epsilon'_v$  and  $\epsilon'_h$ , as permittivity. Knowing the inclination angle of the  $c$ -axes cluster ( $\theta$  in Figure A2b') and horizontal orientation of the  $c$ -axes cluster allows for accurate derivation of  $\Delta\epsilon$  values by rotating around the core axis to align the  $c$ -axis maximum within plane of the electric field vector (as shown in Figure A2b') and calculating the geometrical effects of the inclination angle of the  $c$ -axes cluster.

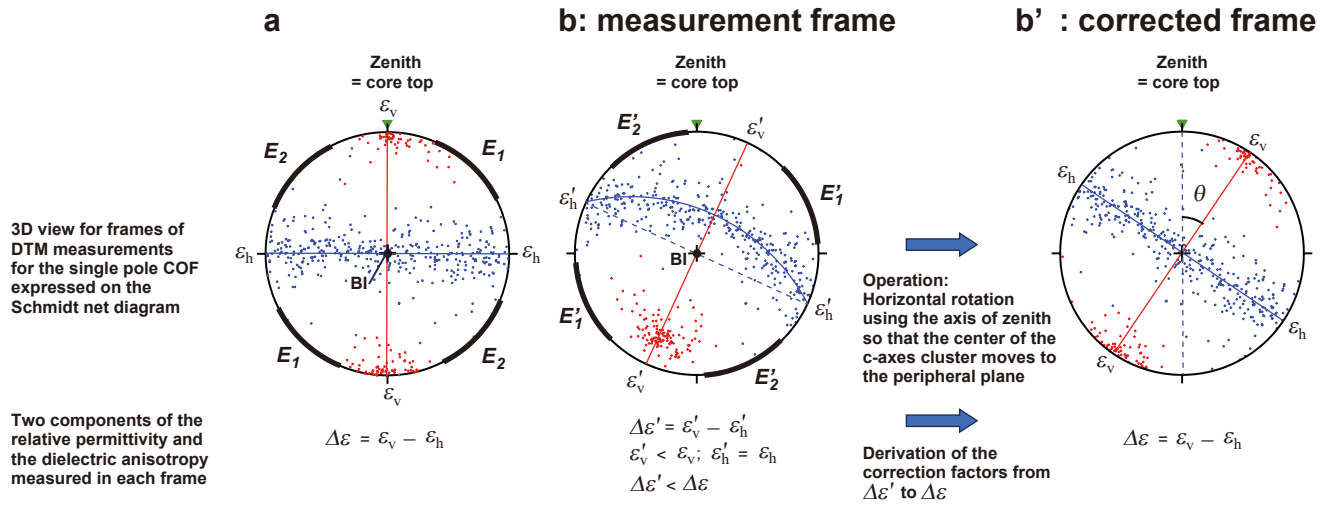


**Figure A2.** An explanation of the 3D geometry of systems composed of core samples, crystal axes, and applied electric fields, represented using projections on the Schmidt net diagram. For three figures from (a) to (b'), both  $c$ -axes (red dots) and  $a$ -axes (dark blue dots) are presented for an imaginary ice core sample. In (a) and (b), the center of the diagram represents the axis of incidence for the microwave beam, with the peripheral circle forming a plane orthogonal to the beam. The top of this peripheral circle corresponds to the vertical orientation within the ice sheet, which is also the top of each ice core. Case (a): The  $c$ -axes cluster of single pole fabric aligns with the vertical, and the  $a$ -axes girdle lies on the horizontal plane. If the microwave beam's electric field vector falls within the orientation ranges of  $E_1$  or  $E_2$ , it induces birefringence, allowing us to derive two components of permittivity,  $\epsilon_v$  and  $\epsilon_h$ , as principal components of the tensor. Consequently, we can calculate the difference as  $\Delta\epsilon$ . Case (b): Here, the  $c$ -axes cluster of single pole fabric is inclined to an arbitrary horizontal orientation. The girdle of the  $a$ -axes deviates from the beam axis. In this scenario, using the electric field vectors from (a) within the orientation ranges of  $E_1$  or  $E_2$  is ineffective for detecting birefringence, as the splitting of waves into two components is not equally balanced. However, if the microwave beam's electric field vector is within inclined range from  $E_1$  or  $E_2$ , namely  $E'_1$  or  $E'_2$ , balanced birefringence is achieved, and we can derive two non-principal components of permittivity,  $\epsilon'_v$  and  $\epsilon'_h$ . This results in the calculation of the non-principal difference as  $\Delta\epsilon'$ . Case (b'): This is the same as (b), but the system is horizontally rotated so that the  $c$ -axes cluster aligns with the periphery of the diagram where the electric field vector is located. By comparing permittivity values between cases (b) and (b') using the COF  $c$ -axis fabric data, we can determine factors to adjust  $\Delta\epsilon'$  values to  $\Delta\epsilon$  values.

### A3 Detail of the layer inclination measurements

1240 The inclination of the layers in the Dome Fuji ice core was measured using two methods, as follows: Thin, cloudy bands  
1241 are faint features with thicknesses ranging from about 10 mm to 1 mm. We observed the ice cores using a light stage,  
1242 approximately 250 mm by 600 mm in size, placed on a table. The ice cores, shaped as half vertical cuts of the original  
1243 cylindrical form, were visually inspected by observers who looked directly down at the core from above the light stage. The  
1244 ice cores were positioned between the observers' eyes and the light stage. The faint and thin cloudy layers are identified when  
1245 oriented vertically; only in this orientation do the observers recognize the layers as sharp lines. From angles deviating from  
1246 this, it is difficult to recognize such layers. By orienting the layers vertically and keeping them orthogonal to the core's  
1247 inclination on the light stage, the observers could measure and record the inclination angle of the ice cores using a large  
1248 protractor. With this procedure, layer inclination was measured in a 3D manner, and we always measured the maximum  
1249 inclination angle. In some cases, we employed another method where the observers used the coordinates of three or more  
1250 points in each layer within ice cores shaped as half of the core. Using these points, we measured the inclination angle of the  
1251 layers in 3D, ensuring the orientation was at the point of maximum layer inclination. At least two observers (in most cases,  
1252 Miyamoto and Fujita) measured the inclination angles for each layer as a cross-check. Additionally, we repeated measurements  
1253 several times to gain skills and confirm reproducibility. The observers estimated that the maximum errors in measurement  
1254 were about 5 degrees. The orientation of the inclination was not recorded because core orientation was not a topic of interest  
1255 at that time. However, we checked if these two are in the same vertical plane or not. We conformed that the horizontal  
1256 orientation of the *c*-axes cluster and the normal axis of the layer inclination are within the same vertical plain throughout the  
1257 LO20%.

#### 1258 **A4 Estimation of the error range of the normalized eigenvalues for the *c*-axis fabric data obtained through thin-** 1259 **section methods**

1260 Generally, if the total number of grain samples is  $N$  (in our Laue example, ranging from about 50 to about 250), the addition  
1261 of a grain means the normalized eigenvalue can vary by about  $1/N$  at maximum. When *c*-axes are clustered, as in the Dome  
1262 Fuji core, the range of variation will be much smaller than this  $1/N$ . Assuming each grain contributes an eigenvalue between  
1263  $2/3$  and  $1$  (see Figure 5a), the range of variation will be  $1/(3N)$  or less. Therefore, the total number of grains is very important.  
1264 The error in the eigenvalue is on the order of  $1/(3N)$  or less.

#### 1265 **A5 Microstructural observations**

1266 We analysed grain shape using ImageJ software. Table A4 shows the aspect ratio value defined as the ratio of the short and  
1267 long axis of a fitted ellipse. In the table, sample depths, concentration of dust particles, average and standard deviation of the  
1268 aspect ratio are listed. In some depths, we used several thin sections to obtain the number of crystal grains (indicated by  
1269 annotation). We found flattened (or elongated in 2D) grains in samples from depths of 2540, 2648, 2653.5, 2673.5, 2759.5 m.  
1270 (see brown shading in Figure 5). There, the aspect ratio ranges from 1.9 to 2.0. In contrast, the aspect ratio in deep impurity-  
1271 rich layers (samples from depths of 2907.5 and 2949 m) and impurity-poor layers ranges from 1.5 to 1.6. Shallower than a

1272 depth of 2600 m, depths of 2518.5 and 2540 m are located in impurity-rich layer (see Figure 5). The concentration of dust  
 1273 particles in 2518.5 m is not so high (~32 ppbv), so there is no evident elongation, and the aspect ratio is not large.

1274 Table A4: Aspect ratio of grains analysed by Image J software using thin sections. Sample depths, concentration of dust  
 1275 particles, grain number, average and standard deviation (SD) are listed. The columns with bold text correspond to the impurity-  
 1276 rich layer indicating slanting and flattened (or elongated in 2D) grains.

Depth [m]	2470	2490	2500	2518.5	<b>2540</b>	2623.5	<b>2648</b>	<b>2653.5</b>	<b>2673.5</b>
Concentration of dust particles [ppbv]	~3	~1	~7	~32	<b>~132</b>	~4	<b>~273</b>	<b>~221</b>	<b>~166</b>
Grain number	122 <sup>a)</sup>	90 <sup>b)</sup>	44	121	<b>167</b>	43	<b>335</b>	<b>238</b>	<b>244</b>
Average	1.7	1.6	1.7	1.7	<b>1.9</b>	1.5	<b>2.0</b>	<b>1.9</b>	<b>1.9</b>
SD	0.6	0.5	0.5	0.6	<b>0.5</b>	0.3	<b>0.7</b>	<b>0.6</b>	<b>0.6</b>

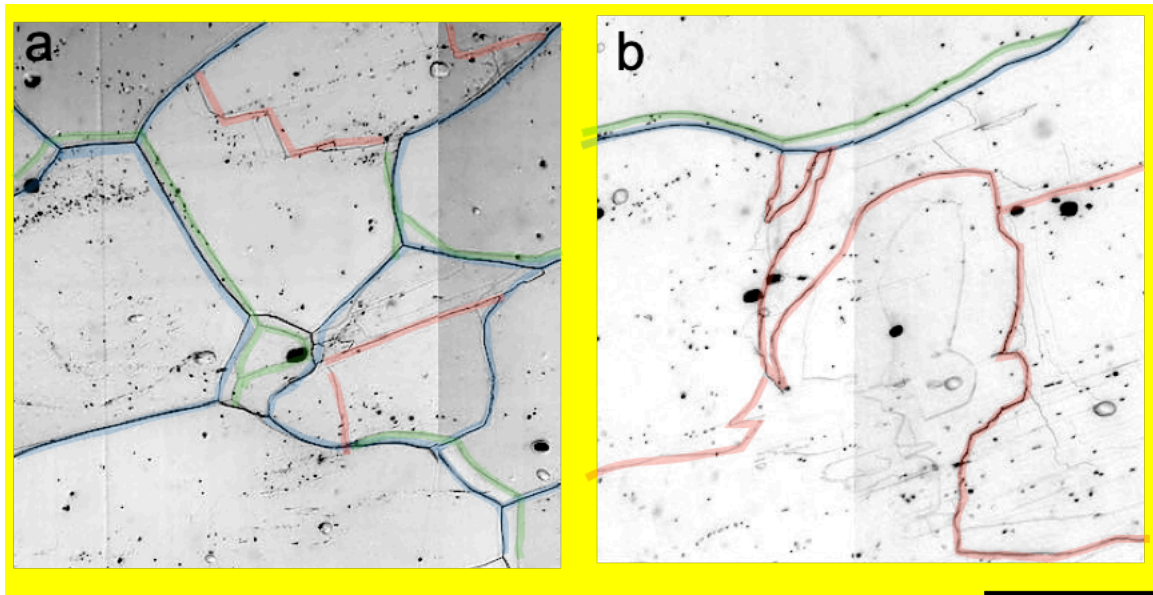
  

2685	2730	<b>2759.5</b>	2807	2847.5	2868	2872	2887	2907.5	2949
~12	~10	<b>~137</b>	~4	~34	~2	~3	~10	~91	~51
55	96	<b>262</b>	44	107 <sup>a)</sup>	41	42 <sup>a)</sup>	45	56	48
1.6	1.6	<b>1.9</b>	1.5	1.5	1.6	1.6	1.5	1.6	1.5
0.5	0.4	<b>0.7</b>	0.5	0.4	0.5	0.5	0.6	0.3	0.3

1278 a) Sum of two thin sections

1279 b) Sum of three thin sections

1280 Figure A3 (a and b) shows closeup images of microstructures. Each panel corresponds to the top-right sections of Figures  
 1281 5a and 5b images. Here, we illustrated grain boundaries, grain boundaries on the reverse side, and subgrain boundaries  
 1282 speculated from geometry by colored shading.



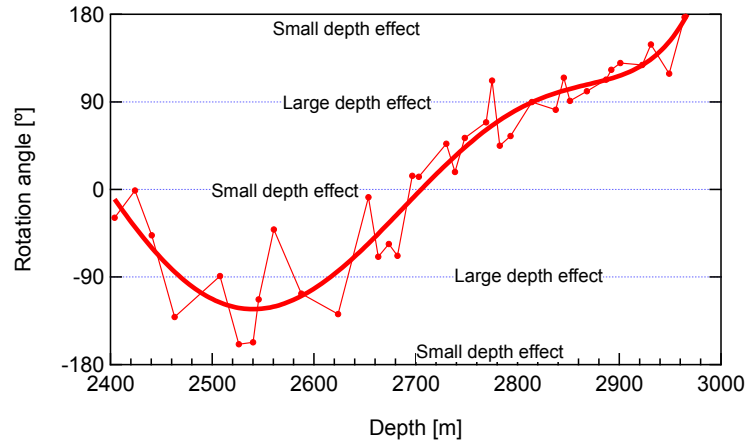
**Figure A3.** Closeup images of microstructures (samples from depths of 2648 and 2685 m). Each corresponds to the top-right of the original images in Figures 5a and 5b. Grain boundaries (blue lines), grain boundaries on the reverse side (green lines) and subgrain boundaries (red lines) speculated from geometry are illustrated. Scale bar: 2mm.

## 1289 Appendix B: Corrections from $\Delta\epsilon'$ to $\Delta\epsilon$

1290 Using data from the Laue X-ray diffraction measurement taken at 43 42 different depths, we initially examined both the  
1291 inclination angle and the horizontal orientation of the  $c$ -axes cluster. We assumed that the inclination angle of the  $c$ -axes  
1292 cluster consistently develops towards the same horizontal orientation within the ice sheet, a plausible assumption given the  
1293 unlikelihood of horizontal rotation in ice flow under deep englacial conditions at the dome summit. In the ice sheet, there is  
1294 a possibility that the inclination angle of the  $c$ -axis cluster may rotate with increasing depths if the dome summit position  
1295 migrates in a complex manner. Another possibility is that when handling many cylindrical ice cores, sometimes the continuity  
1296 of orientation between adjacent cores is lost, especially when irregular ice core breaks occur. When we perform the DTM  
1297 measurements, we do not know the core orientation in advance. We can determine the orientation only from the Laue data  
1298 (or orientation of layer inclination if they were recorded). Only with the assumptions we made were we able to apply  
1299 corrections from  $\Delta\epsilon'$  to  $\Delta\epsilon$ . The inclination angle of the  $c$ -axes cluster is presented in Figure 5f of the main text. We observed  
1300 that the horizontal orientation of the  $c$ -axes cluster gradually rotates with increasing depth (Figure B1). To address the data  
1301 scatter, we proposed a fitting curve as shown in the figure. Notably, some data scatter between approximately 2400 and 2700  
1302 m leads to significant deviations from the fitting curve. We calculated the tensorial components of  $c$ -axes projected onto the  
1303 diagram's periphery and further computed eigenvalue anisotropy (the difference between the maximum and minimum) by  
1304 combining the inclination angle of the  $c$ -axes cluster (Figure 5f) and the horizontal orientation of the  $c$ -axes cluster (Figure  
1305 B1) for orientations where the  $c$ -axes cluster aligns with the periphery of the Schmidt net diagram (as shown in Figure A2b').  
1306 The results are presented in Figure B2. Using these data, we estimated coefficients for correcting  $\Delta\epsilon$  to  $\Delta\epsilon'$ , detailed in Figure  
1307 B3. We found that the necessary corrections are minor (up to several percent) at depths shallower than about 2730 m but  
1308 become more significant at deeper depths (up to about 20 percent). At depths between approximately 2400 and 2730 m,  
1309 where large deviations from the fitting curve were observed (Figure B1), the resulting errors in corrections are likely limited  
1310 due to the inclination angle of the  $c$ -axes cluster remaining small, less than about 20 degrees, in this depth range (Figure 5c).  
1311 Therefore, we estimate the errors in our correction coefficients to be less than 10%.

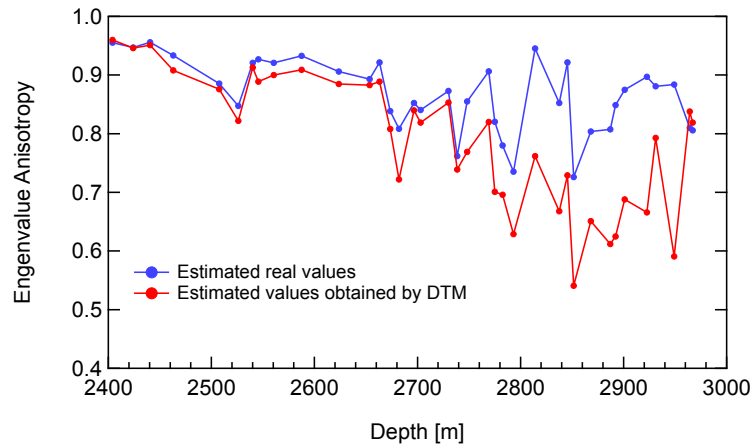
1312 Figure B4 displays the  $\Delta\epsilon'$  and  $\Delta\epsilon$  values, along with eigenvalue anisotropy obtained from the Laue X-ray diffraction  
1313 measurements. At depths exceeding 2900 m, the corrections incorporate errors due to continuity uncertainties between core  
1314 samples, which arise from unpredictable core rotation. Consequently, sudden changes in  $\Delta\epsilon$  values may be erroneous.  
1315 Nevertheless, we observed a good agreement between the  $\Delta\epsilon$  values from the two ice cores (DF and EDC) at ages older than  
1316 approximately 630 kyr BP, corresponding to the ice age at 2900 m.

1317



1318

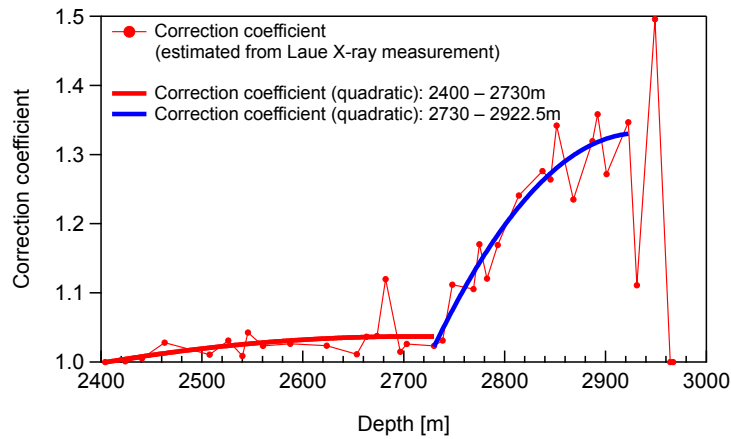
1319 **Figure B1.** Horizontal orientation of the *c*-axes cluster (left axis) was derived from the COF *c*-axis fabric data obtained through the Laue  
 1320 X-ray diffraction measurements. Angles of 0, 180, or -180 degrees indicate that the *c*-axes cluster is perpendicular to the observer's line of  
 1321 sight and parallel to the electric field vector of the electromagnetic waves. Conversely, angles of 90 or -90 degrees indicate that the *c*-axes  
 1322 cluster is parallel to the observer's line of sight and perpendicular to the electric field vector. When the horizontal orientation of the *c*-axes  
 1323 cluster measures 0, 180, or -180 degrees, it aligns with the periphery of the Schmidt equal area projection.



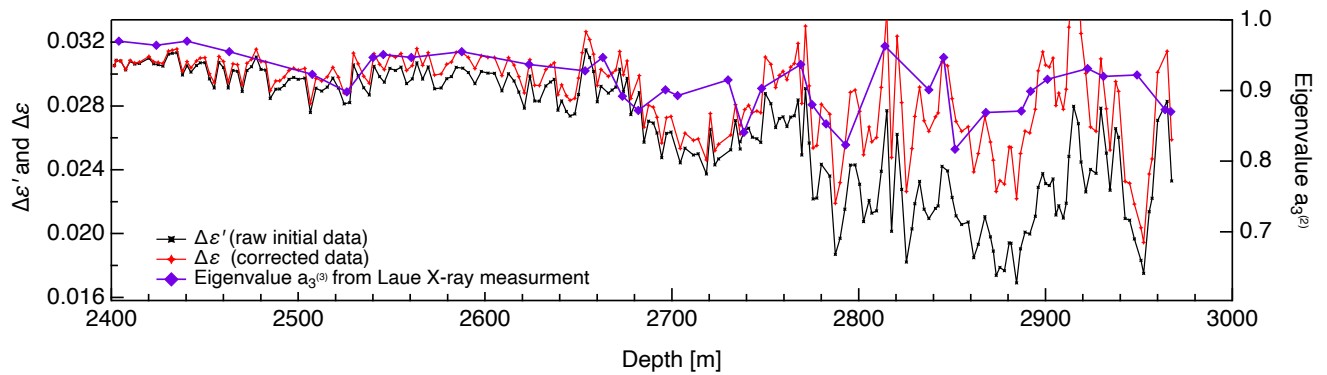
1324

1325 **Figure B2.** Comparison of eigenvalue anisotropy values between measurement frame (indicated in red) and corrected frame (indicated in  
 1326 blue).

1327



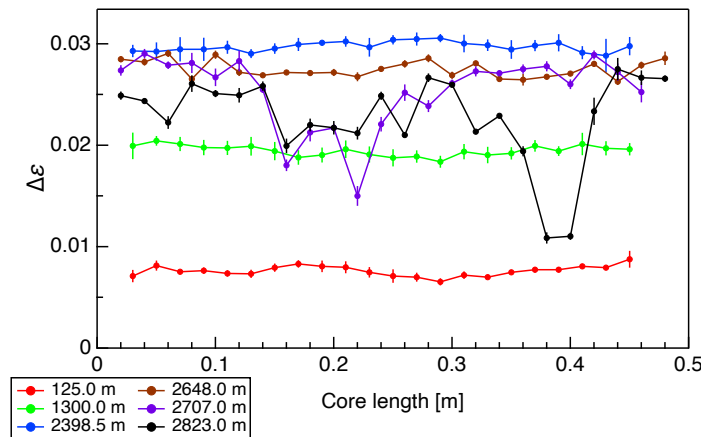
**Figure B3.** Correction coefficients for converting  $\Delta\epsilon'$  to  $\Delta\epsilon$ . This figure presents proposed fitting curves for depths ranging from 2400 to 2730 m and for depths greater than 2730 m.



**Figure B4.** Correction of  $\Delta\epsilon'$  (depicted in black) to  $\Delta\epsilon$  (shown in red) and comparison with eigenvalues  $a_3^{(2)}$  (illustrated in purple) as estimated from the Laue X-ray Diffraction Measurements. It is important to note that the DTM data represent average values for each 0.5 m section using thick-sections, while the Laue X-ray diffraction measurement data are derived from thin sections. The volume of ice represented by a single data point differs by approximately  $10^2$  times. Additionally, the DTM method provides volume-weighted values of COF c-axis fabric, whereas the Laue X-ray diffraction measurements yield an average value across the total number of crystal grains, typically not accounting for the size (volume) of each individual crystal grain.

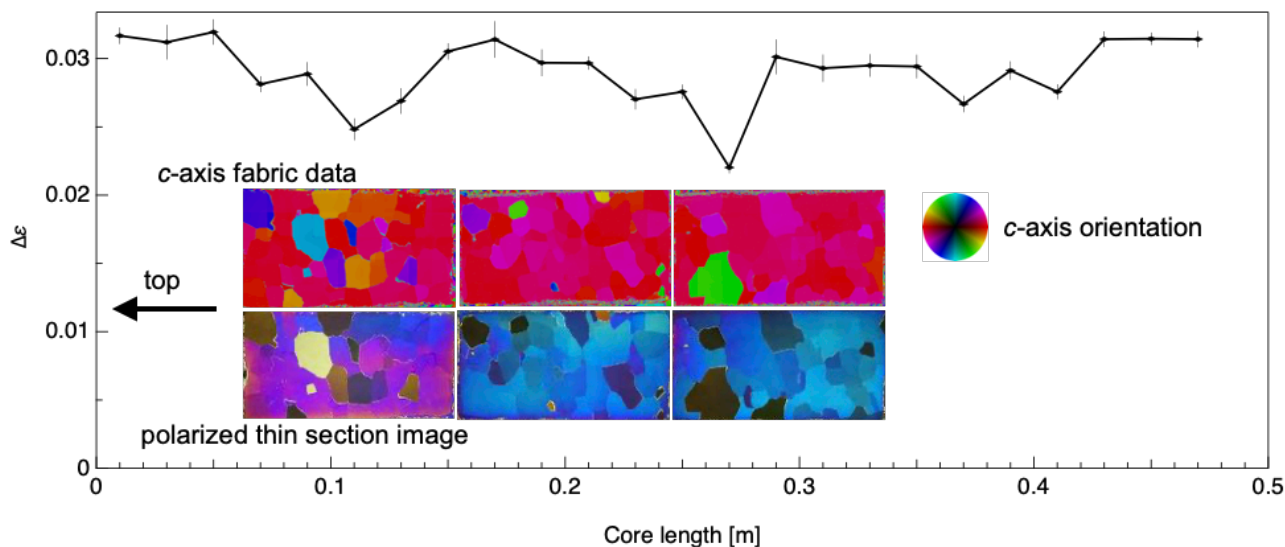
# Appendix C: Continuous Variations in $\Delta\epsilon$ and Comparison with Microstructures

Figure C1 showcases examples of the continuous variation of  $\Delta\epsilon$  across 0.5 m core samples at five depths (125.0–125.5, 1300.0–1300.5, 2648.0–2648.5, 2707.0–2707.5, and 2823.0–2823.5 m). The shallowest 2 depths were obtained from Saruya et al. (2022b). The mean values and standard deviations for each 0.02 m segment were calculated using various TEM  $_{0,0,q}$  resonance modes in the open resonator method. For the data in Figure C1, the mean values (and SD) at these five depths are 0.0076 (0.0005), 0.0194 (0.0006), 0.0285 (0.0008), 0.0263 (0.0036), and 0.0282 (0.0043), respectively. Fluctuations within the 0.5 m ice core samples become more pronounced at greater depths. However, in the core sample with a higher concentration of dust particles (at 2648.0 m, represented by brown plots), the fluctuations are not as marked.



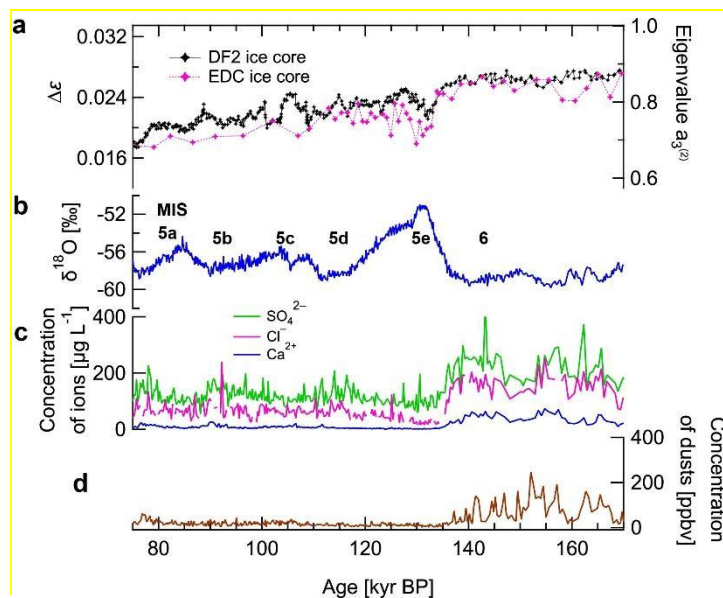
**Figure C1.** Examples of variations in  $\Delta\epsilon$  along 0.5 m sections of ice cores, as determined by continuous measurements. The bars display standard deviations derived from various resonance modes in the open resonator.

Figure C2 presents an example of comparing the  $\Delta\epsilon$  profile with microstructures, specifically for the 2490.0–2490.5 m sample. The upper and lower panels show fabric data and polarized images, respectively. Within the  $\Delta\epsilon$  profile, two locations exhibit lower  $\Delta\epsilon$  values (at 0.11 and 0.27 m). At these depths, grains are observed with  $c$ -axis orientations differing from those of the surrounding grains. These layers contribute to a decrease in the mean  $\Delta\epsilon'$  value and an increase in the SD value for this 0.5 m core section.



**Figure C2.** An example of comparing the  $\Delta\epsilon$  variation along a 0.5 m ice core section with microstructures (COF **c-axis** fabric data and polarized images) obtained from thin-section measurements (2490.0–2490.5 m). The bars in the  $\Delta\epsilon$  variation graph represent standard deviations from different resonance modes of the open resonator. The horizontal scales in both the  $\Delta\epsilon$  variation graph and the microstructural images are aligned for consistency.

#### Appendix D: Modified Figure 10 highlighting the Termination II and MIS 5



1368  
1369  
1370  
1371  
1372  
1373  
  
1374  
1375  
1376

Figure D: Modification of the Figure 10. Crystal orientation fabric data from the DF core and the EDC core are compared using a common age scale of the DF2021 age scale. (a)  $\Delta\epsilon$  presented as mean values for each 0.5-m segment (black markers for DF) or for each thin section (magenta marker for EDC). The right axis provides a scale for normalized eigenvalues. (b) Oxygen isotope ratios ( $\delta_{18}\text{O}$ ) in the DF ice core. (c) Concentrations of  $\text{Cl}^-$ ,  $\text{SO}_4^{2-}$ , and  $\text{Ca}^{2+}$  ions (Goto-Azuma et al., 2019). (d) Concentration of dust particles (DFICPM, 2017). For ice at EDC at MIS5, the normalized eigenvalues are smaller than those at DF.

- 1378 Abbasi, R., Ackermann, M., Adams, J., Aggarwal, N., Aguilar, J., Ahlers, M., et al. (2024). In situ estimation of ice crystal  
1379 properties at the South Pole using LED calibration data from the IceCube Neutrino Observatory. *The Cryosphere*, 18(1),  
1380 75-102. <https://tc.copernicus.org/articles/18/75/2024>, 2024
- 1381 Alley, R.B.: Flow law hypotheses for ice sheet modelling, *J. Glaciol.*, 38(12), 245–256,  
1382 <https://doi.org/10.3189/S0022143000003658>, 1992.
- 1383 Alley, R. B., and Woods, G. A.: Impurity influence on normal grain growth in the GISP2 ice core, Greenland, *J. Glaciol.*,  
1384 42(141), 255–260, <https://doi.org/10.3189/S0022143000004111>, 1996.
- 1385 Azuma, N.: A flow law for anisotropic polycrystalline ice under uniaxial compressive deformation, *Cold Reg. Sci. Tech.*, 23,  
1386 137-147, [https://doi.org/10.1016/0165-232X\(94\)00011-L](https://doi.org/10.1016/0165-232X(94)00011-L), 1995.
- 1387 Azuma, N. and Goto-Azuma, K.: An anisotropic flow law for ice-sheet ice and its implications, *Ann. Glaciol.*, 23, 202-208,  
1388 <https://doi.org/10.3189/S0260305500013458>, 1996.
- 1389 Azuma, N., Wang, Y., Mori, K., Narita, H., Hondoh, T., Shoji, H., and Watanabe O.: Textures and fabrics in the Dome F  
1390 (Antarctica) ice core, *Ann. Glaciol.*, 29, 163–168, <https://doi.org/10.3189/172756499781821148>, 1999.
- 1391 Azuma, N., Wang, Y., Yoshida, Y., Narita, H., Hondoh, T., Shoji, H., and Watanabe, O.: Crystallographic analysis of the  
1392 Dome Fuji ice core, in: *Physics of Ice Core Records*, edited by: Hondoh, T., Hokkaido University Press, Sapporo, 45–61,  
1393 2000.
- 1394 Bamber, J. L., Gomez-Dans, J. L., and Griggs, J. A.: Antarctic 1 km Digital Elevation Model (DEM) from combined ERS-1  
1395 radar and ICESat Laser satellite altimetry, in: *National Snow and Ice Data Center, Digital media*, Boulder, Colorado, USA,  
1396 2009.
- 1397 ~~Barnes, P. R. F., Wolff, E. W., Mader, H. M., Udisti, R., Castellano, E., and Röthlisberger, R.: Evolution of chemical peak~~  
1398 ~~shapes in the Dome C, Antarctica, ice core, *J. Geophys. Res.*, 108, 4126, <https://doi.org/10.1029/2002JD002538>, 2003.~~
- 1399 Bazin, L., Landais, A., Lemieux-Dudon, B., Toyé Mahamadou Kele, H., Veres, D., Parrenin, F., Martinerie, P., Ritz, C.,  
1400 Capron, E., Lipenkov, V., Loutre, M.F., Raynaud, D., Vinther, B., Svensson, A., Rasmussen, S. O., Severi, M., Blunier,  
1401 T., Leuenberger, M., Fischer, H., Masson-Delmotte, V., Chappellaz, J., and Wolff, E.: An optimized multi-proxy, multi-  
1402 site Antarctic ice and gas orbital chronology (AICC2012): 120–800 ka, *Clim. Past*, 9(4), 1715–1731,  
1403 <https://doi.org/10.5194/cp-9-1715-2013>, 2013.
- 1404 Budd, W. F. and Jacka, T. H.: A Review of Ice Rheology for Ice Sheet Modelling, *Cold Reg. Sci. Tech.*, 16, 107-144,  
1405 [https://doi.org/10.1016/0165-232X\(89\)90014-1](https://doi.org/10.1016/0165-232X(89)90014-1), 1989.
- 1406 ~~Bons, P. D., and Jessell, M. W.: Micro shear zones in experimentally deformed octachloropropane, *J. Struct. Geol.*, 21(3),~~  
1407 ~~323–334, [https://doi.org/10.1016/S0191-8141\(98\)90116-X](https://doi.org/10.1016/S0191-8141(98)90116-X), 1999.~~
- 1408 Buizert, C., Fudge, T. J., Roberts, W. H. G., Steig, E. J., Sherriff-Tadano, S., Ritz, C., Lefebvre, E., Edwards, J., Kawamura,  
1409 K., Oyabu, I., Motoyama, H., Kahle, E. C., Jones, T. R., Abe-Ouchi, A., Obase, T., Martin, C., Corr, H., Severinghaus, J.

1410 P., Beaudette, R., Epifanio, J. A., Brook, E. J., Martin, K., Chappellaz, J., Aoki, S., Nakazawa, T., Sowers, T., Alley, R.,  
 1411 Ahn, J., Sigl, M., Severi, M., Dunbar, N. W., Svensson, A., Fegyveresi, J., He, C., Liu, Z., Zhu, J., Otto-Bliesner, B.,  
 1412 Lipenkov, V., Kageyama, M., and Schwander, J.: Antarctic-wide surface temperature and elevation during the Last Glacial  
 1413 Maximum, *Science*, 372, 1097–1101, <https://doi.org/10.1126/science.abd2897>, 2021.

1414 Calonne, N., Montagnat, M., Matzl, M., and Schneebeli M.: The layered evolution of fabric and microstructure of snow at  
 1415 Point Barnola, Central East Antarctica, *Earth Planet. Sci. Lett.*, 460, 293–301, <https://doi.org/10.1016/j.epsl.2016.11.041>,  
 1416 2017

1417 Castelnau, O., Thorsteinsson, T., Kipfstuhl, J., Duval, P., and Canova, G. R.: Modelling fabric development along the GRIP  
 1418 ice core, central Greenland, *Ann. Glaciol.*, 23, 194–201, <https://doi.org/10.3189/S0260305500013446>, 1996.

1419 Castelnau, O., Shoji, H., Mangeney, A., Milsch, H., Duval, P., Miyamoto, A., Kawada, K., and Watanabe, O.: Anisotropic  
 1420 behavior of GRIP ices and flow in Central Greenland, *Earth Planet. Sc. Lett.*, 154, 307–322, [https://doi.org/10.1016/S0012-](https://doi.org/10.1016/S0012-821X(97)00193-3)  
 1421 [821X\(97\)00193-3](https://doi.org/10.1016/S0012-821X(97)00193-3), 1998.

1422 Chauve, T., Montagnat, M., Barou, F., Hidas, K., Tommasi, A., and Mainprice, D.: Investigation of nucleation processes during  
 1423 dynamic recrystallization of ice using cryo-EBSD, *Phil. Trans. R. Soc. A*, 375, 20150345,  
 1424 <http://dx.doi.org/10.1098/rsta.2015.0345>, 2017.

1425 Church, J., Clark, P., Cazenave, A., Gregory, J., Jevrejeva, S., Levermann, A., Merrifield, M., Milne, G., Nerem, R., Nunn, P.,  
 1426 Payne, A., Pfeffer, W., Stammer, D. and Unnikrishnan, A.: Sea Level Change. In: *Climate Change 2013: The Physical*  
 1427 *Science Basis. Contribution of Working Group I to the Fifth Assessment Report of the Intergovernmental Panel on Climate*  
 1428 *Change (IPCC)*, Cambridge University Press, Cambridge, 1137–1216, 2013.

1429 Colbeck, S. C.: ~~Snow crystal growth with varying surface temperatures and radiation penetration, *J. Glaciol.*, 35(119), 23–29,~~  
 1430 ~~<https://doi.org/10.3189/002214389793701536>, 1989.~~

1431 Cuffey, K. M., and Paterson, W. S. B.: *The Physics of Glaciers*, 4th edition, Elsevier, Amsterdam, 2010.

1432 Cullen, A. L.: Infrared and Millimeter Waves, in *Millimeter-Wave Open-Resonator Techniques*, Academic Press, New York,  
 1433 pp. 233–280, 1983.

1434 Dahl-Jensen, D., Johnsen, S. J., Hammer, C. U., Clausen, H. B., and Jouzel, J.: Past Accumulation rates derived from observed  
 1435 annual layers in the GRIP ice core from Summit, Central Greenland, In: Peltier, W.R. (eds) *Ice in the Climate System*.  
 1436 NATO ASI Series, vol 12. Springer, Berlin, Heidelberg. [https://doi.org/10.1007/978-3-642-85016-5\\_29](https://doi.org/10.1007/978-3-642-85016-5_29), 1993.

1437 Dahl-Jensen, D., Mosegaard, K., Gundestrup, N., Clow, G. D., Johnsen, S. J., Hansen, A. W., and Balling, N.: Past  
 1438 Temperatures Directly from the Greenland Ice Sheet, *Science*, 282, 268–271, <https://doi.org/10.1126/science.282.5387.268>,  
 1439 1998.

1440 De La Chapelle, S., Castelnau, O., Lipenkov, V., and Duval, P.: Dynamic recrystallization and texture development ice as  
 1441 revealed by the study of deep ice cores Antarctica and Greenland, *J. Geophys. Res.*, 103, 5091–5105,  
 1442 <https://doi.org/10.1029/97JB02621>, 1998.

1443 Dome Fuji Ice Core Project Members: State dependence of climatic instability over the past 720,000 years from Antarctic ice  
 1444 cores and climate modeling, *Sci. Adv.*, 3(2), e1600446, <https://doi.org/10.1126/sciadv.1600446>, 2017.

1445 Drews, R., Eisen, O., Weikusat, I., Kipfstuhl, S., Lambrecht, A., Steinhage, D., Wilhelms, F., and Miller, H.: Layer  
 1446 disturbances and the radio-echo free zone in ice sheets, *The Cryosphere*, 3, 195–203, <https://doi.org/10.5194/tc-3-195-2009>,  
 1447 2009.

1448 ~~Drury, M., and Humphreys, F.: Microstructural shear criteria associated with grain boundary sliding during ductile~~  
 1449 ~~deformation, *J. Struct. Geol.*, 10(1): 83–89, [https://doi.org/10.1016/0191-8141\(88\)90130-7](https://doi.org/10.1016/0191-8141(88)90130-7), 1988.~~

1450 Durand, G., Weiss, J., Lipenkov, V., Barnola, J., Krinner, G., Parrenin, F., Delmonte, B., Ritz, C., Duval, P., and Röthlisberger,  
 1451 R.: Effect of impurities on grain growth in cold ice sheets, *J. Geophys. Res.*, 111(F1), F01015,  
 1452 <https://doi.org/10.1029/2005JF000320>, 2006.

1453 Durand, Gillet-Chaulet, F., Svensson, A., Gagliardini, O., Kipfstuhl, S., Meyssonier, J., Parrenin, F., Duval, P., and Dahl-  
 1454 Jensen, D.: Change in ice rheology during climate variations - implications for ice flow modelling and dating of the EPICA  
 1455 Dome C core, *Clim. Past*, 3, 155-167, <https://doi.org/10.5194/cp-3-155-2007>, 2007.

1456 Durand, G., Svensson, A., Persson, A., Gagliardini, O., Gillet-Chaulet, F., Sjolte, J., Montagnat M., Dahl-Jensen, D.: Evolution  
 1457 of the texture along the EPICA Dome C ice core, in: *Physics of Ice Core Records II*, edited by: Hondoh, T., Hokkaido  
 1458 University Press, Sapporo, 91–105, 2009.

1459 Duval, P.: Creep and Fabrics of Polycrystalline Ice Under Shear and Compression, *J. Glaciol.*, 27, 129-140,  
 1460 <https://doi.org/10.3189/S002214300001128X>, 1981.

1461 Duval, P. and Le Gac, H.: Mechanical Behaviour of Antarctic Ice, *Ann. Glaciol.*, 3, 92-95,  
 1462 <https://doi.org/10.3189/S0260305500002585>, 1982.

1463 Duval, P., Ashby, M. F., and Anderman, I.: Rate-controlling pro- cesses in the creep of polycrystalline ice, *J. Phys. Chem.*, 87,  
 1464 4066–4074, <https://doi.org/10.1021/j100244a014>, 1983.

1465 Duval, P. and Castelnau, O.: Dynamic recrystallization of ice in polar ice sheets, *J. Phys. III*, 5, 197–205,  
 1466 <https://doi.org/10.1051/jp4:1995317>, 1995.

1467 Eichler, J., Kleitz, I., Bayer-Giraldi, M., Jansen, D., Kipfstuhl, S., Shigeyama, W., Weikusat, C., and Weikusat, I.: Location  
 1468 and distribution of micro-inclusions in the EDML and NEEM ice cores using optical microscopy and in situ Raman  
 1469 spectroscopy, *The Cryosphere*, 11, 1075-1090, <https://doi.org/10.5194/tc-11-1075-2017>, 2017.

1470 Eisen, O., Steinhage, D., Karlsson, N. B., Binder, T., Helm, V.: Ice thickness of Dome Fuji region, Antarctica, recorded with  
 1471 the AWI airborne radar system: line 20172048. PANGAEA, <https://doi.org/10.1594/PANGAEA.920649>, 2020.

1472 EPICA Community Members: Eight glacial cycles from an Antarctic ice core, *Nature*, 429, 623–628,  
 1473 <https://doi.org/10.1038/nature02599>, 2004.

1474 Fan, S., Hager, T. F., Prior, D. J., Cross, A. J., Goldsby, D. L., Qi, C., Negrini, M., and Wheeler, J.: Temperature and strain  
 1475 controls on ice deformation mechanisms: insights from the microstructures of samples deformed to progressively higher  
 1476 strains at –10, –20 and –30 °C, *The Cryosphere*, 14, 3875-3905, <https://doi.org/10.5194/tc-14-3875-2020>, 2020.

1477 Faria, S. H., Kipfstuhl, S., Azuma, N., Freitag, J., Weikusat, I., Murshed, M. M., and Kuhs, W. F.: The Multiscale Structure  
 1478 of Antarctica Part I: Inland Ice, in: Physics of Ice Core Records II, edited by: Hondoh, T., Hokkaido University Press,  
 1479 Sapporo, 39–59, 2009.

1480 Faria, S. H., Weikusat, I., and Azuma, N.: The microstructure of polar ice. Part I: Highlights from ice core research, *J. Struct.*  
 1481 *Geol.*, 61, 2–20, <http://dx.doi.org/10.1016/j.jsg.2013.09.010>, 2014a.

1482 Faria, S. H., Weikusat, I., and Azuma, N.: The microstructure of polar ice. Part II: State of the art, *J. Struct. Geol.*, 61, 21–49,  
 1483 <http://dx.doi.org/10.1016/j.jsg.2013.11.003>, 2014b.

1484 Fitzpatrick, J. J., Voigt, D. E., Fegyveresi, J. M., Stevens, N. T., Spencer, M. K., Cole-Dai, J., Alley, R. B., Jardine, G. E.,  
 1485 Cravens, E. D., Wilen, L. A., Fudge, T. J., and McConnell, J. R.: Physical properties of the WAIS Divide ice core, *J.*  
 1486 *Glaciol.*, 60, 1181–1198, <http://dx.doi.org/10.3189/2014JoG14J100>, 2014.

1487 Freitag, J., Kipfstuhl, S., Laepple, T., and Wilhelms, F.: Impurity controlled densification: a new model for stratified polar  
 1488 firn, *J. Glaciol.*, 59, 1163–1169, <https://doi.org/10.3189/2013JoG13J042>, 2013.

1489 Fletcher, N. H.: The Chemical Physics of Ice, Cambridge University Press, Cambridge,  
 1490 <http://dx.doi.org/10.1017/CBO9780511735639>, 1970.

1491 Fujita, S., Nakawo, M., and Mae, S.: Orientation of the 700m Mizuho core and its strain history., *Proc. NIPR Symp. Polar*  
 1492 *Meteorol. Glaciol.*, 1, 122–131, <https://doi.org/10.15094/00003530>, 1987

1493 Fujita, S., Maeno, H., Uratsuka, S., Furukawa, T., Mae, S., Fujii, Y., and Watanabe, O.: Nature of radio echo layer in the  
 1494 Antarctic ice sheet detected by a two-frequency experiment, *J. Geophys. Res.*, 104(B6), 13013–13024,  
 1495 <https://doi.org/10.1029/1999JB900034>, 1999.

1496 Fujita, S., Matsuoka, T., Ishida, T., Matsuoka, K., and Mae, S.: A summary of the complex dielectric permittivity of ice in the  
 1497 megahertz range and its applications for radar sounding of polar ice sheets, in: Physics of Ice Core Records, edited by:  
 1498 Hondoh, T., Hokkaido University Press, Sapporo, 185–212, <http://hdl.handle.net/2115/32469>, 2000.

1499 Fujita, S., Maeno, H., and Matsuoka, K.: Radio-wave depolarization and scattering within ice sheets: a matrix-based model to  
 1500 link radar and ice-core measurements and its application, *J. Glaciol.*, 52, 407–424,  
 1501 <https://doi.org/10.3189/172756506781828548>, 2006

1502 Fujita, S., Okuyama, J., Hori, A., and Hondoh, T.: Metamorphism of stratified firn at Dome Fuji, Antarctica: A mechanism for  
 1503 local insolation modulation of gas transport conditions during bubble close off, *J. Geophys. Res.*, 114, F03023,  
 1504 <https://doi.org/10.1029/2008JF001143>, 2009.

1505 Fujita, S., Holmlund, P., Matsuoka, K., Enomoto, H., Fukui, K., Nakazawa, F., Sugiyama, S., and Surdyk, S.: Radar diagnosis  
 1506 of the subglacial conditions in Dronning Maud Land, East Antarctica, *The Cryosphere*, 6, 1203–1219,  
 1507 <https://doi.org/10.5194/tc-6-1203-2012>, 2012.

1508 Fujita, S., Hirabayashi, M., Goto-Azuma, K., Dallmayr, R., Satow, K., Zheng, J., and Dahl-Jensen, D.: Densification of layered  
 1509 firn of the ice sheet at NEEM, Greenland, *J. Glaciol.*, 60, 905–921, <https://doi.org/10.3189/2014JoG14J006>, 2014.

1510 Fujita, S., Parrenin, F., Severi, M., Motoyama, H., and Wolff, E. W.: Volcanic synchronization of Dome Fuji and Dome C  
 1511 Antarctic deep ice cores over the past 216 kyr, *Clim. Past*, 11, 1395-1416, <https://doi.org/10.5194/cp-11-1395-2015>, 2015.

1512 Fujita, S., Goto-Azuma, K., Hirabayashi, M., Hori, A., Iizuka, Y., Motizuki, Y., Motoyama H., and Takahashi, K.:  
 1513 Densification of layered firn in the ice sheet at Dome Fuji, Antarctica, *J. Glaciol.*, 62(231), 103–123,  
 1514 <https://doi.org/10.1017/jog.2016.16>, 2016.

1515 Ghan, S., Crawford, J., Langematz, U., Leung, R., Li, Z., Russell, L., Steiner, A., and Zhang, C.: Author contributions can be  
 1516 clarified, *J. Geophys. Res.*, 121, 8155–8155, <https://doi.org/10.1002/2016JD025417>, 2016.

1517 Goodman, D. J., Frost, H. J., and Ashby, M. F.: The plasticity of polycrystalline ice, *Philos. Mag.*, 43(3), 665–695,  
 1518 <https://doi.org/10.1080/01418618108240401>, 1981.

1519 Goto-Azuma, K., Hirabayashi, M., Motoyama, H., Miyake, T., Kuramoto, T., Uemura, R., Igarashi, M., Iizuka, Y., Sakurai,  
 1520 T., and Horikawa, S.: Reduced marine phytoplankton sulphur emissions in the Southern Ocean during the past seven  
 1521 glacials, *Nat. Commun.*, 10(1): 1–7, <https://doi.org/10.1038/s41467-019-11128-6>, 2019.

1522 Gödert, G. and Hutter, K.: Induced anisotropy in large ice shields: theory and its homogenization, *Continuum Mech.*  
 1523 *Thermodyn.*, 10, 293-318, <https://doi.org/10.1007/s001610050095>, 1998.

1524 Goldsby, D. L. and Kohlstedt, D. L.: Superplastic deformation of ice: Experimental observations, *J. Geophys. Res.*, 106,  
 1525 11017-11030, <https://doi.org/10.1029/2000JB900336>, 2001.

1526 Gow, A. J. and Williamson, T.: Rheological implications of the internal structure and crystal fabrics of the West Antarctic ice  
 1527 sheet as revealed by deep core drilling at Byrd Station, *GSA Bulletin*, 87, 1665-1677, [https://doi.org/10.1130/0016-7606\(1976\)87<1665:RIOTIS>2.0.CO;2](https://doi.org/10.1130/0016-7606(1976)87<1665:RIOTIS>2.0.CO;2), 1976.

1528 Hargreaves, N. D.: The radio-frequency birefringence of polar ice, *J. Glaciol*, 21(85), 301–313,  
 1529 <https://doi.org/10.3189/S0022143000033499>, 1978.

1531 Higashi, A., Nakawo, M., Narita, H., Fujii, Y., Nishio, F., and Watanabe, O.: Preliminary Results of Analyses of 700 m Ice  
 1532 Cores Retrieved at Mizuho Station, Antarctica, *Ann. Glaciol.*, 10, 52-56, <https://doi.org/10.3189/S026030550000416X>,  
 1533 1988.

1534 Humphreys, F. and Hatherly, M.: Recrystallization and Related Annealing Phenomena, 2nd edn., Elsevier,  
 1535 <https://doi.org/10.1016/B978-0-08-044164-1.X5000-2>, 2004.

1536 Inoue, R., Fujita, S., Kawamura, K., Oyabu, I., Nakazawa, F., Motoyama, H., and Aoki, T.: Spatial distribution of vertical  
 1537 density and microstructure profiles in near-surface firn around Dome Fuji, Antarctica, *The Cryosphere*, 18, 425–449,  
 1538 <https://doi.org/10.5194/tc-18-425-2024>, 2024.

1539 Jacka, T. and Li, J.: The steady-state crystal size of deforming ice, *Ann. Glaciol.*, 20, 13–18,  
 1540 <https://doi.org/10.3189/1994AoG20-1-13-18>, 1994.

1541 Journaux, B., Chauve, T., Montagnat, M., Tommasi, A., Barou, F., Mainprice, D., and Gest, L.: Recrystallization processes,  
 1542 microstructure and crystallographic preferred orientation evolution in polycrystalline ice during high-temperature simple  
 1543 shear, *The Cryosphere*, 13, 1495–1511, <https://doi.org/10.5194/tc-13-1495-2019>, 2019.

Johnson, A. F.: Creep characterization of transversely-isotropic metallic materials, *J. Mech. Phys. Solids*, 25, 117-126, [https://doi.org/10.1016/0022-5096\(77\)90007-2](https://doi.org/10.1016/0022-5096(77)90007-2), 1977.

~~Jones, S. J.: Softening of ice crystals by dissolved fluoride ions, *Phys. Lett. A*, 25, 366–367, [https://doi.org/10.1016/0375-9601\(67\)90702-5](https://doi.org/10.1016/0375-9601(67)90702-5), 1967.~~

Jones, R. G.: The measurement of dielectric anisotropy using a microwave open resonator, *J. Phys. D: Applied Physics*, 9(5), 819–827, <https://doi.org/10.1088/0022-3727/9/5/015>, 1976a.

Jones, R. G.: Precise dielectric measurements at 35 GHz using an open microwave resonator, *Proc. IEEE*, 123(4), 285–290, <http://doi.org/10.1049/piee.1976.0067>, 1976b.

Jones, S., and Glen, J.: The effect of dissolved impurities on the mechanical properties of ice crystals, *Philos. Mag.*, 19(157), 13–24, <https://doi.org/10.1080/14786436908217758>, 1969.

Kipfstuhl, S., Faria, S. H., Azuma, N., Freitag, J., Hamann, I., Kaufmann, P., Miller, H., Weiler, K., and Wilhelms, F.: Evidence of dynamic recrystallization in polar firn, *J. Geophys. Res.*, 114, B05204, <https://doi.org/10.1029/2008JB005583>, 2009.

Komiyama, B., Kiyokawa, M., and Matsui, T.: Open resonator for precision dielectric measurements in the 100 GHz band. *IEEE Trans. Microw. Theory Tech.*, 30(10), 1792–1796, <https://doi.org/10.1109/22.88556>, 1991.

Kuiper, E.-J. N., Weikusat, I., de Bresser, J. H. P., Jansen, D., Pennock, G. M., and Drury, M. R.: Using a composite flow law to model deformation in the NEEM deep ice core, Greenland – Part 1: The role of grain size and grain size distribution on deformation of the upper 2207 m, *The Cryosphere*, 14, 2429–2448, <https://doi.org/10.5194/tc-14-2429-2020>, 2020.

Langway, C. C.: Ice fabrics and the universal stage, *SIPRE Tech. Rep.*, 62, 1958.

~~Lipenkov, V., Barkov, N., Duval, P., and Pimienta, P.: Crystalline Texture of the 2083 m Ice Core at Vostok Station, Antarctica, *J. Glaciol.*, 35(121), 392–398, <https://doi.org/10.3189/S0022143000009321>, 1989.~~

~~Llorens, M. G., Grier, A., Bons, P. D., Lebensohn, R. A., Evans, L. A., Jansen, D., and Weikusat, I.: Full-field predictions of ice dynamic recrystallisation under simple shear conditions, *Earth Planet. Sci. Lett.*, 450, 233–242, <http://dx.doi.org/10.1016/j.epsl.2016.06.045>, 2016.~~

Mangeney, A., Califano, F., and Hutter, K.: A numerical study of anisotropic, low Reynolds number, free surface flow for ice sheet modeling, *J. Geophys. Res.*, 102(B10), 22749–22764, <https://doi.org/10.1029/97JB01697>, 1997.

Matsuda, M., Wakahama, G., and Budd, W. F.: Twinning of ice from Antarctic ice sheet. Observations of a-axis orientation associated with diamond c-axis orientation fabric, *Low temperature science (Teion kagaku). Series A Physical sciences*, 34, 163–171, 1976.

Matsuda, M., and Wakahama, G.: Crystallographic structure of polycrystalline ice, *J. Glaciol.*, 21, 607–620, <https://doi.org/10.3189/S0022143000033724>, 1978.

Matsuoka, T., Mae, S., Fukazawa, H., Fujita, S., and Watanabe, O.: Microwave dielectric properties of the ice core from Dome Fuji, Antarctica, *Geophys. Res. Lett.*, 25, 1573–1576, <https://doi.org/10.1029/98GL01225>, 1998.

Miyamoto, A., Weikusat, I., and Hondoh, T.: Complete determination of ice crystal orientation using Laue X-ray diffraction method. *J. Glaciol.*, 57(201), 103–110, <https://doi.org/10.3189/002214311795306754>, 2011.

1578 Montagnat, M., Buiron, D., Arnaud, L., Broquet, A., Schlitz, P., Jacob, R., and Kipfstuhl, S.: Measurements and numerical  
1579 simulation of fabric evolution along the Talos Dome ice core, Antarctica, *Earth and Planetary Science Letters*, 357-358,  
1580 168-178, <https://doi.org/10.1016/j.epsl.2012.09.025>, 2012.

1581 Montagnat, M., Azuma, N., Dahl-Jensen, D., Eichler, J., Fujita, S., Gillet-Chaulet, F., Kipfstuhl, S., Samyn, D., Svensson, A.,  
1582 and Weikusat, I.: Fabric along the NEEM ice core, Greenland, and its comparison with GRIP and NGRIP ice cores, *The*  
1583 *Cryosphere*, 8, 1129-1138, <https://doi.org/10.5194/tc-8-1129-2014>, 2014.

1584 Montagnat, M., Chauve, T., Barou, F., Tommasi, A., Beausir, B., and Fressengeas, C.: Analysis of Dynamic Recrystallization  
1585 of Ice from EBSD Orientation Mapping, *Front. Earth Sci.*, 3, 81, <https://doi.org/10.3389/feart.2015.00081>, 2015.

1586 Montagnat, M., Löwe, H., Calonne, N., Schneebeil, M., Matzl, M., and Jaggi, M.: On the Birth of Structural and  
1587 Crystallographic Fabric Signals in Polar Snow: A case study from the EastGRIP snowpack, *Frontiers in Earth Science*, 8,  
1588 <https://doi.org/10.3389/feart.2020.00365>, 2020.

1589 Monz, M. E., Hudleston, P. J., Prior, D. J., Michels, Z., Fan, S., Negrini, M., Langhorne, P. J., and Qi, C.: Full crystallographic  
1590 orientation (c and a axes) of warm, coarse-grained ice in a shear-dominated setting: a case study, Storglaciären, Sweden,  
1591 *The Cryosphere*, 15, 303–324, <https://doi.org/10.5194/tc-15-303-2021>, 2021.

1592 Motoyama, H., Takahashi, A., Tanaka, Y., Shinbori, K., Miyahara, M., Yoshimoto, T., Fujii, Y., Furusaki, A., Azuma, N., and  
1593 Ozawa, Y.: Deep ice core drilling to a depth of 3035.22 m at Dome Fuji, Antarctica in 2001–07, *Ann. Glaciol.*, 62(85-86),  
1594 212–222, <https://doi.org/10.1017/aog.2020.84>, 2020.

1595 Nakamura, T., and Jones, S.: Softening effect of dissolved hydrogen chloride in ice crystals, *Scripta Metallurgica*, 4(2), 123–  
1596 126, [https://doi.org/10.1016/0036-9748\(70\)90176-6](https://doi.org/10.1016/0036-9748(70)90176-6), 1970.

1597 Ohno, H., Igarashi, M., and Hondoh, T.: Salt inclusions in polar ice core: Location and chemical form of water-soluble  
1598 impurities, *Earth Planet. Sc. Lett.*, 232, 171–178, <https://doi.org/10.1016/j.epsl.2005.01.001>, 2005.

1599 Ohno, H., Iizuka, Y., Hori, A., Miyamoto, A., Hirabayashi, M., Miyake, T., Kuramoto, T., Fujita, S., Segawa, T., Uemura, R.,  
1600 Sakurai, T., Suzuki, T., and Motoyama, H.: Physicochemical properties of bottom ice from Dome Fuji, inland East  
1601 Antarctica, *J. Geophys. Res.*, 121(7), 1230–1250, <https://doi.org/10.1002/2015JF003777>, 2016.

1602 Oyabu, I., Iizuka, Y., Kawamura, K., Wolff, E., Severi, M., Ohgaito, R., et al., Compositions of dust and sea salts in the Dome  
1603 C and Dome Fuji ice cores from Last Glacial Maximum to early Holocene based on ice-sublimation and single-particle  
1604 measurements. *J. Geophys. Res.*, 125, e2019JD032208. <https://doi.org/10.1029/2019JD032208>, 2020.

1605 Oyabu, I., Kawamura, K., Buizert, C., Parrenin, F., Orsi, A., Kitamura, K., Aoki, S., and Nakazawa, T.: The Dome Fuji ice  
1606 core DF2021 chronology (0–207 kyr BP), *Quaternary Sci. Rev.*, 294, 107754,  
1607 <https://doi.org/10.1016/j.quascirev.2022.107754>, 2022.

1608 Oyabu, I., Kawamura, K., Fujita, S., Inoue, R., Motoyama, H., Fukui, K., Hirabayashi, M., Hoshina, Y., Kurita, N., Nakazawa,  
1609 F., Ohno, H., Sugiura, K., Suzuki, T., Tsutaki, S., Abe-Ouchi, A., Niwano, M., Parrenin, F., Saito, F., and Yoshimori, M.:  
1610 Temporal variations of surface mass balance over the last 5000 years around Dome Fuji, Dronning Maud Land, East  
1611 Antarctica, *Clim. Past*, 19, 293–321, <https://doi.org/10.5194/cp-19-293-2023>, 2023.

1612 Parrenin, F., Fujita, S., Abe-Ouchi, A., Kawamura, K., Masson-Delmotte, V., Motoyama, H., Saito, F., Severi, M., Stenni, B.,  
1613 Uemura, R., and Wolff, E. W.: Climate dependent contrast in surface mass balance in East Antarctica over the past 216 ka,  
1614 *Journal of Glaciology*, 1-12, <https://doi.org/10.1017/jog.2016.85>, 2016, 2016.

1615 Paterson, W. S. B.: Why ice-age ice is sometimes "soft", *Cold Reg. Sc. Tech.*, 20, 75-98, <https://doi.org/10.1016/0165->  
1616 232X(91)90058-O, 1991.

1617 Pattyn, F., Perichon, L., Aschwanden, A., Breuer, B., de Smedt, B., Gagliardini, O., Gudmundsson, G. H., Hindmarsh, R. C.  
1618 A., Hubbard, A., Johnson, J. V., Kleiner, T., Kononov, Y., Martin, C., Payne, A. J., Pollard, D., Price, S., Rückamp, M.,  
1619 Saito, F., Souček, O., Sugiyama, S., and Zwinger, T.: Benchmark experiments for higher-order and full-Stokes ice sheet  
1620 models (ISMIP–HOM), *The Cryosphere*, 2, 95–108, <https://doi.org/10.5194/tc-2-95-2008>, 2008.

1621 Pattyn, F.: Antarctic subglacial conditions inferred from a hybrid ice sheet/ice stream model, *Earth Planet. Sc. Lett.*, 295(3–4),  
1622 451–461, <https://doi.org/10.1016/j.epsl.2010.04.025>, 2010.

1623 Petrenko, V. F., and Whitworth, R. W.: *Physics of Ice*, Oxford University Press, Oxford, 1999.

1624 Pimienta, P., Duval, P., and Lipenkov, V. Y.: Mechanical Behavior of Ice Along the 2040 m Vostok Core, Antarctica, *Ann.*  
1625 *Glaciol.*, 10, 137-140, <https://doi.org/10.3189/S0260305500004316>, 1988.

1626 Poirier J.-P. 1985. *Creep of Crystals*. Cambridge Earth Science Series. Xiv, Cambridge University Press. ISBN 0 521 26177,  
1627 *Geological Magazine*, 122, 579-580, <https://doi.org/10.1017/S0016756800035664>, 1985.

1628 Qi, C., Prior, D. J., Craw, L., Fan, S., Llorens, M. G., Griera, A., Negrini, M., Bons, P. D., and Goldsby, D. L.: Crystallographic  
1629 preferred orientations of ice deformed in direct-shear experiments at low temperatures, *The Cryosphere*, 13, 351-371,  
1630 <https://doi.org/10.5194/tc-13-351-2019>, 2019.

1631 Richards, D. H., Pegler, S. S., Piazzolo, S., Stoll, N., & Weikusat, I.: Bridging the gap between experimental and natural fabrics:  
1632 Modeling ice stream fabric evolution and its comparison with ice-core data, *J. Geophys. Res.*, 128, e2023JB027245,  
1633 <https://doi.org/10.1029/2023JB027245>, 2023.

1634 Russell-Head, D. S. and Budd, W. F.: Ice-sheet flow properties derived from bore-hole shear measurements combined with  
1635 ice-core studies, *J. Glaciol.*, 24, 117-130, <https://doi.org/10.3189/S0022143000014684>, 1979.

1636 Saruya, T., Fujita, S., and Inoue, R.: Dielectric anisotropy as indicator of crystal orientation fabric in Dome Fuji ice core:  
1637 method and initial results, *J. Glaciol.*, 68(267), 65–76, <https://doi.org/10.1017/jog.2021.73>, 2022a.

1638 Saruya, T., Fujita, S., Iizuka, Y., Miyamoto, A., Ohno, H., Hori, A., Shigeyama, W., Hirabayashi, M., and Goto-Azuma, K.:  
1639 Development of crystal orientation fabric in the Dome Fuji ice core in East Antarctica: implications for the deformation  
1640 regime in ice sheets, *The Cryosphere* 16(7), 2985–3003, <https://doi.org/10.5194/tc-16-2985-2022>, 2022b.

1641 Shoji, H., and Higashi, A.: A deformation mechanism map of ice, *J. Glaciol.*, 85(21), 419–427,  
1642 <https://doi.org/10.3189/S002214300003358X>, 1978.

1643 Shoji, H. and Langway Jr., C. C.: Mechanical Properties of Fresh Ice Core from Dye 3, Greenland. In: *Greenland Ice Core:*  
1644 *Geophysics, Geochemistry, and the Environment*, <https://doi.org/10.1029/GM033p0039>, 1985.

Steinbach, F., Kuiper, E.-J. N., Eichler, J., Bons, P. D., Drury, M. R., Grier, A., Pennock, G. M., and Weikusat, I.: The Relevance of Grain Dissection for Grain Size Reduction in Polar Ice: Insights from Numerical Models and Ice Core Microstructure Analysis, *Front. Earth Sci.*, 5, <https://doi.org/10.3389/feart.2017.00066>, 2017.

Stoll, N., Eichler, J., Hörhold, M., Erhardt, T., Jensen, C., and Weikusat, I.: Microstructure, micro-inclusions, and mineralogy along the EGRIP ice core – Part 1: Localisation of inclusions and deformation patterns, *The Cryosphere*, 15, 5717–5737, <https://doi.org/10.5194/tc-15-5717-2021>, 2021a.

Stoll, N., Eichler, J., Hörhold, M., Shigeyama, W., and Weikusat, I.: A Review of the Microstructural Location of Impurities in Polar Ice and Their Impacts on Deformation, *Front. Earth Sci.*, 8, 615613, <https://doi.org/10.3389/feart.2020.615613>, 2021b.

Stoll, N., Hörhold, M., Erhardt, T., Eichler, J., Jensen, C., and Weikusat, I.: Microstructure, micro-inclusions, and mineralogy along the EGRIP (East Greenland Ice Core Project) ice core – Part 2: Implications for palaeo-mineralogy, *The Cryosphere*, 16, 667–688, <https://doi.org/10.5194/tc-16-667-2022>, 2022.

Thibert, E., and Domine F.: Thermodynamics and kinetics of the solid solution of HCl in ice, *J. Phys. Chem. B*, 101(18), 3554–3565, <https://doi.org/10.1021/jp962115o>, 1997.

Thomas, R. E., Negrini, M., Prior, D. J., Mulvaney, R., Still, H., Bowman, M. H., Craw, L., Fan, S., Hubbard, B., Hulbe, C., Kim, D., and Lutz, F.: Microstructure and Crystallographic Preferred Orientations of an Azimuthally Oriented Ice Core from a Lateral Shear Margin: Priestley Glacier, Antarctica, 9, <https://doi.org/10.3389/feart.2021.702213>, 2021.

Thorsteinsson, T., Kipfstuhl, J. and Miller, H.: Textures and fabrics in the GRIP ice core, *J. Geophys. Res.*, 102(C12), 26583–26599, <https://doi.org/10.1029/97JC00161>, 1997.

Thorsteinsson, T., Waddington, E. D., Taylor, K. C., Alley, R. B., and Blankenship, D. D.: Strain -rate enhancement at Dye 3, Greenland, *J. Glaciol.*, 45, 338–345, <https://doi.org/10.3189/002214399793377185>, 1999.

Tsutaki, S., Fujita, S., Kawamura, K., Abe-Ouchi, A., Fukui, K., Motoyama, H., Hoshina, Y., Nakazawa, F., Obase, T., Ohno, H., Oyabu, I., Saito, F., Sugiura, K., and Suzuki, T.: High-resolution subglacial topography around Dome Fuji, Antarctica, based on ground-based radar surveys conducted over 30 years, *The Cryosphere*, 16, 2967–2983, <https://doi.org/10.5194/tc-16-2967-2022>, 2022.

Urbini, S., Frezzotti, M., Gandolfi, S., Vincent, C., Scarchilli, C., Vittuari, V., and Fily, M.: Historical behaviour of Dome C and Talos Dome (East Antarctica) as investigated by snow accumulation and ice velocity measurements, *Glob. Planet. Change*, 60, <https://doi.org/10.1016/j.gloplacha.2007.08.002>, 2008.

Wang, Q., Fan, S., Richards, D. H., Worthington, R., Prior, D. J., and Qi, C.: Evolution of crystallographic preferred orientations of ice sheared to high strains by equal-channel angular pressing, *EGUsphere* [preprint], <https://doi.org/10.5194/egusphere-2024-331>, 2024.

Wang, Y., Kipfstuhl, S., Azuma, N., Thorsteinsson, T., and Miller, H.: Ice-fabrics study in the upper 1500 m of the Dome C (East Antarctica) deep ice core, *Ann. Glaciol.*, 37, 97–104, <https://doi.org/10.3189/172756403781816031>, 2003.

1678 Weikusat, I., Kipfstuhl, S., Faria, S. H., Azuma, N., and Miyamoto, A.: Subgrain boundaries and related microstructural  
 1679 features in EDML (Antarctica) deep ice core, *J. Glaciol.*, 55, 461-472, <https://doi.org/10.3189/002214309788816614>, 2009.

1680 Weikusat, I., Jansen, D., Binder, T., Eichler, J., Faria, S. H., Wilhelms, F., Kipfstuhl, S., Sheldon, S., Miller, H., Dahl-Jensen,  
 1681 D., and Kleiner, T.: Physical analysis of an Antarctic ice core – towards an integration of micro- and macrodynamics of  
 1682 polar ice, *Phil. Trans. R. Soc. A*, 375, 20150347, <http://dx.doi.org/10.1098/rsta.2015.0347>, 2017.

1683 Wolff, E. W., Fischer, H., van Ommen, T., and Hodell, D. A.: Stratigraphic templates for ice core records of the past 1.5 Myr,  
 1684 *Clim. Past*, 18, 1563–1577, <https://doi.org/10.5194/cp-18-1563-2022>, 2022.

1685 Yamanouchi, T., Hirasawa, N., Hayashi, M., Takahashi, S., and Kaneto, S.: Meteorological characteristics of Antarctic inland  
 1686 station, Dome Fuji. *Mem. Natl Inst. Polar Res., Spec. Issue*, 57, 94–104, 2003.

1687 Young, D. A., Roberts, J. L., Ritz, C., Frezzotti, M., Quartini, E., Cavitte, M. G. P., Tozer, C. R., Steinhage, D., Urbini, S.,  
 1688 Corr, H. F. J., van Ommen, T., and Blankenship, D. D.: High-resolution boundary conditions of an old ice target near Dome  
 1689 C, Antarctica, *The Cryosphere*, 11, 1897–1911, <https://doi.org/10.5194/tc-11-1897-2017>, 2017.

1690